Parabolized Eddy Viscosity Models for Wind Turbine Wake Modelling

Arthur van Dijk

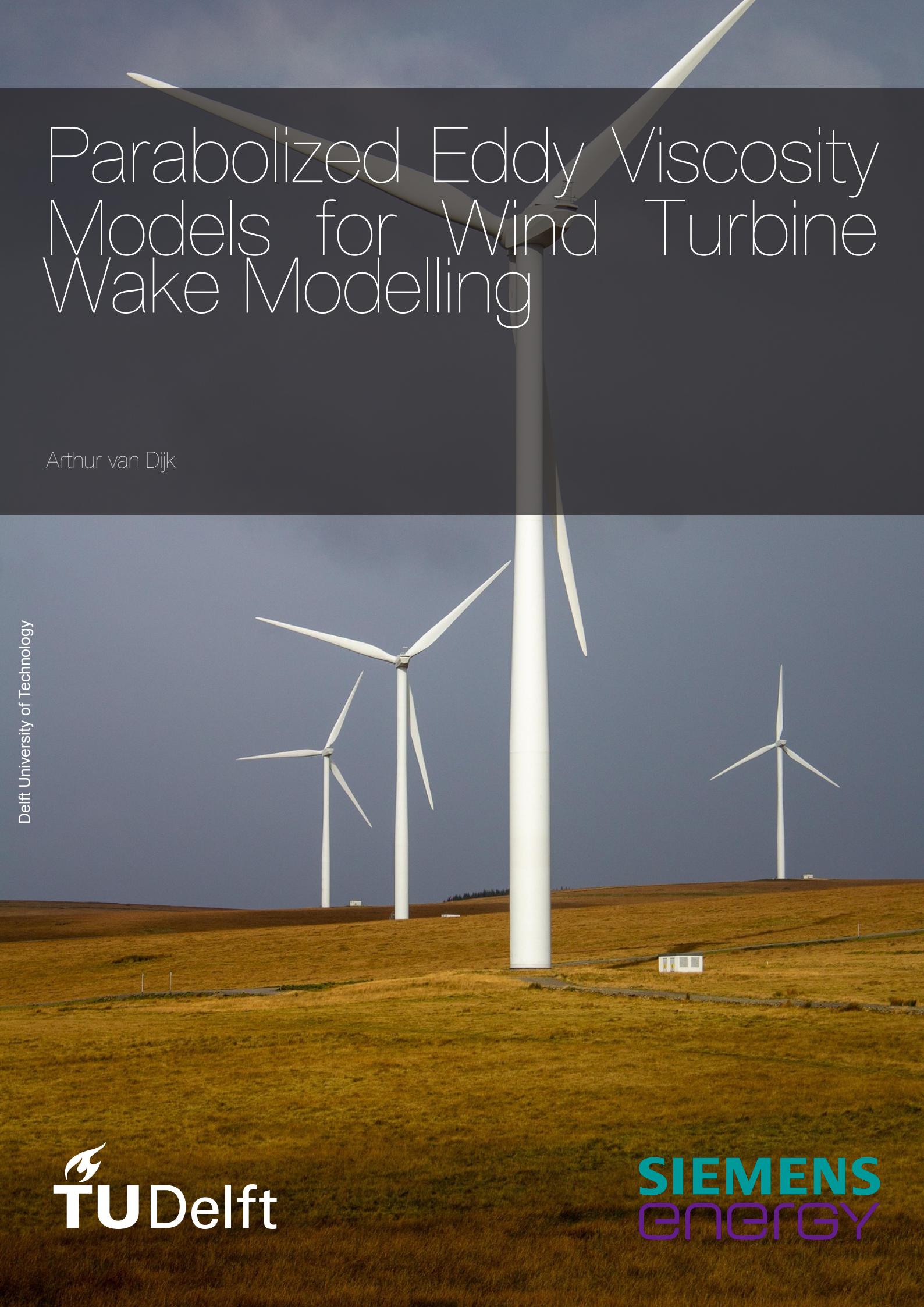

Delft University of Technology

TU Delft

SIEMENS energy

Parabolized Eddy Viscosity Models for Wind Turbine Wake Modelling

by

Arthur van Dijk

to obtain the degree of Master of Science in Aerospace Engineering

at the Delft University of Technology,

to be defended publicly on Thursday April 17, 2026 at 10:00 AM.

Student number:	4888022	
Project duration:	September 22, 2025 – April 17, 2026	
Thesis committee:	Dr. R.P. Dwight,	TU Delft, supervisor
	Dr. M.I. Gerritsma,	TU Delft, chair
	Dr. N.G.W. Warncke,	Siemens Energy, supervisor
	Dr. W. Yu,	TU Delft, committee member

Institution: Delft University of Technology
Place: Faculty of Aerospace Engineering, Delft

An electronic version of this thesis is available at http://repository.tudelft.nl/.

TU Delft

Preface

This thesis marks the end of my studies in Aerospace Engineering at the TU Delft and shows the work I carried out during my graduation internship at Siemens Energy. There, the wind turbine loads team is actively developing a more physically consistent alternative to the wake models currently used in loads computations. The present work contributes to that effort by investigating parabolised k–ε turbulence closures for this model.

I would like to thank my supervisors, Richard Dwight and Norbert Warncke, for their guidance throughout this project. I am especially grateful to Norbert for the amount of time and effort he has invested in supervising me. His willingness to sit down and patiently work through difficult topics has helped me to make this thesis in many ways. The discussions we have had about the intricacies of the parabolised Navier–Stokes equations and subtleties of finite volume discretisations and turbulence modelling, have taught me more than I could have hoped for at the start of this project. These discussions often lasted longer than what could be expected of a supervisor.

I would like to thank my girlfriend for her patience, support and encouragement throughout this long process. Thank you for putting up with the many evenings and weekends that disappeared into the thesis. I am grateful to my parents and my sisters and brother-in-law, whose support over the past years during my studies made it possible for me to come this far.

Finally, I would like to thank my friends from Zebra and my housemates for keeping life outside of the thesis enjoyable. The shared coffee breaks, music and games were welcome distractions to me during these final months.

Arthur van Dijk
Delft, April 2026

Summary

As the share of wind energy in the global electricity mix increases, it becomes more important to accurately predict wind turbine wakes, in order to optimise wind farm layouts and to reduce fatigue loads on downstream turbines. Wake models based on the Reynolds Averaged Navier–Stokes equations offer a good balance between accuracy and computational cost. But their performance depends strongly on the turbulence closure used. The standard k–ε model is widely used in wind energy, but it is known to overpredict the eddy viscosity in the near wake. This leads to an overestimation of turbulent mixing and wake recovery. To address this, researchers have proposed extended closures, which have only been validated in fully elliptic three-dimensional RANS solvers. The Forced Ainslie Wake Model has improved the physical consistency of parabolic wake modelling by reintroducing part of the actuator disk force. Its turbulence closure is currently limited to a constant eddy viscosity. A transport-based turbulence model that is compatible with the parabolic marching scheme of the FAWM is therefore needed.

This thesis develops and validates a parabolized, axisymmetric k–ε turbulence model that can be coupled to the Forced Ainslie Wake Model. Three turbulence closures are implemented. The standard k–ε model and two of its extensions. The k–ε–f_P model limits the eddy viscosity in regions of high shear through a variable C_μ^* derived from the nonlinear eddy viscosity model framework. And the extended k–ε model with a sink term S_k accounts for the extraction of turbulent kinetic energy by the actuator disk. The transport equations for k and ε are discretised on a staggered finite volume grid using a second-order upwind scheme for the convective terms and central differencing for the diffusive term. The turbulence model is coupled with the FAWM through a Picard iteration scheme that exchanges velocity and eddy viscosity at each axial station until convergence. The implementation is verified through the decay of isotropic turbulence, the Method of Manufactured Solutions, and a self-similar coflowing jet simulation. In all three tests, the solver achieves the formal order of convergence. This confirms the correct implementation of the discretisation and the coupling between the transport equations.

During the validation against LES data for a DTU 10MW reference wind turbine across four operating conditions, numerical stability problems were encountered. In the original model formulation, only 5 out of 12 simulations converged. Some of the converged cases produced nonphysical values of the turbulent kinetic energy. The source of the instabilities was traced to the axial gradient of the radial velocity, $\partial V/\partial x$, which contributes to the strain-rate invariant and therefore the production term. Because the radial velocity is derived from the axial velocity through the continuity equation, $\partial V/\partial x$ depends on the second axial derivative of U. Any irregularity in the actuator disk forcing is transferred to the axial velocity through the momentum equation. In a parabolic solver the axial diffusion and pressure terms that would normally dampen these gradients are absent, leading to an overestimation of $\partial V/\partial x$. Neglecting $\partial V/\partial x$ in the computation of the production term restored convergence in 11 out of 12 cases. This also keeps all the predicted values within physical bounds.

With the modified formulation, the three turbulence closures were compared against the LES reference data. For the axial velocity, the k–ε–f_P model performs best in the near wake, with MAPE values between 1 and 4%, while the k–ε–S_k model produces the lowest errors in the far wake. The standard k–ε model has the largest velocity errors across all configurations. The velocity errors increase with increasing thrust coefficient and decreasing wind speed. For the turbulent kinetic energy, all three models overpredict the LES values by a large margin, with full-wake MAPE values ranging from 50 to 126%. The k–ε–S_k model produces the lowest TKE errors in every configuration, while the standard model and k–ε–f_P model have comparable errors.

In summary, this thesis demonstrates that parabolised turbulence models can be coupled with the parabolic FAWM solver. Next to this it shows that the extended closures improve predictions compared to the standard k–ε model. However, the original model formulation with $\partial V/\partial x$ included in the production term is not reliably stable, and the presented results were obtained with a modified formulation. No single closure is best for all flow variables simultaneously. Further work is needed to resolve the stability issue of the original formulation.

Nomenclature

Abbreviations

Abbreviation	Definition
ABL	Atmospheric Boundary Layer
AD	Actuator Disk
ALM	Actuator Line Method
ASM	Algebraic Stress Model
AWM	Ainslie Wake Model
DNS	Direct Numerical Simulation
DTU	Danmarks Tekniske Universitet
FAWM	Forced Ainslie Wake Model
FEM	Finite Element Method
FVM	Finite Volume Method
IEC	International Electrotechnical Commission
LES	Large Eddy Simulation
LRR-IP	Launder–Reece–Rodi Isotropisation of Production
MAPE	Mean Absolute Percentage Error
MMS	Method of Manufactured Solutions
NLEVM	Nonlinear Eddy Viscosity Model
PNS	Parabolized Navier–Stokes
RANS	Reynolds Averaged Navier–Stokes
RRMSE	Relative Root Mean Square Error
RSM	Reynolds Stress Model
SGS	Subgrid-Scale
TKE	Turbulent Kinetic Energy

Symbols

Symbol	Definition	Unit
a	Induction factor	[–]
$\mathbf{a}$	Reynolds stress anisotropy tensor	[–]
A_{cell}	Frontal area of computational cell	[m^2]
b	Initial wake width	[m]
C_μ	Eddy viscosity model constant	[–]
C_μ^*	Variable eddy viscosity coefficient	[–]
C_R	Rotta constant	[–]
C_2	Isotropisation-of-production constant	[–]
C_T	Thrust coefficient	[–]
C_T'	Disk-based thrust coefficient	[–]
$C_{\varepsilon 1}$	ε-equation production constant	[–]
$C_{\varepsilon 2}$	ε-equation destruction constant	[–]
$C_{\varepsilon 4}$	El Kasmi–Masson model constant	[–]
D	Rotor diameter	[m]
D_M	Initial centreline velocity deficit	[–]
$f_{AD,x}$	Axial actuator disk forcing	[N/m^3]
f_i	Body force per unit volume	[N/m^3]
f_P	van der Laan's correction term	[–]
f_0	f_P scaling constant	[–]
F_1, F_2	Filter functions in AWM eddy viscosity	[–]
$G^{(\lambda)}$	NLEVM scalar coefficient	[–]
h	Grid spacing	[m]
I	Ambient turbulence intensity	[–]
I_{REF}	IEC reference turbulence intensity	[–]
k	Turbulent kinetic energy	[m^2/s^2]
k_d	Disk-averaged turbulent kinetic energy	[m^2/s^2]

Symbol	Definition	Unit
l	Length scale	[m]
l_w	Wake length scale	[m]
L	Domain length	[m]
M	Number of radial cells	[–]
n	Decay exponent or number of data points	[–]
n_i	Unit normal vector	[–]
N	Number of axial cells	[–]
N_L	Number of grid points per direction (DNS)	[–]
p	Order of accuracy	[–]
p_f	Force-induced pressure	[Pa]
p_u	Velocity-induced pressure	[Pa]
P	Mean pressure	[Pa]
$\mathcal{P}$	Production of turbulent kinetic energy	[m^2/s^3]
$\mathcal{P}_{ij}$	Reynolds stress production tensor	[m^2/s^3]
P_k	Production of k	[m^2/s^3]
r	Radial coordinate	[m]
R	Rotor radius	[m]
R_W	Wake radius	[m]
$\mathcal{R}_{ij}$	Pressure-rate-of-strain tensor	[m^2/s^3]
Re	Reynolds number	[–]
S	Strain-rate magnitude	[1/s]
S_{ij}	Mean rate of strain tensor	[1/s]
S_k	Sink term in the k-equation	[m^2/s^3]
S_ε	Source term in the ε-equation	[m^2/s^4]
$\mathbf{s}$	Normalised strain-rate tensor	[–]
t	Time	[s]
T_{kij}	Reynolds stress transport tensor	[m^2/s^3]
$\boldsymbol{T}_{ij}^{(\lambda)}$	NLEVM tensor group	[–]
U	Mean axial velocity	[m/s]
U_i	Mean velocity component	[m/s]
U_∞	Freestream velocity	[m/s]
u_i'	Fluctuating velocity component	[m/s]
u_η	Kolmogorov velocity scale	[m/s]
V	Mean radial velocity	[m/s]
V_{cell}	Cell volume	[m^3]
v_w	Wake velocity scale	[m/s]
w_i^x	Axial Gaussian regularisation weight	[–]
x	Axial coordinate	[m]
$\tilde{x}$	Non-dimensional downstream coordinate	[–]
α	NLEVM calibration constant or upwind selector	[–]
β	Inward-flow selector function	[–]
$\gamma_{j,l}$	Area overlap fraction	[–]
$\hat{\gamma}$	Regularised overlap fraction	[–]
δ_{ij}	Kronecker delta	[–]
Δ	Jet half-width	[m]
Δr	Radial cell size	[m]
Δx	Axial cell size	[m]
ε	Dissipation rate of TKE	[m^2/s^3]
ε_α	Ambient eddy viscosity	[m^2/s]
ε_{ij}	Dissipation tensor	[m^2/s^3]
η	Kolmogorov length scale	[m]
θ	Momentum radius	[m]
λ	Velocity excess ratio	[–]
λ_J	Jet velocity ratio	[–]
μ	Dynamic viscosity	[Pa s]
ν	Kinematic viscosity	[m^2/s]
ν_T	Kinematic eddy viscosity	[m^2/s]

Symbol	Definition	Unit
$\boldsymbol{\omega}$	Normalised vorticity tensor	[–]
ω	Under-relaxation factor	[–]
Ω	Control volume	[m^3]
Φ	Contracted strain-rate scalar ($2S_{ij}S_{ij}$)	[1/s^2]
ρ	Fluid density	[kg/m^3]
σ	Local normalised shear parameter	[–]
$\tilde{\sigma}$	Equilibrium shear parameter	[–]
σ_1	Standard deviation of velocity fluctuations	[m/s]
σ_k	Turbulent Prandtl number for k	[–]
σ_ε	Turbulent Prandtl number for ε	[–]
σ_r	Radial regularisation width	[m]
σ_x	Axial regularisation width	[m]
τ	Convergence tolerance	[–]
τ_η	Kolmogorov time scale	[s]
τ_{ij}^{SGS}	Subgrid-scale stress tensor	[m^2/s^2]

Contents

List of Figures

List of Tables

1 Introduction

Human activities are the driving factors behind global warming that has been observed since last century [3]. Greenhouse gasses and deforestation will lead to an increase in global temperature at the end of this century of approximately 2.5 °C to 4.5 °C compared to pre-industrial levels if no drastic measures are taken [4], [5]. Consequently, global warming will result in the rise of sea-levels, collapse of ecosystems, and more extreme and frequent weather. To limit the rise in temperature to 1.5 °C, nations have endorsed the Paris Agreement in 2015, in which they agree to achieve net-zero carbon dioxide emissions by 2050 [6]. In order to achieve this, it is expected that wind energy will account for one-third of the global electricity demand by 2050 [7].

To produce renewable electricity, wind turbines extract momentum from the wind, and by doing so produce wakes. Wakes are the regions of turbulent flows behind wind turbines that are characterized by a reduced wind velocity and increased turbulence intensity. The reduced wind velocity, also called the wake deficit, recovers as wind travels away from the turbine, until it regains its original velocity and uniformity. The recovery is caused by the turbulence in the wake, which induces mixing of the wake with surrounding air and redistributes momentum through the wake [8].

If any wind turbine is located inside another wind turbine's wake, the former wind turbine is affected in two ways [8]. Firstly, the affected wind turbine produces less power, since the wind has a decreased velocity and thus contains less momentum. The reduced power output can lead to a 10-20% reduction in annual energy production by wind farms [9]. Secondly, due to the elevated turbulence level in the wake, the wind turbine experiences increased fatigue loads, which decreases their lifespan. These energy losses and fatigue loads are influenced by the layout of a wind farm, terrain features, and atmospheric conditions. Therefore, to maximize the energy output of a wind farm, it is crucial to develop models that can accurately simulate the interactions between wind turbines, their wakes, the terrain and atmospheric conditions [10].

Many models exist that are capable of simulating wind turbine wakes. For the purpose of wind farm design, Reynolds Averaged Navier–Stokes (RANS) based models are the most suitable. Wind turbine wake models are used to predict the wake deficit, wake recovery, and turbulence level of wind turbine wakes. One can distinct four kinds of wake simulations, which all differ in computational cost and accuracy. Firstly, Direct Numerical Simulation (DNS) is the most precise model, since it simulates all scales of motion. To do so, it requires a very fine spatial and temporal resolution, making DNS computationally expensive and unsuitable for engineering purposes. Secondly, Large Eddy Simulations (LES) are less computationally expensive than DNS, while still yielding good results that agree well with experimental and field data. However, they are still too costly to be practical for engineering purposes [11]. Instead, they are used to validate results from lower fidelity models. Thirdly, simple analytical empirical wake models exist that are very efficient, and have been widely used to compute single wind turbine wakes. However, the simulations of wind farms require higher fidelity models that are proficient in capturing the physics involved in wind turbine wakes [12]. Lastly, RANS models are a lower fidelity type of modeling than LES, while producing superior results over analytical models. Therefore, they are the standard in the wind industry [7].

RANS models require a turbulence model to compute the influence of turbulent momentum transfer to the mean flow, for which the standard k–ε model is most widely used for wind turbine applications. However, it is known that the standard k–ε model greatly overpredicts the eddy viscosity in the near wake of a turbine, which leads to an overestimation of mixing and wake recovery [13]. Therefore, researchers have proposed modifications to the standard k–ε model to improve its agreement with experimental, field, and LES data.

Two modifications are used in this thesis. The first is the k–ε–f_P model, proposed by Laan et al. [14]. This extension replaces the constant C_μ in the eddy viscosity definition with a variable coefficient $C_\mu^* = C_\mu f_P$. The correction factor f_P is derived from the nonlinear eddy viscosity model framework and reduces the eddy viscosity in regions of high shear, such as the wake edges, where the standard model is known to overpredict turbulent mixing. Laan et al. [14] validated this model against LES and field data for single and double wake configurations and showed that it significantly improves velocity deficit predictions. The second modification is the extended k–ε model with a sink term S_k in the turbulent kinetic energy equation, derived by Zehtabiyan-Rezaie and Abkar [7]. This term accounts for the extraction of turbulent kinetic energy by the actuator disk forces. The S_k term is derived analytically from the actuator disk force and requires no empirical calibration constants. Both modifications have been developed and validated only within fully elliptic three-dimensional RANS solvers, and their behaviour in a parabolic marching framework has not been studied.

One of the most widely used parabolic RANS models for wind turbine wake prediction is the Ainslie Wake Model (AWM) [15]. This model simplifies the RANS equations by assuming axisymmetry, neglecting axial diffusion and the pressure term. The solution is then marched downstream column by column. This makes it computationally very efficient, but

the omission of the pressure term introduces a limitation in its accuracy. The Forced Ainslie Wake Model (FAWM), proposed by Paddeu [16] and further developed by Warncke et al. [2], resolves this. It does so by reintroducing part of the actuator disk force in the momentum equation, while preserving the parabolic marching scheme. However, the current FAWM implementation uses a constant eddy viscosity for the turbulence closure. Since the original Ainslie eddy viscosity model causes numerical instabilities when coupled with the FAWM [2]. A constant eddy viscosity is not able to capture the spatial variation of turbulent mixing in the wake. This limits the model's agreement with high-fidelity reference data, especially in the far wake where turbulent diffusion governs the recovery process.

This leads to a clear research gap. Extended turbulence models that address the shortcomings of the standard k–ε model exist and have been validated in elliptic RANS solvers, but none of them have been coupled with a parabolic wake model such as the FAWM. Three turbulence closures are therefore selected for implementation: the standard k–ε model, which serves as a baseline, the k–ε–f_P model, and the extended k–ε model with the S_k sink term. The research questions of this thesis are:

1. Can the standard k–ε, k–ε–f_P, and extended k–ε (with S_k sink term) closures be successfully integrated into the FAWM parabolic solver, and do the extended models improve velocity deficit and turbulence predictions compared to the standard k–ε?
2. How do the FAWM predictions with these turbulence closures compare against high-fidelity large eddy simulation reference data?

To answer these questions, the three turbulence closures are implemented in a finite volume discretisation of the parabolized axisymmetric k–ε transport equations. They are then coupled with the existing FAWM solver through a Picard iteration scheme. The implementation is verified in three steps. First a canonical turbulent decay test case is used to verify the coupling between the k- and ε-equations. Secondly, the Method of Manufactured Solutions is used to verify the order of accuracy of the coupled model. Lastly, a self-similar coflowing jet simulation is used as an additional check to verify that the solver reproduces the expected physical behaviour. The validated solver is then used to simulate the wake of a DTU 10MW reference wind turbine [17] using four differen operating conditions. The results are compared against high-fidelity LES data generated with the YALES2 solver [18].

The thesis is structured as follows. Chapter 2 provides the theoretical background. Chapter 3 describes the development of the parabolized k–ε model. Chapter 4 presents the verification of the numerical implementation. Chapter 5 shows the validation results against LES data for the four operating conditions, discusses numerical stability issues that were encountered, and compares the performance of the three turbulence closures. Finally, Chapter 6 presents the conclusions and recommendations for future work.

2 Theoretical Background

This chapter presents the theoretical background for coupling two-equation turbulence models with the Forced Ainslie Wake Model.

Section 2.1 introduces the three main types of turbulence simulation approaches and explains why the parabolized RANS equations are the appropriate for computationally efficient wake modeling. Section 2.2 reviews the Ainslie Wake Model and its extension, the Forced Ainslie Wake Model, which reintroduces the actuator disk pressure gradient while preserving the parabolic marching scheme. With the pressure treatment resolved, the turbulence closure becomes the main remaining modelling challenge.

Several options for the turbulence closure are addressed in Section 2.3. Starting from the Reynolds stress transport equations, the derivation chain through the algebraic stress model and nonlinear eddy viscosity models down to the k-ε-f_P model with variable C_μ^* is shown in detail. The extended k-ε model with the S_k sink term is presented as an alternative approach. Finally, Section 2.4 summarizes the shortcomings of existing approaches and formulates the research questions that this thesis aims to answer.

2.1 Turbulence Modeling

The flow inside a wind turbine's wake is always highly turbulent, which means it consists of irregular and fluctuating velocity fields in both space and time [19]. A flow can be either turbulent or laminar, and this depends on the balance between the inertial and viscous forces. This balance is quantified by the Reynolds number:

$$Re = \frac{Ul}{\nu}, \tag{2.1}$$

where U is the velocity scale, l is the length scale and ν is the kinematic viscosity. For large wind turbines, Re is on the order of millions, indicating high turbulence intensity. This section introduces common approaches for modeling such flows: direct numerical simulation (DNS, Section 2.1.1), large eddy simulation (LES, Section 2.1.2), the Reynolds Averaged Navier-Stokes equations (RANS, Section 2.1.3) and the parabolized Navier-Stokes equations (PNS, Section 2.1.4).

2.1.1 Direct Numerical Simulation

DNS aims to resolve all the spatial and temporal scales of a turbulent flow, and does so by directly solving the Navier-Stokes equations [19]. This method yields the most accurate results when simulating turbulent flows, but also the most computationally expensive.

The smallest characteristic scales of turbulent flows are called the Kolmogorov microscales [20], and they are defined as:

$$\eta = \left(\frac{\nu^3}{\varepsilon}\right)^{1/4}, \quad \tau_\eta = \sqrt{\frac{\nu}{\varepsilon}}, \quad u_\eta = (\nu\varepsilon)^{1/4}, \tag{2.2}$$

where η is the Kolmogorov length scale, τ_η is the Kolmogorov time scale, u_η is the Kolmogorov velocity scale and ε is the average rate of dissipation of turbulent kinetic energy ($\frac{dk}{dt}$). They are based on the Kolmogorov hypothesis. This hypothesis states that at high Reynolds numbers, the smallest turbulent motions are statistically isotropic and depend only on ν and ε.

DNS computes the instantaneous velocity field by solving the Navier-Stokes equations:

$$\begin{aligned} \frac{\partial \rho}{\partial t} + \frac{\partial \rho U_i}{\partial x_i} &= 0, \\ \frac{\partial (\rho U_i)}{\partial t} + \frac{\partial (\rho U_i U_j)}{\partial x_j} &= -\frac{\partial P}{\partial x_i} + \mu \frac{\partial^2 U_i}{\partial x_j^2}, \end{aligned} \tag{2.3}$$

where ρ is the fluid density, U_i are the instantaneous velocity components and P is the instantaneous pressure.

In order to resolve the smallest turbulent scales, the computational grid must be as fine as the Kolmogorov length scale. The number of grid points in one direction is then approximately l/η, and in three dimensions:

$$N_L^3 = \left(\frac{l}{\eta}\right)^3 \sim Re^{9/4}. \tag{2.4}$$

This scaling shows that the computational cost grows rapidly with Reynolds number. For flows around wind turbines, where Re is on the order of millions, DNS would require an impractically large number of grid cells and time steps. Consequently, DNS is not feasible for wind turbine wake modeling.

2.1.2 Large Eddy Simulation

LES is a turbulence modeling approach that resolves the large, energy-containing eddies in a flow while modeling the smaller scales [19]. Unlike DNS, which computes all scales of turbulence, LES applies a spatial filtering operation to the Navier-Stokes equations. This process separates the flow into resolved large-scale motions and subgrid-scale (SGS) motions. The large scales are computed directly, while the SGS effects are represented using a turbulence model.

The filtered Navier-Stokes equations for LES are:

$$\frac{\partial\left(\rho\overline{U}_i\right)}{\partial t}+\frac{\partial\left(\rho\overline{U}_i\overline{U}_j\right)}{\partial x_j}=-\frac{\partial\overline{P}}{\partial x_i}+\mu\frac{\partial^2\overline{U}_i}{\partial x_j^2}-\rho\frac{\partial\tau_{ij}^{\text{SGS}}}{\partial x_j}, \tag{2.5}$$

where $\overline{U}_i$ are the filtered velocity components, $\overline{P}$ is the filtered pressure and $\tau_{ij}^{\text{SGS}}=\overline{U_iU_j}-\overline{U}_i\overline{U}_j$ is the subgrid-scale stress tensor, representing the effect of unresolved scales.

To close the equations, a subgrid-scale model is required. The most common approach is the Smagorinsky model, which relates SGS stresses to the strain-rate of the resolved scales.

LES has a lower accuracy than DNS, but a much better computational cost. By resolving the large scales, which contain most of the turbulent kinetic energy and are highly anisotropic, LES captures the essential physics of turbulence more accurately than RANS models. However, LES still requires fine grids and small time steps, especially near walls, making it computationally expensive for highly turbulent flows such as wind turbine wakes. In wind turbine engineering, LES is often used as a high-fidelity reference to validate lower-fidelity models such as RANS [21].

2.1.3 Reynolds Averaged Navier-Stokes Equations

The RANS approach is based on decomposing the instantaneous flow variables into a mean component and a fluctuating component using Reynolds decomposition [19]. By applying Reynolds averaging to the Navier-Stokes equations, the Reynolds averaged continuity and momentum equations are obtained:

$$\begin{aligned}\frac{\partial\left(\rho U_i\right)}{\partial x_i}&=0,\\ \frac{\partial\left(\rho U_iU_j\right)}{\partial x_j}&=-\frac{\partial P}{\partial x_i}+\mu\frac{\partial^2U_i}{\partial x_j^2}-\frac{\partial\left(\rho\overline{u_i'u_j'}\right)}{\partial x_j},\end{aligned} \tag{2.6}$$

where U_i and P denote the mean velocity components and mean pressure, respectively. The term $\overline{u_i'u_j'}$ is the Reynolds stress tensor, which represents the momentum transport caused by turbulent fluctuations.

Due to the unknown Reynolds stresses, there are now more unknowns than equations, which makes the system unclosed. This is known as the turbulence closure problem. To close the system, a turbulence model is required that expresses the Reynolds stresses in terms of known quantities. The most widely used class of turbulence models are the linear eddy viscosity models, which employ the Boussinesq hypothesis [22] to relate the Reynolds stresses to the mean rate of strain tensor:

$$-\overline{u_i'u_j'}=2\nu_TS_{ij}-\frac{2}{3}k\delta_{ij}, \tag{2.7}$$

where ν_T is the kinematic eddy viscosity and $S_{ij}=\frac{1}{2}\left(\frac{\partial U_i}{\partial x_j}+\frac{\partial U_j}{\partial x_i}\right)$ is the mean rate of strain tensor. This hypothesis draws an analogy between turbulent momentum transport and molecular diffusion, assuming that the Reynolds stresses are proportional to the local mean velocity gradients, with the eddy viscosity acting as the proportionality factor. The assumptions and implications of the Boussinesq hypothesis are discussed in detail in Section 2.3.1.

Two important flow parameters appear in the RANS-equations (Equation 2.7): the turbulent kinetic energy k and the eddy viscosity ν_T. The turbulent kinetic energy is defined as half the trace of the Reynolds stress tensor:

$$k=\frac{1}{2}\overline{u_i'u_i'}. \tag{2.8}$$

k represents the kinetic energy per unit mass of all the turbulent velocity fluctuations in the flow. The rate at which this energy is dissipated by molecular viscosity is given by the dissipation rate:

$$\varepsilon = \nu \overline{\frac{\partial u_i'}{\partial x_k} \frac{\partial u_i'}{\partial x_k}}, \tag{2.9}$$

This destruction occurs at the smallest scales of the turbulent motions due to viscosity. Together, k and ε are used to set the characteristic velocity scale ($k^{1/2}$), length scale ($k^{3/2}/\varepsilon$) and time scale (k/ε) of the turbulent flow.

Through dimensional analysis, the eddy viscosity can be expressed as a function of k and ε [23], [24]:

$$\nu_T = C_\mu \frac{k^2}{\varepsilon}, \tag{2.10}$$

where C_μ is a model constant. Substituting this relation together with Equation 2.7 into the RANS momentum equation (Equation 2.6) closes the system of equations of the RANS framework.

The distributions of k and ε are calculated through transport equations. An exact transport equation for k can be derived by contracting the Reynolds stress transport equations. After modeling the unknown correlations using the gradient-diffusion assumption and the Boussinesq hypothesis, the modeled k-equation becomes:

$$\frac{\partial k}{\partial t} + U_j \frac{\partial k}{\partial x_j} = \underbrace{\frac{\partial}{\partial x_j}\left[\left(\nu + \frac{\nu_T}{\sigma_k}\right)\frac{\partial k}{\partial x_j}\right]}_{\text{diffusion}} + \underbrace{\mathcal{P}}_{\text{production}} - \underbrace{\varepsilon}_{\text{dissipation}}, \tag{2.11}$$

where $\mathcal{P} = -\overline{u_i' u_j'} \frac{\partial U_i}{\partial x_j}$ is the production of turbulent kinetic energy, caused by the transfer of energy from the mean flow to the turbulent motions, and σ_k is a closure coefficient. The derivation involves modeling both the turbulent transport and pressure diffusion terms through a gradient-diffusion approximation, which assumes that these terms have the same effect as molecular diffusion, thus transporting k down its gradient.

An exact equation for ε also exists, but it is far more complex, because it contains double and triple correlation terms that cannot be measured or modeled individually. The standard approach, introduced by Jones and Launder [25] and further refined by Launder and Sharma [26], is to construct a modeled equation for ε that has a similar structure as the k-equation:

$$\frac{\partial \varepsilon}{\partial t} + U_j \frac{\partial \varepsilon}{\partial x_j} = \frac{\partial}{\partial x_j}\left[\left(\nu + \frac{\nu_T}{\sigma_\varepsilon}\right)\frac{\partial \varepsilon}{\partial x_j}\right] + C_{\varepsilon 1}\frac{\varepsilon}{k}\mathcal{P} - C_{\varepsilon 2}\frac{\varepsilon^2}{k}, \tag{2.12}$$

where σ_ε, $C_{\varepsilon 1}$ and $C_{\varepsilon 2}$ are closure coefficients. It is based on the assumption that ε is produced in proportion to $\mathcal{P}$ (scaled by ε/k on dimensional grounds) and destructed through a term analogous to the dissipation of k ε^2/k. The ratio ε/k can be interpreted as the inverse of the turbulent time scale, which ensures that the production and destruction of ε evolve on the same time scale as the turbulence itself.

Together, Equation 2.7, Equation 2.10, Equation 2.11 and Equation 2.12 form the standard k-ε model, which is widely used in engineering and in wind energy applications. They are widely used in engineering because they offer a good trade-off between accuracy and computational cost. While they do not give the instantaneous flow fields, they give reasonable results of the mean flow with much less computational costs than LES or DNS.

2.1.4 Parabolized Navier-Stokes Equations

The RANS equations described in Section 2.1.3 are obtained by time-averaging the Navier-Stokes equations. This process removes the temporal gradient in the equations. However, the equations remain parabolic, since information propagates in all possible directions. This means that any location in the flow field can influence the rest of the flow field [27]. This makes it elliptic problems very computationally expensive to solve.

Classifying PDE's as elliptic, parabolized and hypoerbolic is based on the eigenvalues of the coefficient matrix associated with diffusion terms. For a system in two spatial dimensions, the equation is elliptic when the determinant of this matrix is strictly positive, hyperbolic when it is negative, and parabolic when it equals zero. In the RANS equations, the diffusion terms in all spatial directions make the determinant strictly positive, resulting in an elliptic system.

The parabolized Navier-Stokes (PNS) equations are obtained by modifying the diffusion terms such that the determinant of the coefficient matrix becomes zero. This makes the governing equations parabolic [28]. This can be achieved by neglecting the diffusion terms in the main direction of transport, which is justified when convective transport dominates

over diffusive transport in that direction. In other words, when the gradients perpendicular to the main flow direction are much larger than those along it, the gradients in the direction of the main flow can be neglected.

Parabolizing a PDE has as advantage that information is only transported in one direction. Therefore, it becomes possible to march through the solution step by step, instead of solving for the entire domain at once. This results in a large reduction in computational cost and memory requirements. However, this simplification also means that errors at one location move downstream and accumulate, which makes parabolized models more prone to numerical instabilities [29].

The parabolic assumption is well suited for wind turbine wake flows. In the turbine's wake, the flow is in the streamwise direction and the velocity deficit evolves gradually in downstream direction. Radial gradients are much larger than the axial gradients in the far-wake, which makes it justified to neglect streamwise diffusion. Mittal [30], [31] developed a parabolized approach for wind turbine flows. They showed that the parabolic approach can calculate the most important wake characteristics in a much shorter time span than elliptic RANS. Another simplification can be made by omitting the pressure term, which removes the elliptic pressure Poisson equation. While this invalidates the model in the region close around wind turbine where pressure gradients are large, it makes it a fully parabolic model. Cabezón et al. [32] proposed a semi-parabolic approach that retains the pressure gradient in the cross-stream plane while marching in the streamwise direction, offering a middle ground between the full elliptic RANS and the fully parabolic Ainslie model.

By further assuming axisymmetry and transforming to cylindrical coordinates, one arrives at the Ainslie wake model [15], which is one of the most widely used engineering models for wind turbine wake prediction. The derivation and formulation of this model are discussed in detail in Section 2.2.1.

2.2 Wind Turbine Wake Modeling

2.2.1 Ainslie Wake Model

The Ainslie Wake Model (AWM), developed by Ainslie in 1988 [15], provides a method of calculating the velocity deficit in a wind turbine wake by using a simplified form of the RANS equations. The derivation begins with the steady incompressible RANS equations in cylindrical coordinates and assumes axisymmetric flow. This assumption removes the azimuthal velocity component and its derivatives from the formulation. By doing so it reduces the number of transport equations from three to two, since the transport equation for the azimuthal momentum is no longer required. Furthermore, axisymmetry makes it possible for the axial and radial velocity components to be related through the Stokes stream function, which further reduces the problem to a single transport equation: the axial momentum equation.

Next to this, the axial pressure gradient is neglected. This makes the model invalid in the near-wake region, where pressure gradients are large. Farther downstream, radial gradients become much larger than the axial gradients and the latter are thus ignored. This turns the axial momentum equation from elliptic to parabolic. Lastly, since a wind turbine wake is highly turbulent, molecular viscosity is also neglected. This yields Ainslie's model:

$$U\frac{\partial U}{\partial x} + V\frac{\partial U}{\partial r} = -\frac{1}{r}\frac{\partial(r\overline{u'v'})}{\partial r}, \tag{2.13}$$

where U and V are the mean axial and radial velocity components and $\overline{u'v'}$ is the Reynolds shear stress.

Ainslie gives initial conditions for the model at about two rotor diameters downstream, where the initial centerline velocity deficit D_M and the initial wake width b are given as functions of the thrust coefficient C_T and the ambient turbulence intensity I:

$$D_M = C_T - 0.05 - (16C_T - 0.5)\frac{I}{1000}, \quad b = \left[\frac{3.56C_T}{8D_M(1 - 0.5D_M)}\right]^{1/2}. \tag{2.14}$$

A Gaussian velocity deficit profile is assumed at this initial station, and the solution is then marched downstream.

2.2.2 Ainslie Eddy Viscosity Model

The Reynolds shear stress in the right hand side of Ainslie's equation (Equation 2.13) is modeled using the Boussinesq hypothesis (Section 2.3.1), in which the Reynolds shear stress is related to the mean shear through the eddy viscosity [15]. In the AWM, this eddy viscosity is calculated through the characteristic velocity and length scales of the wake, together with a contribution from the atmospheric turbulence. Using Boussinesq hypothesis yields the final result of

AWM:

$$-\overline{u'v'} = \nu_T \frac{\partial U}{\partial r} \quad \text{with} \quad \nu_T(x) = l_w(x) v_w(x) + \varepsilon_\alpha,$$
$$U\frac{\partial U}{\partial x} + V\frac{\partial U}{\partial r} = \nu_T \frac{1}{r}\frac{\partial}{\partial r}\left(r\frac{\partial U}{\partial r}\right). \tag{2.15}$$

In these equations, ν_T is the eddy viscosity which is a function of a length scale (l_w), a velocity scale (v_w) and the ambient eddy viscosity (ε_α).

Because the near wake has a strong imbalance between the mean-flow gradients and the developing turbulence field, the equilibrium assumption made by the eddy viscosity is not valid there. Consequently, a modified formulation is used in the near-wake region. The IEC 61400-1 standard [33] defines the eddy viscosity as a function of the non-dimensional downstream coordinate $\tilde{x} = x/D$, the wake radius R_W and two filter functions F_1 and F_2. The filter functions are obtained by fitting the model to field measurements. For example, Larsen et al. [34] calibrated these functions using data from the Egmond aan Zee wind farm.

2.2.3 Forced Ainslie Wake Model

As discussed in Section 2.2.1, the Ainslie Wake Model has very low computational costs, because it omits the pressure term and axial diffusion from the RANS equations. However, this comes at a cost: prescribing inflow conditions for an already expanded wake requires wake expansion models that do not preserve the intrinsic conservation of mass and momentum for the full computational domain. This leads to systematic overprediction of momentum deficits and necessitates empirical corrections.

The Forced Ainslie Wake Model (FAWM), proposed by Paddeu [16] and further developed by Warncke et al. [2], reintroduces into the axial momentum equation a part of the pressure that is caused by the actuator disk forcing. This is done by decomposing the pressure field into two contributions through the pressure Poisson equation:

$$\nabla^2 p = \underbrace{-\rho \nabla \cdot [\nabla \cdot (\bar{u} \otimes \bar{u})]}_{\nabla^2 p_u} + \underbrace{\nabla \cdot \bar{f}}_{\nabla^2 p_f}, \tag{2.16}$$

where $\nabla^2 p_u$ is the pressure Poisson equation for the velocity-induced contribution and $\nabla^2 p_f$ is the contribution from the applied forcing $\bar{f}$. The forcing contribution p_f depends only on the prescribed actuator disk force and can therefore be solved independently of the velocity field. This means that the Poisson equation for p_f can be solved analytically, without effecting the parabolized nature of the axial momentum equation.

Once computed, the axial component of the pressure gradient associated with p_f is substituted into the right-hand side of the momentum equation as a source term. This yields the FAWM transport equation [2]:

$$U\frac{\partial U}{\partial x} + V\frac{\partial U}{\partial r} = \frac{1}{\rho} f_{AD,x} + \nu_T \frac{1}{r}\frac{\partial}{\partial r}\left(r\frac{\partial U}{\partial r}\right), \tag{2.17}$$

where $f_{AD,x}$ is the axial forcing term, derived from the actuator disk. Since this term is a precomputed source that does not introduce any new spatial derivatives, the transport equation remains parabolic, and the marching solution procedure is preserved.

It should be noted that only the forcing contribution p_f is accounted for in FAWM, since the velocity-induced pressure p_u is still neglected. In reality, there is a feedback loop between the pressure and velocity fields, but this feedback loop is now omitted. The forcing term is computed once from the actuator disk model and is not iteratively updated as the wake velocity evolves downstream. This decoupling is what allows the problem to remain parabolic and compatible with the marching scheme, but it also means that pressure effects arising from the wake itself (such as the streamwise pressure recovery in the near-wake) are not captured by the model.

Despite this downside of the model, FAWM significantly improves the physical consistency of the wake model compared to the original AWM. The model is able to conserve the applied thrust force in the integral momentum deficit to very small relative errors [2]. This represents an improvement of several orders of magnitude compared to other inflow models used in the standard AWM. Comparisons between FAWM and LES data show good qualitative agreement in near-wake velocity deficits and wake expansion, though in the far-wake the use of a simplified eddy viscosity model causes larger discrepancies. Therefore, it is crucial to develop a more appropriate turbulence model that is compatable with the FAWM.

2.2.4 Siemens Energy Reference Implementation

The implementation of the FAWM developed at Siemens Energy [2] is used in this thesis to couple with the turbulence model that will be developed. This implementation solves the axial momentum equation on a staggered finite volume mesh in the r–x plane. Furthermore, the radial velocity V is eliminated in the momentum equation by substituting a radial integral of the continuity equation. The nonlinear system of equations is solved via a Newton–Raphson iteration. A symmetry boundary condition is imposed at $r = 0$ and a Robin boundary condition is applied at $r = R_{\text{max}}$ for the axial velocity U. The Robin condition combines a Dirichlet contribution based on the freestream velocity with a Neumann contribution. A first-order upwind scheme is used to discretize the axial convection term, which results in a stable solver. The radial convection term and the radial diffusion term are both discretised with central differences. This combination gives a scheme that is second-order accurate in the radial direction and first-order accurate in the axial direction on uniform grids. The eddy viscosity is prescribed as a single constant value over the entire domain, since the IEC 61400–1 prescribed eddy viscosity model caused stability issues when coupled with the FAWM. The need for a turbulence model that is compatible with the forcing term is the main motivation for the parabolised turbulence model developed in this thesis.

2.3 Turbulence Closure Models

In this section a short overview is given of a different variety of turbulence closure models relevant to this thesis. First, the Boussinesq hypothesis is explained. Then the derivation that underpins the k-ε-f_P model is reviewed. Finally, the standard k-ε model and some of its proposed extensions for wind turbine wake flows are discussed.

2.3.1 Boussinesq Hypothesis

Linear eddy viscosity models use the Boussinesq hypothesis [22] to relate the Reynolds stresses to the mean velocity gradients, by making an analogy between molecular diffusion and turbulent momentum transport. The hypothesis assumes that the Reynolds stresses are proportional to the local mean strain-rate [35]:

$$\overline{u_i' u_j'} = -2\nu_T S_{ij}, \tag{2.18}$$

where ν_T is the eddy viscosity and $S_{ij} = \frac{1}{2}\left(\frac{\partial U_i}{\partial x_j} + \frac{\partial U_j}{\partial x_i}\right)$ is the mean rate of strain tensor. Since the trace of the Reynolds stress tensor equals twice the turbulent kinetic energy, $\overline{u_i' u_i'} \equiv 2k$, while the trace of the right-hand side vanishes due to continuity, Equation 2.18 is modified to:

$$\overline{u_i' u_j'} = -2\nu_T S_{ij} + \frac{2}{3} k \delta_{ij}. \tag{2.19}$$

Note that in Section 2.1.3, the same relation was written as $-\overline{u_i' u_j'} = 2\nu_T S_{ij} - \frac{2}{3} k \delta_{ij}$ (Equation 2.7).

Réthoré [36] has presented an analysis that highlights the assumptions underlying the Boussinesq hypothesis. The analysis studies a particle n that passes through a fixed point x at time $t = t^n$. The particle's instantaneous velocity is decomposed into its ensemble average value and a fluctuating component:

$$U_i(x, t^n) = \overline{U_i}(x) + u_i'(x, t^n). \tag{2.20}$$

To study turbulent momentum transport, the flow differences between the particle at point x and an upstream point x_p^n are analyzed, defined by the time $t = t_p^n < t^n$:

$$U_i(x_p^n, t_p^n) = \overline{U_i}(x_p^n) + u_i'(x_p^n, t_p^n), \tag{2.21}$$

where $\overline{U_i}(x_p^n)$ is the ensemble average velocity at position x_p^n and therefore depends on the particle considered, as illustrated in Figure 2.1. The superscript ^{n} is omitted hereafter for conciseness. Three assumptions are made from Equation 2.21:

1. There exists a time $\tau = t - t_p$ small enough so that a particle's momentum is conserved: $U(x_p, t_p) = U(x, t)$.
2. The time τ is large enough so that the fluctuating components at the two points are uncorrelated: $\overline{u_i'(x_p, t_p) u_j'(x, t)} = 0$.
3. The mean velocity components between x and x_p change linearly:

$$\begin{aligned} \overline{U_i}(x_p) &= \overline{U_i}(x) - L_{p,j} \frac{\partial \overline{U_i}}{\partial x_j}(x), \quad \text{with} \\ L_{p,j} &= \int_{t_p}^{t} U_j\left(x(s), s\right) ds = x_j - x_{p,j}. \end{aligned} \tag{2.22}$$

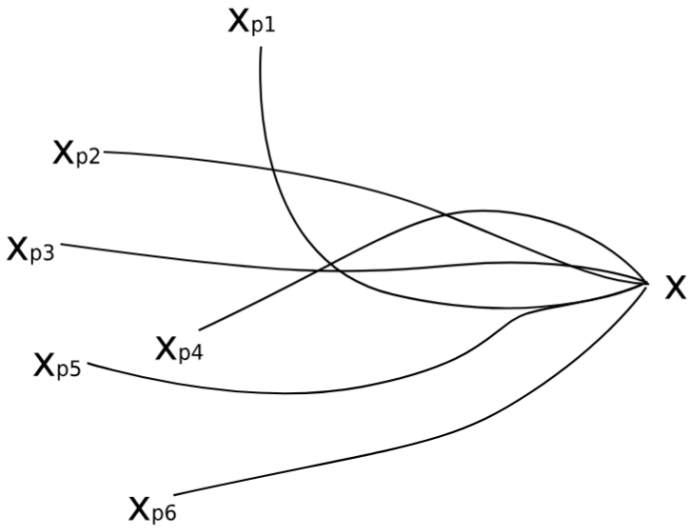

Figure 2.1: Illustration of different paths followed by particles passing through the position x [36].

Subtracting Equation 2.21 from Equation 2.20, applying assumptions 1–3, multiplying with $u'_j(x,t)$ and Reynolds averaging, and assuming that local fluctuation components are mainly correlated with their respective distances ($\overline{u'_j L_{p,k}} \neq 0$ only if $j = k$), gives:

$$\begin{aligned} \overline{u'_i u'_j} &= -\nu_{t,ij} \frac{\partial \overline{U_i}}{\partial x_j}, \\ \nu_{t,ij} &= \overline{\int_{t_p}^{t} u'_j(x,t) u'_i(x(s),s) ds} = \overline{u'_j(x,t) L_{p,j}}. \end{aligned} \tag{2.23}$$

Enforcing tensor symmetry, the definition of k, and assuming the eddy viscosity is isotropic, the Boussinesq hypothesis (Equation 2.19) is recovered. This derivation makes explicit that the hypothesis requires: (1) a separation of time scales between momentum conservation and decorrelation of fluctuations, (2) a locally linear mean velocity field, and (3) an isotropic eddy viscosity. In wind turbine wakes, where the mean velocity field exhibits strong spatial gradients and the turbulence is highly anisotropic, these assumptions are violated.

The Boussinesq hypothesis reduces the turbulence closure problem from six unknown parameters to only one parameter: the eddy viscosity ν_T. To determine this parameter, a lot of different models exist. The simplest are algebraic (zero-equation) models, such as Prandtl's mixing-length model [37], which calculated ν_T directly through local flow quantities without solving additional transport equations. One-equation models solve one transport equation for k and using an algebraic length scale to compute $\nu_T = k^{1/2} l$ [24], [38]. Other variants instead transport ν_T, such as the Spalart–Allmaras model [39]. These models are not able to determine the turbulence length scale from the flow itself. Therefore, two-equation models have been developed that solve an additional transport equations for a second turbulence variable, thereby fully determining ν_T without prescribing a length scale.

Two-equation models combine the Boussinesq hypothesis with transport equations for k and a second variable that sets the turbulence length scale. The most common models use either the dissipation rate ε (giving $\nu_T \sim k^2/\varepsilon$) or the specific dissipation rate ω (giving $\nu_T \sim k/\omega$) [24]. The k-ω model, first proposed by Kolmogorov [23] and later refined by Wilcox [40], performs better than the k-ε model for wall-bounded flows with adverse pressure gradients but is less commonly used in wind energy applications. This thesis uses the k-ε model, which is discussed below.

2.3.2 Standard k-ε Model

The standard k-ε model, presented by Launder and Sharma [26], is one of the most widely used turbulence closures in wind energy applications. It uses the Boussinesq hypothesis (Equation 2.19) together with modeled transport equations for k and ε. The exact ε-equation contains several double and triple correlation terms that cannot be accurately measured. The standard approach is therefore to construct a modeled equation that mirrors the structure of the k-equation:

$$\frac{\partial k}{\partial t} + U_j \frac{\partial k}{\partial x_j} = \frac{\partial}{\partial x_j}\left(\left(\nu + \frac{\nu_T}{\sigma_k}\right)\frac{\partial k}{\partial x_j}\right) + \tau_{ij}\frac{\partial U_i}{\partial x_j} - \varepsilon, \tag{2.24a}$$

$$\frac{\partial \varepsilon}{\partial t} + U_j \frac{\partial \varepsilon}{\partial x_j} = \frac{\partial}{\partial x_j}\left(\left(\nu + \frac{\nu_T}{\sigma_\varepsilon}\right)\frac{\partial \varepsilon}{\partial x_j}\right) + C_{\varepsilon 1}\frac{\varepsilon}{k}\tau_{ij}\frac{\partial U_i}{\partial x_j} - C_{\varepsilon 2}\frac{\varepsilon^2}{k}. \tag{2.24b}$$

where σ_ε, $C_{\varepsilon 1}$, and $C_{\varepsilon 2}$ are closure coefficients. The model constant values generally used for wind energy applications are $\sigma_k = 1$, $\sigma_\varepsilon = 1.3$, $C_{\varepsilon 1} = 1.44$, $C_{\varepsilon 2} = 1.92$ and $C_\mu = 0.03$ [41]. In the k-ε model, the eddy viscosity is given by $\nu_T = C_\mu k^2/\varepsilon$.

The theoretical basis of the standard k-ε model relies on the assumption of a linear relationship between the Reynolds stresses and strain-rate tensors. However, this assumption becomes problematic in wind turbine wake regions where the eddy viscosity concept is invalidated [36]. Cabezón et al. [42] compared the standard k-ε, realizable k-ε and Reynolds Stress Model for single wind turbine wakes and found that all models overpredict wake recovery, although the realizable variant with its variable C_μ performs somewhat better. The standard model was not specifically designed for wake flows. This causes its application to turbine wakes to reveal significant limitations. For instance, it is not able to capture the non-local mixing phenomena characteristic of atmospheric wake dispersion [43]. Therefore, researchers have developed extensions to the standard model.

2.3.3 Realizability

In flow regions with high shear, the Reynolds stresses predicted by the linear eddy viscosity relation can violate physical bounds. Schumann [44] showed that the Reynolds stresses computed by eddy viscosity models can violate the so-called realizability conditions. These are non-negative normal stresses ($\overline{u_i' u_i'} \geq 0$), the Schwarz inequality ($\overline{u_i' u_j'}^2 \leq \overline{u_i' u_i'}\,\overline{u_j' u_j'}$), and a non-negative determinant of the Reynolds stress tensor. Figure 2.2 shows that these conditions are violated in a large part of a wind turbine's wake when using the standard k-ε model.

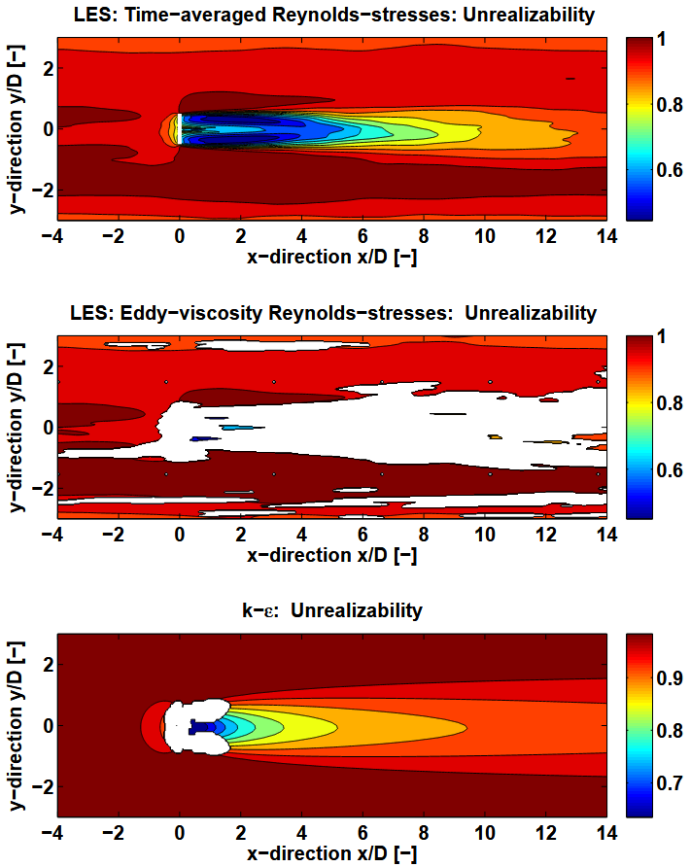

Figure 2.2: Realizability criterion at hub height for LES and k-ε. The axial velocity is represented with the colours. The white colour illustrates the regions where the Schwarz inequalities are significantly invalidated. The top plot is based on the time-averaged resolved LES Reynolds stresses $\overline{u_i' u_j'}$. The middle and bottom plots are based on the eddy viscosity concept [36].

2.3.4 From Reynolds Stress Models to Variable C_μ

The realizability violations motivate looking for a model that goes beyond the constant C_μ assumption. This subsection follows the derivation from the full Reynolds Stress Model (RSM) through the Algebraic Stress Model (ASM) and Nonlinear Eddy Viscosity Models (NLEVM) to the variable C_μ concept.

Reynolds Stress Model

The most general RANS closure solves transport equations for the individual Reynolds stresses $\overline{u_i' u_j'}$ directly. The Reynolds stress transport equation is as follows [45]:

$$\frac{\overline{D}}{\overline{D}t}\overline{u_i' u_j'} + \frac{\partial}{\partial x_k} T_{kij} = \mathcal{P}_{ij} + \mathcal{R}_{ij} - \varepsilon_{ij}, \tag{2.25}$$

where T_{kij} is the transport tensor, $\mathcal{P}_{ij}$ is the production tensor, $\mathcal{R}_{ij}$ is the pressure-rate-of-strain tensor and ε_{ij} is the dissipation tensor [46]. By solving six coupled transport equations (in 3D), the RSM captures the full anisotropy of the turbulence without the Boussinesq hypothesis. However, this comes at considerable computational cost. In the parabolic momentum equation (Equation 2.13) used in this thesis, only a single Reynolds stress component $\overline{u'v'}$ exists, so solving six transport equations to obtain one shear stress is therefore unnecessary.

Algebraic Stress Model

The ASM, due to Rodi [47], reduces the Reynolds stress transport equations to algebraic relations by invoking the weak-equilibrium assumption. This assumption states that the normalized Reynolds stress tensor $\overline{u_i' u_j'}/k$ varies slowly along mean-flow streamlines. Neglecting the transport tensor T_{kij} and assuming isotropic dissipation, the RSTE simplifies to:

$$\frac{\tilde{D}\overline{u_i' u_j'}}{\tilde{D}t} = \mathcal{P}_{ij} + \mathcal{R}_{ij} - \frac{2}{3}\varepsilon\delta_{ij}. \tag{2.26}$$

Under weak equilibrium, the material derivative on the left can be replaced by $\frac{\overline{u_i' u_j'}}{k}(\mathcal{P} - \varepsilon)$, yielding the algebraic Reynolds stress equation:

$$\frac{\overline{u_i' u_j'}}{k}(\mathcal{P} - \varepsilon) = \mathcal{P}_{ij} + \mathcal{R}_{ij} - \frac{2}{3}\varepsilon\delta_{ij}. \tag{2.27}$$

This is a set of coupled algebraic equations for the Reynolds stress components, which still requires a model for the pressure-strain tensor $\mathcal{R}_{ij}$.

For the PNS framework, the relevant result is what Equation 2.27 implies for the single shear stress component $\overline{u'v'}$. In a simple shear flow where $\partial U/\partial y$ is the dominant velocity gradient, the Boussinesq hypothesis gives $-\overline{u'v'} = C_\mu(k^2/\varepsilon)\frac{\partial U}{\partial y}$. Extracting $\overline{u'v'}$ from Equation 2.27 and using the LRR-IP model [45] for $\mathcal{R}_{ij}$ yields:

$$C_\mu = \frac{2}{3}\frac{(1 - C_2)\,(C_R - 1 + C_2\mathcal{P}/\varepsilon)}{(C_R - 1 + \mathcal{P}/\varepsilon)^2}, \tag{2.28}$$

where $C_R = 1.8$ and $C_2 = 0.6$ are the Rotta and isotropization-of-production constants. This shows that C_μ is not a constant but depends on $\mathcal{P}/\varepsilon$. In equilibrium ($\mathcal{P}/\varepsilon = 1$), the standard value $C_\mu \approx 0.09$ is recovered. In high-shear regions such as wake edges, where $\mathcal{P}/\varepsilon$ is large, C_μ decreases. This behaviour decreases the eddy viscosity in high-shear regions, limiting turbulent mixing and delaying wake recovery.

Nonlinear Eddy Viscosity Models

The algebraic stress equation (Equation 2.27) can be solved explicitly for the anisotropy tensor $\mathbf{a} = \overline{u_i' u_j'}/k - \frac{2}{3}\delta_{ij}$, yielding the class of NLEVMs. If a linear pressure-strain model is used, the solution takes the form [48], [49]:

$$\mathbf{a} = \sum_{\lambda=1}^{10} G^{(\lambda)} \boldsymbol{T}_{ij}^{(\lambda)}, \tag{2.29}$$

where $\boldsymbol{T}_{ij}^{(\lambda)}$ are tensorially independent tensor groups formed from the normalized strain-rate tensor $\mathbf{s}$ and normalized vorticity tensor $\boldsymbol{\omega}$. And $G^{(\lambda)}$ are scalar coefficient functions. Higher-order truncations ($n > 1$) include more tensor groups and capture nonlinear effects. But van der Laan [50] showed that while NLEVMs improve velocity deficit predictions to levels comparable with LES, they numerical instabilities occur on fine meshes.

Linear truncation ($n = 1$) results in only the first tensor group:

$$\mathbf{a} = G^{(1)}\mathbf{s}, \tag{2.30}$$

which gives $C_\mu^* = -\frac{1}{2}G^{(1)}$, when comparing with the Boussinesq form $\mathbf{a} = -2C_\mu\mathbf{s}$. $G^{(1)}$ is variable in all NLEVMs, since it depends on $\mathcal{P}/\varepsilon$. This means means a variable C_μ that reduces the eddy viscosity in high-shear regions. This is the approach taken by the k-ε-f_P model.

2.3.5 k-ε-f_P Model

The k-ε-f_P model, proposed by van der Laan et al. [14], implements the variable C_μ into the standard k-ε model. The constant C_μ is replaced by a variable C_μ^*.

Derivation from NLEVM

From the linear NLEVM truncation (Equation 2.30), the variable eddy viscosity coefficient is [46]:

$$C_\mu^* = \frac{1}{2}\alpha f_P = -\frac{\tilde{a}_{13}}{\tilde{\sigma}} f_P, \tag{2.31}$$

where $\alpha = -2\tilde{a}_{13}/\tilde{\sigma}$ is determined by calibrating against a simple shear flow. Here, $\tilde{a}_{13}$ is the off-diagonal anisotropy tensor component and $\tilde{\sigma} = \frac{k}{\varepsilon}\frac{\partial U}{\partial z}$ is the normalized shear parameter, both evaluated in the calibration flow. The normalization by $\tilde{\sigma}$ ensures that the model is self-consistent with respect to its calibration flow. In simple homogeneous shear at equilibrium, production balances dissipation ($\mathcal{P}/\varepsilon = 1$), and the approximation $\mathcal{P}/\varepsilon \approx C_\mu\sigma^2$ yields $\tilde{\sigma} = 1/\sqrt{C_\mu} \approx 3.33$. The ratio $\sigma/\tilde{\sigma}$ that appears in the f_P function (Equation 2.33) therefore measures how far the local strain rate differs from the equilibrium value. When $\sigma/\tilde{\sigma} = 1$ the flow matches the calibration conditions and $f_P = 1$, resulting in the standard C_μ. But when the local shear exceeds the equilibrium level ($\sigma/\tilde{\sigma} > 1$), f_P decreases and the eddy viscosity is reduced.

The f_P bounding function

The scalar function f_P was introduced by Apsley and Leschziner [49] as a limiter to prevent the NLEVM coefficients from growing out of bounds. It is defined as follows:

$$f_P = \frac{C_R + \widetilde{\mathcal{P}/\varepsilon} - 1}{C_R + \mathcal{P}/\varepsilon - 1}, \tag{2.32}$$

where $\widetilde{\mathcal{P}/\varepsilon} = 1$ for the calibration flow.

Apsley and Leschziner found that direct use of Equation 2.32 leads to numerical instability. Therefore, they proposed the approximation $\mathcal{P}/\varepsilon \approx f_P C_\mu \sigma^2$, which yields an analytically solvable implicit relation [46], [49]:

$$f_P\left(\sigma/\tilde{\sigma}\right) = \frac{2f_0}{1 + \sqrt{1 + 4f_0(f_0 - 1)\left(\sigma/\tilde{\sigma}\right)^2}}, \quad f_0 = \frac{C_R}{C_R - 1}, \tag{2.33}$$

where $\sigma = \frac{k}{\varepsilon}\sqrt{2S_{ij}S_{ij}}$ is the local normalized strain-rate magnitude. This makes sure that C_μ^* remains bounded for all values of $\mathcal{P}/\varepsilon$, so that numerical stability and realizability are retained.

Model summary

The k-ε-f_P model is identical to the standard k-ε model, except that C_μ is replaced by C_μ^*:

$$\nu_T = C_\mu^* \frac{k^2}{\varepsilon}, \tag{2.34}$$

while the transport equations for k and ε remain unchanged (Equation 2.11, Equation 2.12). Since f_P is an explicit function of local flow variables, no additional transport equations or boundary conditions are required [14]. Physically, C_μ^* reduces the eddy viscosity in high-shear regions such as the wake edges, delaying wake recovery compared to the standard model.

Van der Laan et al. [14] validated the model against LES and field measurements for eight single wake cases and showed that it significantly improves velocity deficit predictions. Van der Laan et al. [51] further demonstrated good performance for double wake configurations. However, because the model retains the linear stress-strain relation, it does not improve the prediction of individual Reynolds stress components.

2.3.6 Extended k-ε Models with Actuator Disk Source Terms

The k-ε-f_P model improves wake predictions by modifying the eddy viscosity coefficient, but it does not account for the direct effect of the actuator disk forces on the turbulence itself. In the exact transport equations for k and ε, the body forces applied by the rotor introduce additional source and sink terms. In the standard k-ε model, these terms are neglected [24]. This section reviews two extended models that reintroduce these terms.

Actuator disk force

In the models discussed below, the wind turbine is represented as an actuator disk (AD) that exerts a body force on the flow. For the standard AD model without rotation, the turbine-induced force per unit volume is [7]:

$$f_i = -\frac{1}{2} C_T' A_{\text{cell}} \left(\bar{u}_{d,i}\right)^2 n_i \frac{\gamma_{j,l}}{V_{\text{cell}}}, \tag{2.35}$$

where $C_T' = C_T/(1-a)^2$ is the disk-based thrust coefficient with a the induction factor, A_{cell} is the frontal area of the computational cell within the rotor area, $\bar{u}_{d,i}$ is the disk-averaged velocity component, n_i is the unit vector perpendicular to the disk, $\gamma_{j,l}$ is the area overlap fraction, and V_{cell} is the cell volume.

Source term in the ε-equation: El Kasmi and Masson

El Kasmi and Masson [52] proposed the first extension, which adds a source term to the dissipation equation (originally due to Chen and Kim [53]):

$$S_\varepsilon = C_{\varepsilon 4} \frac{\varepsilon}{k} \mathcal{P}, \tag{2.36}$$

where $C_{\varepsilon 4}$ is a model constant and the term is only active in a prescribed cylindrical region around the rotor. El Kasmi and Masson showed improved velocity deficit predictions for single wake cases, using $C_\mu = 0.033$ [52] rather than $C_\mu = 0.09$. However, $C_{\varepsilon 4}$ and the activation region must be calibrated individually for each case and are not universal [46]. Prospathopoulos et al. [54] and Réthoré [36] confirmed that a calibration optimized for the far wake does not necessarily perform well in the near wake, and vice versa.

Sink term in the k-equation: Zehtabiyan-Rezaie and Abkar

Réthoré [36] used LES data to evaluate the actuator disk source terms in both the k- and ε-equations. The results (Figure 2.3) show that the sink term in the k-equation at its peak is two orders of magnitude larger than the local dissipation, while the corresponding ε-equation term is small enough to justify its omission. This suggests that modifying the ε-equation addresses the wrong equation.

Based on this analysis, Zehtabiyan-Rezaie and Abkar [7] derived a sink term S_k and added it to the modeled k-equation:

$$\partial_t k + \bar{u}_i \partial_i k = \partial_j \left[\left(\nu + \frac{\nu_T}{\sigma_k} \right) \partial_j k \right] + \mathcal{P} - \varepsilon + S_k, \tag{2.37}$$

where S_k is derived from the actuator disk force acting on the turbulent velocity fluctuations. For a yaw-aligned rotor:

$$S_k = -\frac{1}{2} C_T' A_{\text{cell}} \left(2\overline{u_{d,x}'^2}\, \bar{u}_{d,x} + \overline{u_{d,x}'^3} \right) \frac{\gamma_{j,l}}{V_{\text{cell}}}. \tag{2.38}$$

The negative sign confirms that this term acts as a sink. It represents the actuator disk extracting energy from the turbulent fluctuations in addition to extracting energy from the mean flow. Applying the isotropic turbulence assumption $\overline{u_{d,x}'^2} \approx \frac{2}{3} k_d$ yields:

$$S_k \approx -\frac{1}{2} C_T' A_{\text{cell}} \left[\frac{4}{3} k_d\, \bar{u}_{d,x} + \left(\frac{2}{3} k_d \right)^{3/2} \right] \frac{\gamma_{j,l}}{V_{\text{cell}}}, \tag{2.39}$$

where k_d is the disk-averaged turbulent kinetic energy. Unlike the El Kasmi and Masson model, this formulation requires no empirical constants beyond the AD's thrust coefficient C_T and introduces no arbitrary activation region, since the term is only active at the rotor plane through $\gamma_{j,l}$.

Zehtabiyan-Rezaie and Abkar [7] validated the model against LES for several wind farm configurations. The extended model reduces the normalized power prediction error from 36% to 12% for aligned arrays with $7D$ spacing and captures the double-peak turbulence intensity structure in the wake that the standard k-ε model fails to reproduce.

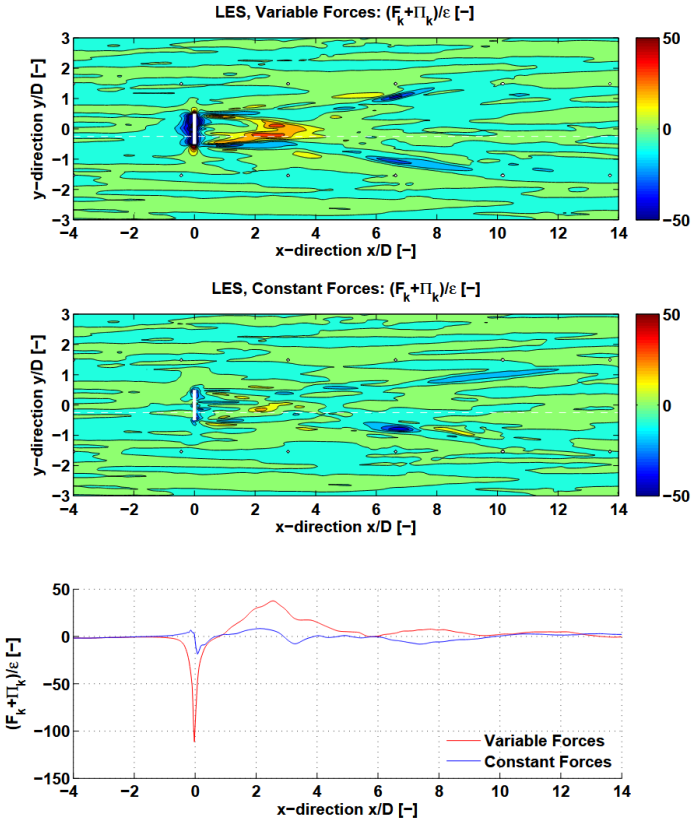

Figure 2.3: Force and pressure terms of the k-equation normalized with the local ε, from two LES simulations. The white dotted line indicates the path of the bottom plot [36].

2.3.7 3-Equation Models

Beyond two-equation closures, 3-equation models introduce an additional transport equation to capture aspects of turbulence anisotropy that the standard k-ε framework cannot represent. An example is the k-ε-$\overline{v^2}$ model of Durbin [55]. This model extends the k-ε system with a transport equation for $\overline{v^2}$, the wall-normal component of the Reynolds stress tensor. The eddy viscosity is then defined as $\nu_T = C_\mu \overline{v^2} T$, replacing the isotropic k-based scaling.

However, the $\overline{v^2}$-f model also requires the solution of an elliptic relaxation equation for f, which couples all spatial directions including the streamwise direction. This fundamentally conflicts with the marching solution procedure of the PNS framework (Section 2.1.4). Moreover, the additional transport equation for $\overline{v^2}$ provides information about normal stress anisotropy. But this is not required by the parabolic wake equation, as discussed in Section 2.3.4. For these reasons, 3-equation models are not pursued further in this work.

2.4 Shortcomings and Research Gap

In the previous sections, different methods of turbulence modeling have been reviewed, ranging from the full Reynolds stress transport equations down to algebraic closure models. Figure 2.4 summarises the relationships between these models and the most important assumptions that connect them. This section analyses the shortcomings of these models, after which the turbulence closures to be investigated will be selected, and the research questions are formulated.

2.4.1 Limitations of the Ainslie Eddy Viscosity Closure

The Ainslie eddy viscosity model (Section 2.2.2) is an algebraic model, since it determines the eddy viscosity through local characterics of the flow without the use of additional transport equations. Therefore, the model is not able to take into account the history of turbulence production and dissipation. The eddy viscosity at any point in the domain only depends on the local variables and not on any information upstream. This is a severe limitation of the model, since the production of k close to the turbine rotor is high, from which turbulent kinetic energy is transport downstream.

In the region close to the turbine, the equilibrium assumption that underlies the eddy viscosity is invalid, since production is much greater there than dissipation. The eddy viscosity model used by AWM tries to account for this by applying filter function F_1 and F_2 that suppress the eddy viscosity in this region [33], [34], [56]. However, these functions require

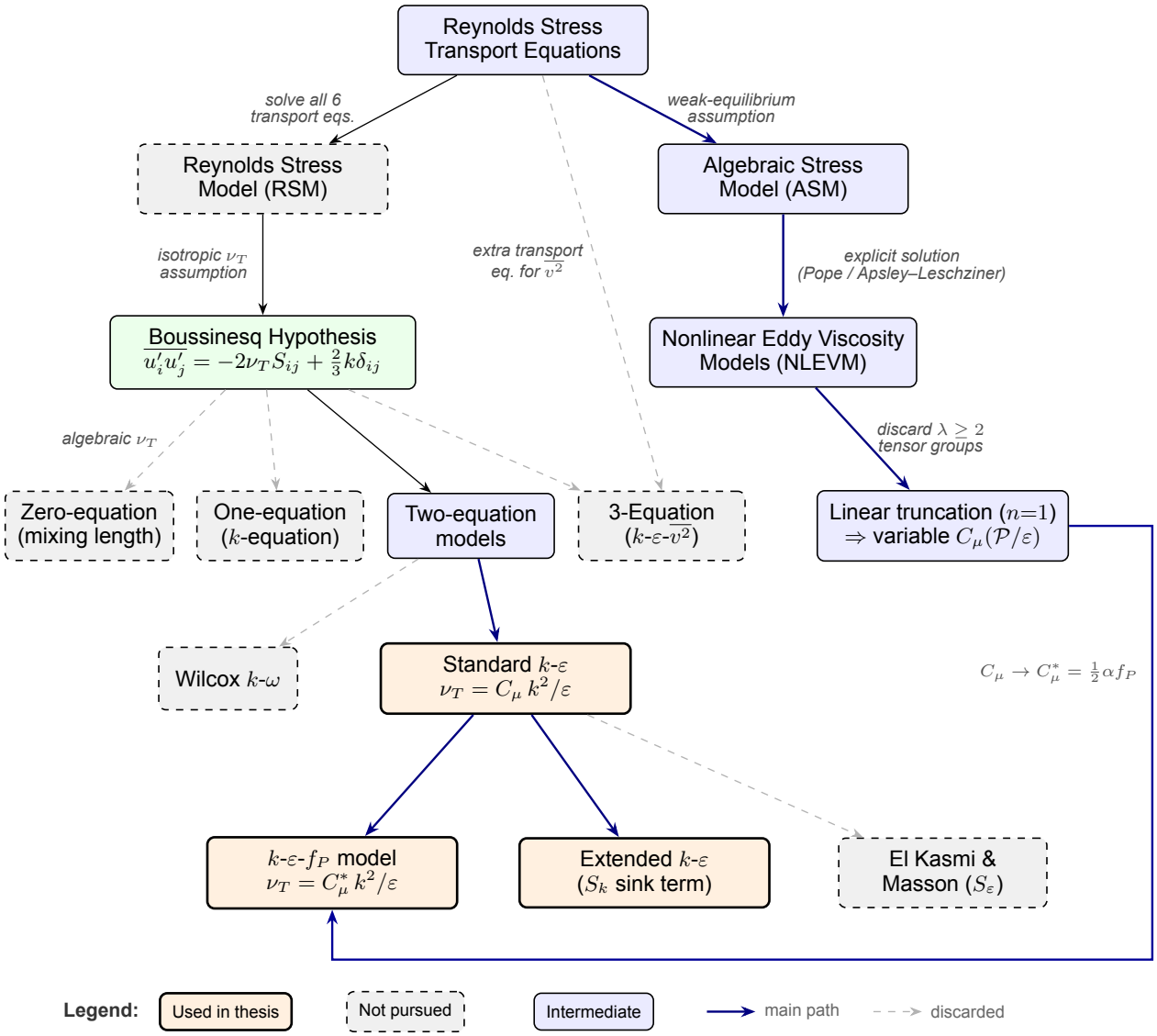

Figure 2.4: Overview of RANS turbulence closure models discussed. Orange boxes indicate the models used in the thesis. blue boxes show intermediate steps, while grey dashed boxes present models not pursued. The thick blue path traces the derivation chain from the Reynolds stress transport equations to the k-ε-f_P model.

tuning, since they contain empirical constants that are not derived from a physical mechanism. Varying thrust settings or atmospheric conditions would require a new calibration. Therefore it is desirable to develop a model that is based on physical mechanisms so it only requires minimal calibration.

Furthermore, the Ainslie Eddy Viscosity Closure is not compatible with the Forced Ainslie Wake Model. FAWM reintroduces the actuator disk pressure gradient as a forcing term in the axial momentum equation, which significantly improves momentum conservation. However, the Ainslie eddy viscosity model causes numerical instabilities when coupled with the FAWM. For this reason, the current FAWM implementation uses only a constant eddy viscosity [2]. While this ensures numerical stability, it removes any spatial variation of the eddy viscosity. This means the model is not able to represent a difference between the enhanced diffusion at the wake edges and the reduced mixing in the wake core.

With the forcing term added to the baseline AWM, a part of the pressure-related shortcomings has been resolved. Now a logical next step would be to replace the current eddy viscosity closure with a more accurate alternative that is better able to represent the flow phenomena inside a turbine's wake, while staying compatible with the parabolic marching scheme.

2.4.2 Limitations of the Standard k-ε Model in Wake Flows

The standard k-ε model (Equation 2.10) is one of the most popular turbulence model in wind energy modeling. It calculates the turbulent kinetic energy k and its dissipation rate ε through their modeled transport equations, which provides a physics-based mechanism for the evolution of turbulent mixing over the domain. However, the model was originally calibrated for boundary layer and channel flows [26], and it's not well suited for the strong non-equilibrium conditions that occur in wind turbine wakes. Especially the constant C_μ in the definition of the eddy viscosity limits the model's ability to correctly predict turbulent mixing.

The constant C_μ causes the eddy viscosity $\nu_T = C_\mu k^2/\varepsilon$ to be overpredicted in the wake shear layer, where the ratio $\mathcal{P}/\varepsilon$ is significantly larger than the equilibrium value of unity for which C_μ was calibrated. The overpredicted eddy viscosity causes the wake to recover to freestream velocity too quickly. This leads to an underprediction of the velocity deficit in the far wake [14], [52], [54].

Another limitation of the standard k-ε model is the Boussinesq hypothesis itself (Section 2.3.1). The hypothesis relies on the assumption of an isotropic relationship between the Reynolds stresses and the mean strain-rate. However, Wind turbine wakes are characterised by strongly anisotropic turbulence, since the rotor mainly generates streamwise fluctuations, so that $\overline{u'^2} \gg \overline{v'^2}, \overline{w'^2}$ in the near wake. This anisotropy cannot be captured by the Boussinesq hypothesis. This causes an inaccuracy in the model that cannot be reduced through any calibration [13].

2.4.3 Extended k-ε Approaches

Researchers have proposed different modifications to the standard k-ε model to mitigate these shortcomings. While each addresses a specific limitation of the model, they have not yet been applied within a parabolic RANS solver.

The k-ε-f_P model of Laan et al. [14] makes C_μ flow-dependent through the parameter f_P (Section 2.3.5). This model has a strong basis in the NLEVM (see Equation 2.31) and has been validated against LES and field measurements for single and double wake configurations, where it showed better agreements with the reference data of the velocity deficit predictions [46]. However, the model has only been coupled with an elliptic three-dimensional solver, and not yet with a parabolized solver.

The S_k sink term derived by Zehtabiyan-Rezaie and Abkar [7] accounts for the effect of the actuator disk force on the turbulent kinetic energy. It depends only on local flow variables at the rotor plane and is therefore compatible with a parabolic marching scheme (see Section 2.3.6). However, this model has also been developed and validated only in elliptic RANS, and its behaviour inside a parabolic framework has not been studied.

2.4.4 Research Questions

The shortcomings identified above point to a clear research gap. FAWM has resolved the main shortcoming of the original Ainslie model by reintroducing the actuator disk pressure gradient. However, its turbulence closure is currently limited to a constant eddy viscosity, which cannot represent the spatial variation of turbulent mixing in the wake. The standard k-ε model would provide a transport-based alternative, but its fixed C_μ overpredicts turbulent diffusion in the wake shear layer. Extended closures that address this overprediction exist and have been validated in elliptic RANS solvers, but none has been tested within the parabolic FAWM framework.

Based on the model hierarchy reviewed above and summarised in Figure 2.4, three turbulence closures are selected for implementation in FAWM. The first is the standard k-ε model (Equation 2.10), which serves as a baseline two-equation closure against which the extended models can be compared. The second is the k-ε-f_P model (Section 2.3.5), which replaces the fixed C_μ with a flow-dependent $C_\mu^* = \frac{1}{2}\alpha f_P$ derived from the NLEVM. The third is the extended k-ε model with the S_k sink term (Equation 2.39), which accounts for the direct effect of the actuator disk force on turbulent kinetic energy. This term does not require calibration, making it a good alternative to the k-ε-f_P closure.

The research questions of this thesis are:

1. Can the standard k-ε, k-ε-f_P, and extended k-ε (with S_k sink term) closures be successfully integrated into the FAWM parabolic solver, and do the extended models improve velocity deficit and turbulence predictions compared to the standard k-ε?
2. How do the FAWM predictions with these turbulence closures compare against high-fidelity large eddy simulation reference data?

3 Development of the Parabolized k–ε Model

In this chapter the implementation of the parabolized, axisymmetric k–ε turbulence model is described. The parabolized and axisymmetric transport equations for k and ε are discretized using the finite volume method with a second-order upwind scheme for the convective terms and central differencing for the diffusive terms. Because the equations are parabolized, the axial diffusion is omitted and the solution is advanced downstream using a marching scheme in the axial direction.

The chapter contains the following four sections. Firstly, Section 3.1 describes the computational mesh, the conventions used, and the boundary conditions. Secondly, Section 3.2 shows the finite volume discretization of the k and ε transport equations. Thirdly, Section 3.3 presents the final system of equations and the fixed-point iteration used to solve the nonlinear equations. Lastly, Section 3.4 describes the coupling of the turbulence model with the Forced Ainslie Wake Model.

3.1 Computational Setup

This section explains the structure of the axisymmetric mesh, the index conventions used for the variables, and the boundary conditions applied at the domain boundaries. The domain is discretized with the finite volume method, in which the governing equations are integrated over each control volume. This formulation is conservative by construction, since the flux leaving one cell through a shared face is identical to the flux entering the neighbouring cell, so that mass and momentum are preserved.

3.1.1 Mesh and Variable Arrangement

The computational domain is discretized using a two-dimensional axisymmetric mesh in the (x, r) plane. The mesh consists of rectangular cell whose edges are aligned in the x and r directions. The axial coordinate x serves as the marching direction, and the radial coordinate r extends from the symmetry axis at $r = 0$ to the outer boundary at $r = r_{\text{max}}$.

The flow variables are organized in a staggered manner. The axial velocity U is defined in the middle of the vertical (constant-x) faces, and the radial velocity V is defined in the middle of the horizontal (constant-r) faces. Both velocity components are assumed to be uniform over their respective faces. Storing the velocities in a staggered way at these locations avoids the need to interpolate face-normal velocity components when discretizing the convective terms, which simplifies the implementation and preserves the accuracy of the convective flux calculation. The turbulent kinetic energy k, the dissipation rate ε, and the eddy viscosity ν_T are stored at the cell centres and are assumed to be uniform over each cell.

A schematic of the mesh and the variable placement is shown in Figure 3.1.

3.1.2 Boundary Conditions

At the symmetry axis, where $r = 0$, the radial velocity is zero and the gradients in radial direction of all scalars are also zero, i.e. $V = 0$ and $\partial\phi/\partial r = 0$ for $\phi \in \{k, \varepsilon\}$. These conditions follow directly from the symmetry of the flow field.

At the outer radial boundary, where $r = r_{\text{max}}$, Neumann conditions are applied to all transported scalars, $\partial\phi/\partial r = 0$. This assumes that the wake has recovered sufficiently for the radial gradients to be negligible at the edge of the domain. The outer boundary must therefore be placed far enough from the wake centre for this assumption to hold; in practice, a domain radius of several rotor diameters is used.

In the axial direction, initial conditions for U, k, and ε are prescribed at the inflow plane $x = x_{\text{min}}$. From this plane, the solution is marched downstream. No outlet boundary condition is required, since the parabolized formulation means there is no information traveling upstream.

3.1.3 Parabolized Formulation

The turbulence transport equations are simplified by omitting the axial diffusion terms, which yields a parabolized system that can be solved by marching through the solution. This assumption is accurate when gradients in axial direction are

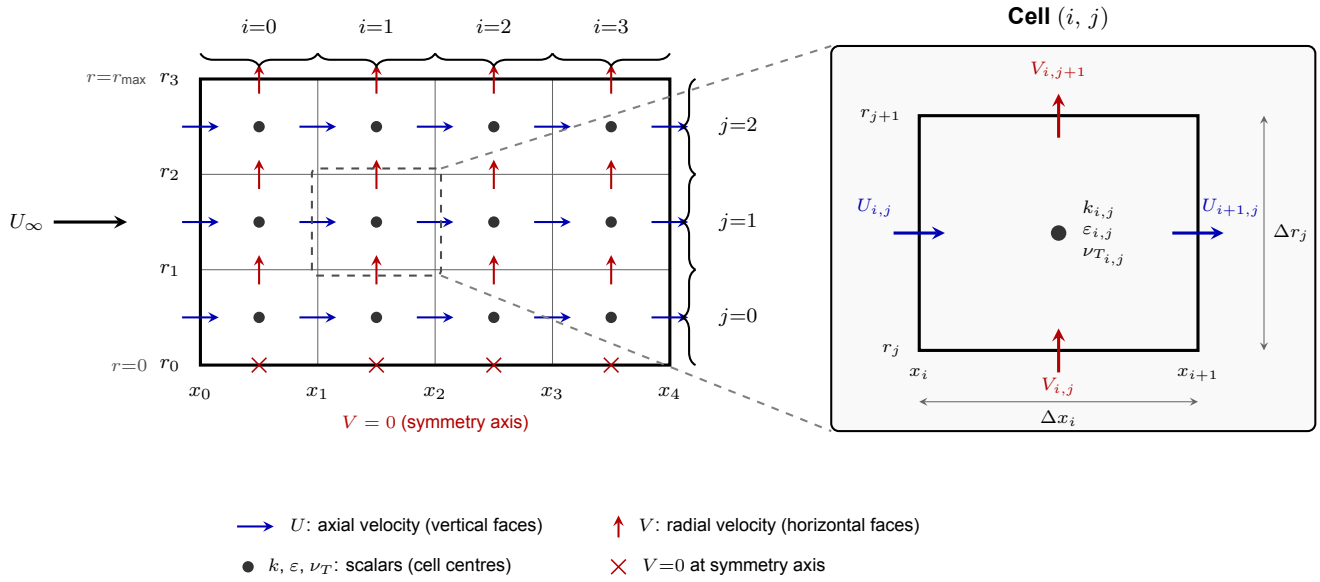

Figure 3.1: Staggered mesh in the axisymmetric plane with variable placement. The axial velocity U is stored at the vertical faces (blue arrows), the radial velocity V at the horizontal faces (red arrows), and scalars at the cell centres (dots). Crosses at r_1 indicate $V = 0$ due to the symmetry condition. The inset shows a single cell (i, j) with all variable locations and cell dimensions.

small compared to gradients in radial direction. In the case of a wind turbine, this is true in the far wake where the flow expands gradually in the streamwise direction.

A requirement in order to be able to march through the solution is the absence of flow reversal, which means all information must travel exclusively downstream. In wind turbine wakes, reverse flow generally does not occur, making the parabolized formulation viable. The resulting reduction in computational cost is enormous, as the solution at each axial step depends only on upstream information and the system can be solved column by column instead of solving for the entire mesh domain at once.

3.2 Finite Volume Discretization of the Turbulence Transport Equations

This section presents the finite volume discretization of the parabolized k–ε turbulence model. Because the solver marches through the solution in the axial direction, axial diffusion is neglected and only radial diffusion is kept. All flow variables are functions of the axial coordinate x and the radial coordinate r.

The transport equations for the turbulent kinetic energy k and its dissipation rate ε are are as follows:

$$\nabla\cdot\left(\begin{pmatrix}U\\V\end{pmatrix}k\right) = \nabla\cdot\left(\frac{\nu_T}{\sigma_k}\begin{pmatrix}0\\\dfrac{\partial k}{\partial r}\end{pmatrix}\right) + P_k - \varepsilon + S_k, \tag{3.1a}$$

$$\nabla\cdot\left(\begin{pmatrix}U\\V\end{pmatrix}\varepsilon\right) = \nabla\cdot\left(\frac{\nu_T}{\sigma_\varepsilon}\begin{pmatrix}0\\\dfrac{\partial \varepsilon}{\partial r}\end{pmatrix}\right) + C_{\varepsilon 1}\frac{\varepsilon}{k}P_k - C_{\varepsilon 2}\frac{\varepsilon^2}{k}, \tag{3.1b}$$

$$P_k = 2\nu_T\, S_{ij}\, S_{ij}, \tag{3.1c}$$

$$\nu_T = C_\mu \frac{k^2}{\varepsilon}, \tag{3.1d}$$

where $S_{ij} = \frac{1}{2}\left(\frac{\partial U_i}{\partial x_j} + \frac{\partial U_j}{\partial x_i}\right)$ is the mean strain-rate tensor. In Equation 3.1a and Equation 3.1b, the left-hand sides represent advection. The right-hand side contains, from left to right: the radial diffusion term, the production term, and the dissipation term. The additional source term S_k in the k-equation represents the turbine-induced sink.

The two transport equations have a similar structure. Their only differences are in their coefficients and source terms. To stay concise, the discretization is derived for the k-equation.

3.2.1 Convective Terms

The convective term in the k-equation is discretized by integrating $\nabla\cdot(\mathbf{u}\,k)$ over the control volume $\Omega_{i,j}$ and applying the divergence theorem:

$$\begin{aligned}\iiint_{\Omega_{i,j}} \nabla\cdot\begin{pmatrix}U\\V\end{pmatrix} k\; d\Omega &= \iint_{\partial\Omega_{i,j}} \begin{pmatrix}U\\V\end{pmatrix} k\cdot\mathbf{n}\; dA \\ &= 2\pi\int_{r_j}^{r_{j+1}} \big(Uk\big|_{x_{i+1}} - Uk\big|_{x_i}\big)\, r\; dr + 2\pi\int_{x_i}^{x_{i+1}} \big(Vrk\big|_{r_{j+1}} - Vrk\big|_{r_j}\big)\, dx \\ &= \underbrace{\pi(r_{j+1}^2 - r_j^2)\big(Uk\big|_{x_{i+1}} - Uk\big|_{x_i}\big)}_{\text{axial flux}} + \underbrace{2\pi\,\Delta x_i\big(Vrk\big|_{r_{j+1}} - Vrk\big|_{r_j}\big)}_{\text{radial flux}},\end{aligned} \tag{3.2}$$

where the surface integrals have been approximated by determining the flux at the face centres and assuming that it is uniform over the entire face. The axial and radial flux contributions are treated separately.

Axial Convective Flux

The first term in Equation 3.2 represents convective transport across the vertical (constant-x) faces of the control volume. Because the axial velocity U is stored at these faces, no interpolation is required for U itself. However, the quantity k is stored at the cell centres and must be interpolated to the faces.

A second-order upwind scheme is used for this interpolation. This scheme was chosen for its numerical stability, accuracy, simplicity, and because it has less numerical diffusion than the first-order upwind scheme [57]. Because the flow is always directed in the positive x-direction, the upwind scheme always use the two upstream cell centres of a certain face.

A linear profile is constructed through the two upstream cell centres,

$$k(x, r_{j+1/2}) = a + b\,x,$$

and evaluated at the face location. For the right face located at $x = x_{i+1}$ this yields

$$k\big|_{x_{i+1}} = k_{i,j} + \frac{\Delta x_i}{\Delta x_i + \Delta x_{i-1}}\big(k_{i,j} - k_{i-1,j}\big) = \frac{2\Delta x_i + \Delta x_{i-1}}{\Delta x_i + \Delta x_{i-1}}\,k_{i,j} - \frac{\Delta x_i}{\Delta x_i + \Delta x_{i-1}}\,k_{i-1,j}. \tag{3.3}$$

Applying the same procedure at the left face $x = x_i$ gives

$$k\big|_{x_i} = \frac{2\Delta x_{i-1} + \Delta x_{i-2}}{\Delta x_{i-1} + \Delta x_{i-2}}\,k_{i-1,j} - \frac{\Delta x_{i-1}}{\Delta x_{i-1} + \Delta x_{i-2}}\,k_{i-2,j}. \tag{3.4}$$

Substituting Equation 3.3 and Equation 3.4 into the axial term of Equation 3.2 gives

$$\pi(r_{j+1}^2 - r_j^2)\big(Uk\big|_{x_{i+1}} - Uk\big|_{x_i}\big) = \pi(r_{j+1}^2 - r_j^2)\Big(a_i^1\,U_{i+1,j}\,k_{i,j} - \big(a_i^2\,U_{i+1,j} + a_i^3\,U_{i,j}\big)\,k_{i-1,j} + a_i^4\,U_{i,j}\,k_{i-2,j}\Big), \tag{3.5}$$

where

$$a_i^1 = \frac{2\Delta x_i + \Delta x_{i-1}}{\Delta x_i + \Delta x_{i-1}},\quad a_i^2 = \frac{\Delta x_i}{\Delta x_i + \Delta x_{i-1}},\quad a_i^3 = \frac{2\Delta x_{i-1} + \Delta x_{i-2}}{\Delta x_{i-1} + \Delta x_{i-2}},\quad a_i^4 = \frac{\Delta x_{i-1}}{\Delta x_{i-1} + \Delta x_{i-2}}. \tag{3.6}$$

Equation 3.7 shows the axial fluxes in matrix–vector form for all radial cells j in axial column i.

$$\vec{F}_i^{\,x} = \mathbf{A}\Big(a_i^1\,\vec{U}_{i+1}\odot\vec{k}_i - \big(a_i^2\,\vec{U}_{i+1} + a_i^3\,\vec{U}_i\big)\odot\vec{k}_{i-1} + a_i^4\,\vec{U}_i\odot\vec{k}_{i-2}\Big), \tag{3.7}$$

where $\odot$ denotes the Hadamard product. The matrix $\mathbf{A}$ and the column vectors $\vec{U}_i$ and $\vec{k}_i$ are defined as

$$\mathbf{A} = \pi\begin{bmatrix} r_1^2 & & & \\ & r_2^2 - r_1^2 & & \\ & & \ddots & \\ & & & r_{J+1}^2 - r_J^2 \end{bmatrix},\quad \vec{U}_i = \begin{pmatrix} U_{i,0}\\ U_{i,1}\\ \vdots\\ U_{i,J}\end{pmatrix},\quad \vec{k}_i = \begin{pmatrix} k_{i,0}\\ k_{i,1}\\ \vdots\\ k_{i,J}\end{pmatrix}. \tag{3.8}$$

Note that the first diagonal entry of $\mathbf{A}$ reduces to πr_1^2 because $r_0 = 0$ at the axis of symmetry.

Radial Convective Flux

The second term in Equation 3.2 represents the convective flux in radial direction across the horizontal (constant-r) faces of the control volume. The quantity Vr is stored at these faces, whereas k is stored at the cell centres and must be interpolated to the horizontal faces. As in the axial direction, a second-order upwind interpolation is used. However, because the radial velocity can be directed either inward or outward, the upwind direction depends on the sign of Vr.

Two selector functions are introduced to determine the upwind direction:

$$\alpha_{i,j} = \begin{cases} 1, & Vr_{i,j} > 0, \\ 0, & \text{otherwise}, \end{cases} \qquad \beta_{i,j} = \begin{cases} 1, & Vr_{i,j} < 0, \\ 0, & \text{otherwise}. \end{cases} \tag{3.9}$$

Here $\alpha_{i,j} = 1$ selects the outward-flow stencil and $\beta_{i,j} = 1$ selects the inward-flow stencil. When $Vr_{i,j} = 0$, both selectors are zero and the radial flux at that face is also zero.

A linear profile $k(r) = a + b\,r$ is interpolated through two upstream cell centres,which results in the following second-order upwind coefficients for interior radial faces, where $2 \le j \le J-1$:

$$b_j^1 = \frac{\Delta r_{j-1}}{\Delta r_{j-1} + \Delta r_{j-2}}, \quad b_j^2 = \frac{2\Delta r_{j-1} + \Delta r_{j-2}}{\Delta r_{j-1} + \Delta r_{j-2}}, \quad b_j^3 = \frac{2\Delta r_j + \Delta r_{j+1}}{\Delta r_j + \Delta r_{j+1}}, \quad b_j^4 = \frac{\Delta r_j}{\Delta r_j + \Delta r_{j+1}}. \tag{3.10}$$

At the boundaries of the domain, the second-order upwind scheme cannot be applied because some of the points will fall outside the domain. The coefficients for the faces at the boundaries are derived from the boundary conditions, as described below.

The lower horizontal face of the first cell, where $j = 1$ is also the axis of symmetry, at which location the radial velocity is zero. Therefore, there is no flux across this boundary, and the interpolation coefficients are all set to zero:

$$b_0^1 = b_0^2 = b_0^3 = b_0^4 = 0.$$

At the face $r = r_1$, the outward stencil requires a value of k at a location below the axis of symmetry, which does not exist in the domain. Therefore, the outward stencil is reduced to a first-order upwind scheme, while the inward stencil keeps the standard second-order stencil:

$$b_1^1 = 0, \qquad b_1^2 = 1, \qquad b_1^3 = \frac{2\Delta r_1 + \Delta r_2}{\Delta r_1 + \Delta r_2}, \qquad b_1^4 = \frac{\Delta r_1}{\Delta r_1 + \Delta r_2}.$$

A Neumann condition $\partial k/\partial r = 0$ is enforced at the outer boundary where $j = J+1$. A ghost cell of the same size as the boundary cell is place outside the domain, and the value of k at its centre is set equal to the value of k at center of the boundary cell: $k_{i,J+1} = k_{i,J}$. In the case of inward directed flow here, the second-order scheme is not used. Instead a first-order upwind scheme is used, making sure that only one ghost cell is needed. The resulting coefficients are

$$b_{J+1}^1 = \frac{\Delta r_J}{\Delta r_J + \Delta r_{J-1}}, \qquad b_{J+1}^2 = \frac{2\Delta r_J + \Delta r_{J-1}}{\Delta r_J + \Delta r_{J-1}}, \qquad b_{J+1}^3 = 1, \qquad b_{J+1}^4 = 0.$$

This yields the following result for k at the horizontal faces.

$$k\big|_{r_j} = \alpha_{i,j}\big(-b_j^1\, k_{i,j-2} + b_j^2\, k_{i,j-1}\big) + \beta_{i,j}\big(\; b_j^3\, k_{i,j} \quad - b_j^4\, k_{i,j+1}\big). \tag{3.11}$$

The fluxes of the radial convection are determined from the cell centred k values using the following equation

$$\vec{Vr} k_{i,\text{faces}} = \mathbf{B}^* \, \vec{k}_i, \tag{3.12}$$

where $\mathbf{B}^*$ includes the radial velocity, the interpolation coefficients, and the coefficients b. It is given by

$$\mathbf{B}^* = \text{diag}(\vec{Vr}_i) \begin{bmatrix} 0 & & & \cdots & & & 0 \\ \alpha_1 b_1^2 & \beta_1 b_1^3 & -\beta_1 b_1^4 & & & & \\ -\alpha_2 b_2^1 & \alpha_2 b_2^2 & \beta_2 b_2^3 & -\beta_2 b_2^4 & & & \\ & \ddots & \ddots & \ddots & \ddots & & \\ & & -\alpha_{J-1} b_{J-1}^1 & \alpha_{J-1} b_{J-1}^2 & \beta_{J-1} b_{J-1}^3 & -\beta_{J-1} b_{J-1}^4 & \\ & & & -\alpha_J b_J^1 & \alpha_J b_J^2 & \beta_J (b_J^3 - b_J^4) & \\ & & & & -\alpha_{J+1} b_{J+1}^1 & \alpha_{J+1} b_{J+1}^2 + \beta_{J+1} b_{J+1}^3 & \end{bmatrix}, \tag{3.13}$$

The Neumann boundary condition is included in the last two rows. The coefficients thar are multiplied with the ghost-cell value $k_{i,J+1}$ are added to the coefficient of $k_{i,J}$, because $k_{i,J+1} = k_{i,J}$.

The vectors that include al the coefficients b are defined as

$$\vec{b}^1 = \begin{pmatrix} 0 \\ 0 \\ b_2^1 \\ \vdots \\ b_{J-1}^1 \\ b_J^1 \\ b_{J+1}^1 \end{pmatrix}, \quad \vec{b}^2 = \begin{pmatrix} 0 \\ 1 \\ b_2^2 \\ \vdots \\ b_{J-1}^2 \\ b_J^2 \\ b_{J+1}^2 \end{pmatrix}, \quad \vec{b}^3 = \begin{pmatrix} 0 \\ b_1^3 \\ b_2^3 \\ \vdots \\ b_{J-1}^3 \\ b_J^3 \\ 1 \end{pmatrix}, \quad \vec{b}^4 = \begin{pmatrix} 0 \\ b_1^4 \\ b_2^4 \\ \vdots \\ b_{J-1}^4 \\ b_J^4 \\ 0 \end{pmatrix}. \tag{3.14}$$

For each cell, the flux over the lower face is subtracted from the flux over the upper flux, which yields the following result.

$$\vec{F}_i^{\,r} = 2\pi\,\Delta x_i \big(\vec{Vr}k_{i,\text{faces, }2:(J+1)} - \vec{Vr}k_{i,\text{faces, }1:J}\big) = \mathbf{B}\,\vec{k}_i, \tag{3.15}$$

where **B** is defined as

$$\mathbf{B} = 2\pi\,\Delta x_i \big(\mathbf{B}^*_{2:(J+1),:} - \mathbf{B}^*_{1:J,:}\big). \tag{3.16}$$

Combined Convective Fluxes

In Equation 3.17, the axial (Equation 3.7) and radial (Equation 3.15) convective fluxes are combined, so that the resulting vector for column i becomes

$$\vec{F}_i^{\,c} = \mathbf{A}\Big(a_i^1\,\vec{U}_{i+1} \odot \vec{k}_i - \big(a_i^2\,\vec{U}_{i+1} + a_i^3\,\vec{U}_i\big) \odot \vec{k}_{i-1} + a_i^4\,\vec{U}_i \odot \vec{k}_{i-2}\Big) + \mathbf{B}\,\vec{k}_i. \tag{3.17}$$

The exact same procedure is done for ε equation, but with all instances of k replaced with ε.

3.2.2 Diffusive Terms

In Equation 3.1a, the first term on the right hand side of the equations shows the diffusion in radial direction caused by the turbulence in the flow. The axial diffusion is absent because of the parabolization assumption.

$$\nabla\cdot\left(\frac{\nu_T}{\sigma_k}\begin{pmatrix} 0 \\ \dfrac{\partial k}{\partial r}\end{pmatrix}\right). \tag{3.18}$$

The diffusive term is integrated over a cell volume $\Omega_{i,j}$, after which the divergence theorem is applied, yielding

$$\begin{aligned}\iiint_{\Omega_{i,j}} \nabla\cdot\left(\frac{\nu_T}{\sigma_k}\begin{pmatrix} 0 \\ \dfrac{\partial k}{\partial r}\end{pmatrix}\right) d\Omega &= \iint_{\partial\Omega_{i,j}} \frac{\nu_T}{\sigma_k}\begin{pmatrix} 0 \\ \dfrac{\partial k}{\partial r}\end{pmatrix}\cdot\mathbf{n}\,dA \\ &= \frac{2\pi}{\sigma_k}\int_{x_i}^{x_{i+1}} \left(\nu_T\frac{\partial k}{\partial r}\,r\Big|_{r_{j+1}} - \nu_T\frac{\partial k}{\partial r}\,r\Big|_{r_j}\right) dx \\ &= \frac{2\pi\,\Delta x_i}{\sigma_k}\left(\nu_T\frac{\partial k}{\partial r}\,r\Big|_{r_{j+1}} - \nu_T\frac{\partial k}{\partial r}\,r\Big|_{r_j}\right).\end{aligned} \tag{3.19}$$

In this equation, the integrals have been approximated by evaluating them at the centre of the faces and assuming they are constant over each face. The resulting diffusive flux is a function of the eddy viscosity ν_T and the radial gradient $\frac{\partial k}{\partial r}$ evaluated at the cell faces. The eddy viscosity ν_T is known only at the cell centers, so a linear interpolation between two adjacent cell centers is done to determine the value at a face. $\frac{\partial k}{\partial r}$ is discretized at each face using central differencing.

Eddy Viscosity Interpolation

At face $r = r_j$, the eddy viscosity is calculated through linear interpolation between the values of the two adjacent cells, which yields:

$$\nu_T\big|_{r_j} = \frac{\Delta r_j}{\Delta r_{j-1} + \Delta r_j}\,\nu_{T_{i,j-1}} + \frac{\Delta r_{j-1}}{\Delta r_{j-1} + \Delta r_j}\,\nu_{T_{i,j}}. \tag{3.20}$$

A matrix $\mathbf{C}_\nu$ is defined that maps the cell-centerd ν_T to ν_T at the faces.

$$\vec{\nu}_{T_{i,\text{faces}}} = \mathbf{C}_\nu \, \vec{\nu}_{T_i}, \tag{3.21}$$

This matrix is defined as

$$\mathbf{C}_\nu = \begin{bmatrix} 0 & 0 & \cdots & 0 \\ \dfrac{\Delta r_1}{\Delta r_0 + \Delta r_1} & \dfrac{\Delta r_0}{\Delta r_0 + \Delta r_1} & & \\ & \ddots & \ddots & \\ & & \dfrac{\Delta r_J}{\Delta r_{J-1} + \Delta r_J} & \dfrac{\Delta r_{J-1}}{\Delta r_{J-1} + \Delta r_J} \\ 0 & \cdots & 0 & 0 \end{bmatrix}, \qquad \vec{\nu}_{T_i} = \begin{pmatrix} \nu_{T_{i,0}} \\ \nu_{T_{i,1}} \\ \vdots \\ \nu_{T_{i,J}} \end{pmatrix}. \tag{3.22}$$

The first and last rows of this matrix are zero. There is no flux over the axis of symmetry since the face area at $r = r_0$ is zero, so the diffusive flux over this face is always set to zero. At the boundary $r = r_{J+1}$, the Neumann boundary conditions implies there is no diffusive flux over this face, so the last row is also set to zero to enforce this.

Gradient Discretization

The radial gradient of k at a horizontal cell face $r = r_j$ is discretized using a second-order central difference scheme, resulting in

$$\left.\frac{\partial k}{\partial r}\right|_{r_j} = \frac{k_{i,j} - k_{i,j-1}}{\frac{1}{2}(\Delta r_{j-1} + \Delta r_j)}. \tag{3.23}$$

The gradients are saved in a vector, by using

$$\left(\frac{\partial \vec{k}}{\partial r}\right)_{i,\text{faces}} = \mathbf{D}^* \, \vec{k}_i, \tag{3.24}$$

where the matrix $\mathbf{D}^*$ is

$$\mathbf{D}^* = \begin{bmatrix} 0 & 0 & \cdots & 0 \\ \dfrac{-2}{\Delta r_0 + \Delta r_1} & \dfrac{2}{\Delta r_0 + \Delta r_1} & & \\ & \ddots & \ddots & \\ & & \dfrac{-2}{\Delta r_{J-1} + \Delta r_J} & \dfrac{2}{\Delta r_{J-1} + \Delta r_J} \\ 0 & \cdots & 0 & 0 \end{bmatrix}. \tag{3.25}$$

The first and last rows are again zero for the same reasons as for $\mathbf{C}_v$.

Diffusive Flux Operator

The resulting diffusive flux at each horizontal face is calculated by multiplying the interpolated eddy viscosity with the gradient at that face and the radial value r_j. In on equation that results in

$$\left(\nu_T \frac{\partial k}{\partial r}\, r\right)_{i,\text{faces}} = \mathbf{D}^{**} \, \vec{k}_i, \qquad \mathbf{D}^{**} = \text{diag}\big(\vec{\nu}_{T_{i,\text{faces}}} \odot \vec{r}_{\text{faces}}\big)\, \mathbf{D}^*, \tag{3.26}$$

where $\vec{r}_{\text{faces}} = (r_0, r_1, \ldots, r_{J+1})^\mathsf{T}$ which contains the radial coordinates of the horizontal faces, and $\vec{\nu}_{T_{i,\text{faces}}}$ is calculated with $\mathbf{C}_\nu$ using Equation 3.21.

The total diffusive flux of a control volume $\Omega_{i,j}$ is calculated by taking the difference by the flux over the upper and lower horizontal faces. For any axial column i this gives

$$\vec{F}_i^{\,d} = \frac{1}{\sigma_k}\, \mathbf{D}\, \vec{k}_i, \qquad \mathbf{D} = 2\pi\, \Delta x_i \big(\mathbf{D}^{**}_{2:(J+1),:} - \mathbf{D}^{**}_{1:J,:}\big). \tag{3.27}$$

The same steps are taken for ε, replacing k with ε and σ_k with σ_ε.

3.2.3 Production Terms

The second term on the right-hand side of Equation 3.1a serves as the productive term of k, caused by the transfer of kinetic energy from the mean flow to the turbulent fluctuations through the interaction between the Reynolds stresses and the mean strain-rate field. In the $k-\varepsilon$ model, this term is defined as

$$P_k = 2\,\nu_T\,S_{ij}\,S_{ij}, \tag{3.28}$$

where $S_{ij} = \frac{1}{2}\left(\partial U_i/\partial x_j + \partial U_j/\partial x_i\right)$ is the mean strain-rate tensor. The tensor S_{ij} is as follows (using axisymmetric coordinates) [19]

$$S_{ij} = \begin{bmatrix} \dfrac{\partial U}{\partial x} & \dfrac{1}{2}\left(\dfrac{\partial U}{\partial r} + \dfrac{\partial V}{\partial x}\right) & 0 \\ \dfrac{1}{2}\left(\dfrac{\partial U}{\partial r} + \dfrac{\partial V}{\partial x}\right) & \dfrac{\partial V}{\partial r} & 0 \\ 0 & 0 & \dfrac{V}{r} \end{bmatrix}. \tag{3.29}$$

After the double contraction of $S_{ij}\,S_{ij}$ is performed, the result includes five contributing terms to the total production. For a certain cell volume the production term yield

$$P_{k_{i,j}} = 2\,\nu_{T_{i,j}}\left[\left(\frac{\partial U}{\partial x}\right)^2_{i,j} + \left(\frac{\partial V}{\partial r}\right)^2_{i,j} + \frac{1}{2}\left(\frac{\partial U}{\partial r} + \frac{\partial V}{\partial x}\right)^2_{i,j} + \left(\frac{V}{r}\right)^2_{i,j}\right]. \tag{3.30}$$

The five contributions are calculated at the cell centers as follows.

Velocity Gradient Discretization

Axial gradient of U.

Since the axial velocity U is defined at the vertical cell faces, the axial gradient at a cell centre is easily determined by using a finite difference between the two values:

$$\left(\frac{\partial U}{\partial x}\right)_{i,j} = \frac{U_{i+1,j} - U_{i,j}}{\Delta x_i}. \tag{3.31}$$

Radial gradient of V.

A similar procedure is applied for the radial gradient of V.

$$\left(\frac{\partial V}{\partial r}\right)_{i,j} = \frac{V_{i,j+1} - V_{i,j}}{r_{j+1} - r_j}. \tag{3.32}$$

Radial gradient of U.

To calculate the radial gradient of U at a cell centre, the average values of U of two adjacent cells are used. Central differencing is then applied to calculate gradient. However, this is only possible for the interior cells which have an adjacent cell at each of upper and lower boundaries.

$$\left(\frac{\partial U}{\partial r}\right)_{i,j} = \frac{(U_{i,j+1} + U_{i+1,j+1}) - (U_{i,j-1} + U_{i+1,j-1})}{r_{j+2} + r_{j+1} - r_j - r_{j-1}}, \tag{3.33}$$

The denumerator represents the distance between the centers of the two adjacent cells $j+1$ and $j-1$. The numerator represents the difference between the average U of these two adjacent cells.

To determine $\frac{\partial U}{\partial r}$ at the centers of the boundary cells, ghost cells are again introduced at the boundaries outside the domain. These ghost cells have the same cell and values of U at their vertical faces as the boundary cells, to enforce the Neumann and symmetry boundary conditions ($\frac{\partial U}{\partial r} = 0$). This results in the following

$$\left(\frac{\partial U}{\partial r}\right)_{i,j} = \begin{cases} \dfrac{(U_{i,1} + U_{i+1,1}) - (U_{i,0} + U_{i+1,0})}{r_2 + 2\,r_1}, & j = 0, \\ \dfrac{(U_{i,J} + U_{i+1,J}) - (U_{i,J-1} + U_{i+1,J-1})}{r_{J+2} + r_{J+1} - r_J - r_{J-1}}, & j = J. \end{cases} \tag{3.34}$$

Axial gradient of V.

The axial gradient of V, $\frac{\partial V}{\partial x}$, is calculated using a second-order backward interpolation to construct a polynomial of V as function of x at radial coordinate r_j. This polynomial is then differentiated and the average between the polynomials at r_j and r_{j+1} is taken to determine the cell-centred value. The quadratic polynomial is a function of $V_{i-2,j}$, $V_{i-1,j}$, and $V_{i,j}$, located at axial coordinates $x_{i-3/2}$, $x_{i-1/2}$, and $x_{i+1/2}$, and it looks as follows:

$$\begin{aligned} V_j(x) = V_{i-2,j}\, &\frac{(x - x_{i-1/2})(x - x_{i+1/2})}{(x_{i-3/2} - x_{i-1/2})(x_{i-3/2} - x_{i+1/2})} \\ + V_{i-1,j}\, &\frac{(x - x_{i-3/2})(x - x_{i+1/2})}{(x_{i-1/2} - x_{i-3/2})(x_{i-1/2} - x_{i+1/2})} \\ + V_{i,j}\, &\frac{(x - x_{i-3/2})(x - x_{i-1/2})}{(x_{i+1/2} - x_{i-3/2})(x_{i+1/2} - x_{i-1/2})}. \end{aligned} \tag{3.35}$$

This polynomial is then differentiated and evaluated at the cell centre $x_{i+1/2}$

$$\left(\frac{\partial V}{\partial x}\right)_{i,j}^{\text{face}} = c_1\, V_{i-2,j} + c_2\, V_{i-1,j} + c_3\, V_{i,j}, \tag{3.36}$$

where the coefficients are defined as

$$\begin{aligned} c_1 &= \frac{x_{i+1/2} - x_{i-1/2}}{(x_{i-3/2} - x_{i-1/2})(x_{i-3/2} - x_{i+1/2})}, \\ c_2 &= \frac{x_{i+1/2} - x_{i-3/2}}{(x_{i-1/2} - x_{i-3/2})(x_{i-1/2} - x_{i+1/2})}, \\ c_3 &= \frac{(x_{i+1/2} - x_{i-3/2}) + (x_{i+1/2} - x_{i-1/2})}{(x_{i+1/2} - x_{i-3/2})(x_{i+1/2} - x_{i-1/2})}. \end{aligned} \tag{3.37}$$

Taking the average between the values of the upper and lower horizontal faces of a cell yields the cell centred value:

$$\left(\frac{\partial V}{\partial x}\right)_{i,j} = \frac{1}{2}\left[\left(\frac{\partial V}{\partial x}\right)_{i,j}^{\text{face}} + \left(\frac{\partial V}{\partial x}\right)_{i,j+1}^{\text{face}}\right]. \tag{3.38}$$

Azimuthal strain term V/r.

By averaging the values of V/r at the upper and lower horizontal faces of a cell, the cell-centred value is determined.

$$\left(\frac{V}{r}\right)_{i,j} = \frac{1}{2}\left(\frac{V_{i,j}}{r_j} + \frac{V_{i,j+1}}{r_{j+1}}\right). \tag{3.39}$$

However, at r_0, both the radial velocity V and coordinate r are zero, which makes the strain term V/r not defined. L'Hôpital's rule is applied, giving $\lim_{r\to 0} V/r = \partial V/\partial r$. Because of the axisymmetric coordinate system, $\partial V/\partial r = 0$, which results in the strain term at the axis of symmetry being always zero. So the cell centred strain term of the boundary cell yields

$$\left(\frac{V}{r}\right)_{i,0} = \frac{1}{2}\,\frac{V_{i,1}}{r_1}. \tag{3.40}$$

Integrated Production Term

The five contributions to the production term are collected in a single scalar value $\Phi_{i,j}$ for each cell

$$\Phi_{i,j} = 2\left(\frac{\partial U}{\partial x}\right)_{i,j}^2 + 2\left(\frac{\partial V}{\partial r}\right)_{i,j}^2 + \left[\left(\frac{\partial U}{\partial r}\right)_{i,j} + \left(\frac{\partial V}{\partial x}\right)_{i,j}\right]^2 + 2\left(\frac{V}{r}\right)_{i,j}^2, \tag{3.41}$$

simplifying the production term to $P_{k_{i,j}} = \nu_{T_{i,j}}\, \Phi_{i,j}$.

For any column i, the scalar values of each cell are put into a vector

$$\vec{\Phi}_i = \begin{pmatrix} \Phi_{i,0} \\ \Phi_{i,1} \\ \vdots \\ \Phi_{i,J} \end{pmatrix}. \tag{3.42}$$

The production term integrated over a volume uses a vector containing the volume of each cell in a column:

$$d\vec{V}_i = \pi\,\Delta x_i \begin{pmatrix} r_1^2 - r_0^2 \\ r_2^2 - r_1^2 \\ \vdots \\ r_{J+1}^2 - r_J^2 \end{pmatrix}, \tag{3.43}$$

so that the result production vector integrated over a cell volume is

$$\vec{F}_i^{\,P_k} = \vec{\nu}_{T,i} \odot \vec{\Phi}_{k,i} \odot d\vec{V}_i. \tag{3.44}$$

Production in the ε-Equation
The production term in the ε-equation is

$$P_\varepsilon = C_{\varepsilon 1}\,\frac{\varepsilon}{k}\,P_k, \tag{3.45}$$

For axial column i, the production term integrated over a volume becomes.

$$\vec{F}_i^{\,P_\varepsilon} = C_{\varepsilon 1}\left(\frac{\vec{\varepsilon}_i}{\vec{k}_i}\right) \odot \vec{\nu}_{T,i} \odot \vec{\Phi}_i \odot d\vec{V}_i, \tag{3.46}$$

where the division $\frac{\vec{\varepsilon}_i}{\vec{k}_i}$ is done per element.

3.2.4 Dissipation Terms

The dissipation term in the k-equation is given by ε. Integrating over a cell volume and collecting all terms in axial column i yields

$$\vec{F}_i^{\,d_k} = \vec{\varepsilon}_i \odot d\vec{V}_i, \tag{3.47}$$

where $\vec{\varepsilon}_i = (\varepsilon_{i,0},\, \ldots,\, \varepsilon_{i,J})^{\mathsf{T}}$ and $d\vec{V}_i$ contains the cell volumes of that column.

In the ε-equation, the destruction term is given by $C_{\varepsilon 2}\,\varepsilon^2/k$. For control volume (i,j) this gives

$$D_{\varepsilon_{i,j}} = C_{\varepsilon 2}\,\frac{\varepsilon_{i,j}^2}{k_{i,j}}.$$

Integrating over a cell volume and collecting all terms in axial colum i in a vector yields.

$$\vec{F}_i^{\,d_\varepsilon} = C_{\varepsilon 2}\left(\frac{\vec{\varepsilon}_i^{\,2}}{\vec{k}_i}\right) \odot d\vec{V}_i. \tag{3.48}$$

The square and division $\left(\frac{\vec{\varepsilon}_i^{\,2}}{\vec{k}_i}\right)$ are applied per element.

3.2.5 Sink Term in the k-Equation

One of the additions to the standard $k-\varepsilon$ model in this thesis is an extra sink term in the k-equation, which accounts for the extraction of turbulent kinetic energy by the turbine forces. This term is derived analytically from the turbine induced force F:

$$F = -\frac{1}{2} C_T' A_{\text{cell}} \left(u_{d,x}^2\right) \frac{\gamma_{i,j}}{V_{\text{cell}}}. \tag{3.49}$$

The sink term S_k comes from the the correlation between the fluctuating velocity and the fluctuating turbine force, $\overline{u_i f_i}$, and is defined as

$$S_k = -\frac{1}{2}\,C_T'\,A_{\text{cell}}\left(2\,u_d^2\,U_d + u_d^3\right)\frac{\gamma_{i,j}}{V_{\text{cell}}}. \tag{3.50}$$

In this equation, A_{cell} is the frontal area of cell volume that intersects the rotor, V_{cell} is that cell's volume, $\gamma_{i,j}$ is the fraction of the area lying inside the rotor disk, and $u_d$is the turbulent velocity fluctuation at the disk in axial direction. The quantity C'_T is the local thrust coefficient, calculated through the global thrust coefficient by $C'_T = C_T/(1-a)^2$, where a is the induction factor which results from the disk averaged mean axial velocity.

In Equation 3.50, u_d^2 is unknown. The expression is closed by assuming isotropic turbulence and by calculating the fluctuating velocity using k: $u_d^2 = \frac{2}{3}\,k_d$, where k_d is the disk-averaged value of k. This yields the following result for the expression of S_k.

$$S_k = -\frac{1}{2}\,C'_T\,A_{\text{cell}}\left(\frac{4}{3}\,k_d\,U_{d,x} + \left(\frac{2}{3}\,k_d\right)^{3/2}\right)\frac{\gamma_{i,j}}{V_{\text{cell}}}. \tag{3.51}$$

Inside the turbulence model, the sink term is updated during each iteration of the nonlinear solver. Firstly, the induction factor a is calculated and used to compute the local thrust coefficient C'_T. Then the disk-averaged values of k_d and $U_{d,x}$ are determined to calculate the value of S_k.

The sink term is then integrated over a control volume $\Omega_{i,j}$, by multiplying Equation 3.51 by V_{cell}. This cancels the volume term in the denominator and leaves only the frontal area $A_{\text{cell}} = \pi(r_{j+1}^2 - r_j^2)$:

$$\iiint_{\Omega_{i,j}} S_k\,d\Omega = -\frac{1}{2}\,C'_T\,\pi\left(r_{j+1}^2 - r_j^2\right)\left(\frac{4}{3}\,k_d\,U_{d,x} + \left(\frac{2}{3}\,k_d\right)^{3/2}\right)\gamma_{i,j}. \tag{3.52}$$

For axial column i, the sink term of each radial cell are put into one vector

$$\vec{F}_i^{\,S_k} = -\frac{1}{2}\,C'_T\,\pi\left(\frac{4}{3}\,k_d\,U_{d,x} + \left(\frac{2}{3}\,k_d\right)^{3/2}\right)\begin{pmatrix}(r_1^2 - r_0^2)\,\gamma_{i,0}\\ \vdots \\ (r_{J+1}^2 - r_J^2)\,\gamma_{i,J}\end{pmatrix}. \tag{3.53}$$

k_d, $U_{d,x}$, and C'_T are disk-averaged quantities, so they are the same for each cell. Only the geometric terms vary among the cells.

Regularization of the Sink Term

In the formulation of Equation 3.53 that is just described, the sink term is applied only to the axial column that contains the actuator disk and to the radial cells whose frontal area intersects with the rotor. This leads to a Dirac delta distribution of the sink term in the axial direction and a step distribution in the radial direction, which may cause numerical instabilities. To prevent these issues, a regularization step is applied to the sink term so that the sink term is distributed over a region in both the axial and radial directions.

Axial regularization.

Along the streamwise direction, the sink term is distributed over multiple axial columns using a symmetric Gaussian weight function centred at the actuator disk location x_{AD}:

$$w_i^x = \frac{\exp\left(-\dfrac{(x_{\rho,i} - x_{\text{AD}})^2}{2\,\sigma_x^2}\right)}{\displaystyle\sum_{n=1}^{N}\exp\left(-\frac{(x_{\rho,n} - x_{\text{AD}})^2}{2\,\sigma_x^2}\right)}, \tag{3.54}$$

where $x_{\rho,i}$ is the cell-centre coordinate of column i and σ_x is the axial spreading width. The summation in the denominator ensures that the weights are normalized, $\sum_i w_i^x = 1$. The Gaussian is truncated at $\pm 3\sigma_x$ from the disk, beyond which the weights are negligible. Setting $\sigma_x = 0$ results in the original unregularized form in which the sink is applied at the disk axial coordinate alone.

Radial regularization.

In the radial direction, the geometric overlap fraction $\gamma_{i,j}$ of Equation 3.52 is replaced by a smooth profile based on the error function:

$$\tilde{\gamma}_j = \frac{1}{2}\left[1 - \text{erf}\left(\frac{r_{\rho,j} - R}{\sigma_r\sqrt{2}}\right)\right], \tag{3.55}$$

where $r_{\rho,j}$ is the cell-centre radius, $R = D/2$ is the rotor radius, and σ_r controls the width of the transition region near the rotor tip. To preserve the disk area, the profile is normalized so that the smooth matches that of the original profile:

$$\hat{\gamma}_j = \tilde{\gamma}_j \, \frac{\sum_j \gamma_j \left(r_{j+1}^2 - r_j^2\right)}{\sum_j \tilde{\gamma}_j \left(r_{j+1}^2 - r_j^2\right)}. \tag{3.56}$$

When $\sigma_r = 0$, the original overlap is recovered.

Regularized sink term.

With both regularization steps applied, the sink term at axial column i and radial cell j becomes

$$S_{k,i,j}^{\text{reg}} = -\frac{w_i^x}{2} C_T' \, \pi \left(r_{j+1}^2 - r_j^2\right) \left(\frac{4}{3} \, k_{d,i} \, U_{d,x,i} + \left(\frac{2}{3} \, k_{d,i} \right)^{3/2} \right) \hat{\gamma}_j \, , \tag{3.57}$$

where the disk-averaged quantities $k_{d,i}$ and $U_{d,x,i}$ are now evaluated from the *local* flow state at column i rather than from a single evaluation at the actuator disk. This means that the induction factor a_i and the corrected thrust coefficient $C_{T,i}'$ are also recomputed at each column from the local velocity field.

Note on conservation.

The axial weights are normalized to sum to unity, and the radial profile is renormalized to preserve the total disk area. However, because the disk-averaged quantities $k_{d,i}$ and $U_{d,x,i}$ vary from column to column, the total integrated sink term is not strictly conserved:

$$\sum_{i=1}^{N} \sum_{j=0}^{J} S_{k,i,j}^{\text{reg}} \;\neq\; \sum_{j=0}^{J} S_{k,j}^{\text{unreg}}. \tag{3.58}$$

This was done for the following reasons. First, the regularization widths σ_x and σ_r are taken to be small relative to the rotor diameter, so the variation in the disk-averaged quantities across the regularized region is small and the conservation error should also remain small. Second, enforcing conservation would require either pre-computing the sink term from a single set of flow quantities or introducing a correction step that redetermines the distributed sink term after each iteration, which is impractical with the parabolization approach of the model.

3.2.6 The f_P Correction

In the k–ε–f_P turbulence model proposed by van der Laan [46], the standard constant C_μ in the eddy viscosity definition is replaced by a variable coefficient to account for strong velocity gradients. The modified eddy viscosity is defined as

$$\nu_T = C_\mu^* \, \frac{k^2}{\varepsilon}, \qquad C_\mu^* = C_\mu \, f_P, \tag{3.59}$$

where f_P is a correction factor that reduces the eddy viscosity in regions where the standard k–ε model is known to overpredict turbulent stresses, for instance in the near-wake of a wind turbine where velocity gradients are large.

The correction factor f_P is a function of the ratio of the local shear parameter σ to its equilibrium value $\tilde{\sigma}$, and is given by

$$f_P\left(\frac{\sigma}{\tilde{\sigma}}\right) = \frac{2 \, f_0}{1 + \sqrt{1 + 4 \, f_0 \, (f_0 - 1) \left(\frac{\sigma}{\tilde{\sigma}}\right)^2}}, \qquad f_0 = \frac{C_R}{C_R - 1}, \tag{3.60}$$

where C_R is the Rotta constant, set to $C_R = 4.5$ following van der Laan's model calibration. By construction, $f_P = 1$ when $\sigma = \tilde{\sigma}$ (equilibrium conditions) and $f_P < 1$ when $\sigma > \tilde{\sigma}$ (above- equilibrium shear), thereby reducing the eddy viscosity.

The local shear parameter σ quantifies the deviation of the flow from the log-law equilibrium conditions for which the standard k–ε model was calibrated. It is defined as

$$\sigma = \frac{k}{\varepsilon} \, S, \qquad S = \sqrt{2 \, S_{ij} \, S_{ij}} = \sqrt{\Phi}, \tag{3.61}$$

where S is the strain-rate magnitude and Φ is the contracted strain-rate scalar as it was computed in Equation 3.41. The reference value $\tilde{\sigma}$ corresponds to the shear parameter in an equilibrium boundary layer that obeys the log law, for which

$$\tilde{\sigma} = \frac{k}{\varepsilon} \left\| \frac{\partial U}{\partial z} \right\|_{\text{eq}} = \frac{1}{\sqrt{C_\mu}}. \tag{3.62}$$

Because $\tilde{\sigma}$ depends on C_μ, the correction factor f_P in Equation 3.60 is implicitly a function of C_μ as well.

During each iteration of the nonlinear solution process of the k- and ε-equations, the shear parameter σ and the correction factor f_P are calculated using the updated values of k, ε, and the velocity gradients. The updated coefficient $C_\mu^* = C_\mu f_P$ is used to obtain the new eddy viscosity, after which the transport equations are solved again. This procedure is repeated until both equations have converged.

3.3 Assembly and Solution of the Discretized Equations

Combining the convective, diffusive, production, dissipation, and sink contributions derived in the previous section, the fully discretized k-equation for axial column i becomes

$$\mathbf{A}\Big(a_i^1 \vec{U}_{i+1} \odot \vec{k}_i - \big(a_i^2 \vec{U}_{i+1} + a_i^3 \vec{U}_i\big) \odot \vec{k}_{i-1} + a_i^4 \vec{U}_i \odot \vec{k}_{i-2}\Big) + \mathbf{B}\,\vec{k}_i = \frac{1}{\sigma_k}\mathbf{D}\,\vec{k}_i + \vec{F}_i^{P_k} - \vec{F}_i^{d_k} + \vec{F}_i^{S_k}, \tag{3.63}$$

and the corresponding ε-equation becomes

$$\mathbf{A}\Big(a_i^1 \vec{U}_{i+1} \odot \vec{\varepsilon}_i - \big(a_i^2 \vec{U}_{i+1} + a_i^3 \vec{U}_i\big) \odot \vec{\varepsilon}_{i-1} + a_i^4 \vec{U}_i \odot \vec{\varepsilon}_{i-2}\Big) + \mathbf{B}\,\vec{\varepsilon}_i = \frac{1}{\sigma_\varepsilon}\mathbf{D}\,\vec{\varepsilon}_i + \vec{F}_i^{P_\varepsilon} - \vec{F}_i^{d_\varepsilon}. \tag{3.64}$$

In these expressions, the matrices **A**, **B**, and **D** as well as the source and sink vectors are defined in Section 3.2.1–Section 3.2.5.

Linearization

Both Equation 3.63 and Equation 3.64 are nonlinear. For instance, the diffusion operator **D** depends on the eddy viscosity ν_T, which is a function of k and ε, and the source terms in the ε-equation contains ε divided by k. A fixed-point iteration is used to solve these coupled nonlinear systems. This approach is chosen because of its simplicity and it does not require the need to determine a Jacobian matrix.

The linearization is done as follows. At the start of each iteration, the values of k and ε from the previous upstream column is used as the initial guess. This initial gues is used to calculate the eddy viscosity, $\nu_T^{(n)} = C_\mu\,(k^{(n)})^2/\varepsilon^{(n)}$, which is then held constant while solving the transport equations. This removes the nonlinearity from the diffusion operator in both the k- and ε-equations.

In the ε-equation, the values of k in the denominators of the production and destruction terms are frozen at their current guessed value $k^{(n)}$. Next to this, one factor of ε in the destruction term $C_{\varepsilon 2}\,\varepsilon^2/k$ is also kept constant at $\varepsilon^{(n)}$, leaving one factor that is linear in the unknown ε. Both equations are now linear and can be solved as standard linear systems for $\vec{k}_i^{(n+1)}$ and $\vec{\varepsilon}_i^{(n+1)}$. The new values then replace the frozen quantities. The iterations stop when the absolute differences between of k and ε reach a prescribed tolerance. In the validation cases presented in Chapter 5, this tolerance is set to 10^{-8}.

Implicit Treatment of Sink Terms

To improve the stability of the iteration, the sink terms in both equations are treated implicitly. Moving sinks to the left-hand side of the linear system increases the diagonal dominance of the left hand side of the resulting equation, which increases the chance of convergence of the iterative solver.

In the k-equation, the dissipation and turbine sink terms are divided point-wise by k and moved to the left-hand side of the equation. The resulting factors of k in the denominator are linearized by keeping them constant at the value from the previous iteration, $k^{(n)}$. Defining the diagonal matrices

$$\mathbf{E}_k = \text{diag}\left(\frac{\vec{\varepsilon}_i^{(n)}}{\vec{k}_i^{(n)}} \odot d\vec{V}_i\right), \qquad \mathbf{S}_k = \text{diag}\left(\frac{\vec{F}_i^{S_k}}{\vec{k}_i^{(n)}}\right), \tag{3.65}$$

the linearized k-equation becomes

$$\underbrace{\mathbf{A} \odot \text{diag}\big(a_i^1 \vec{U}_{i+1}\big)}_{\text{axial outflow}} \vec{k}_i^{(n+1)} + \mathbf{B}\,\vec{k}_i^{(n+1)} - \frac{1}{\sigma_k}\mathbf{D}\,\vec{k}_i^{(n+1)} + \mathbf{E}_k\,\vec{k}_i^{(n+1)} - \mathbf{S}_k\,\vec{k}_i^{(n+1)} = \vec{F}_i^{P_k} + \vec{r}_i^{k}, \tag{3.66}$$

where $\vec{r}_i^{\,k}$ contains the known upstream contributions from $\vec{k}_{i-1}$ and $\vec{k}_{i-2}$.

In the ε-equation, the destruction term is already quadratic in ε, so it can be moved to the left-hand side directly without dividing by ε. Defining

$$\mathbf{E}_\varepsilon = \mathrm{diag}\left(C_{\varepsilon 2}\, \frac{\vec{\varepsilon}_i^{(n)}}{\vec{k}_i^{(n)}} \odot d\vec{V}_i \right), \tag{3.67}$$

the linearized ε-equation takes the same structure as Equation 3.66, with $\mathbf{E}_\varepsilon$ replacing $\mathbf{E}_k$ and the production and upstream terms adjusted accordingly:

$$\underbrace{\mathbf{A} \odot \mathrm{diag}\big(a_i^1\, \vec{U}_{i+1}\big)}_{\text{axial outflow}}\, \vec{\varepsilon}_i^{(n+1)} + \mathbf{B}\, \vec{\varepsilon}_i^{(n+1)} - \frac{1}{\sigma_\varepsilon}\, \mathbf{D}\, \vec{\varepsilon}_i^{(n+1)} + \mathbf{E}_\varepsilon\, \vec{\varepsilon}_i^{(n+1)} = \vec{F}_i^{P_\varepsilon} + \vec{r}_i^{\,\varepsilon}. \tag{3.68}$$

Both systems can be written in the compact form $\mathbf{M}\,\vec{\phi} = \vec{b}$, where $\vec{\phi}$ represents either $\vec{k}_i$ or $\vec{\varepsilon}_i$. The calculations are repeated until the change in both $\vec{k}_i$ and $\vec{\varepsilon}_i$ between iterations falls below the prescribed tolerance.

To further increase the stability of the fixed-point iteration, an under-relaxation factor $\omega \in (0,\, 1]$ is applied when updating the values of k and ε after each iteration. At each iteration, the new estimate is computed as

$$\vec{\phi}_i^{(n+1)} \leftarrow \vec{\phi}_i^{(n)} + \omega\big(\vec{\phi}_i^{(n+1)} - \vec{\phi}_i^{(n)}\big), \tag{3.69}$$

where $\vec{\phi}$ represents either $\vec{k}_i$ or $\vec{\varepsilon}_i$. A value of $\omega = 0.4$ was used in this thesis, since it was found to provide stability for most simulation cases considered. Furthermore, the iteration is stopped after 50 steps regardless of the residual, to prevent being stuck in a loop if a column does not converge to the given tolerance. However, convergence is usually achieved within 10 iterations.

3.4 Coupling with the Wake Deficit Model

The k–ε model described above provides the eddy viscosity needed by the wake deficit model, while the wake deficit model provides the velocity field needed by the turbulence model. A Picard iteration scheme is used to resolve this coupling column by column as the solver marches in the axial direction. Figure 3.2 gives an overview of the complete iteration process. At each axial column i, an initial estimate of the eddy viscosity is obtained from the upstream values of k and ε. The wake deficit model is then called, which uses this initial eddy viscosity to compute the axial outflow velocity of that column. This outflow velocity is subsequently used by the turbulence model to obtain a new estimate of the eddy viscosity. The updated eddy viscosity is passed back to the wake deficit model and the process is repeated. When the absolute differences of U and ν_T between two successive iterations fall below a prescribed tolerance, the solver stops iterating and moves on to the next axial column. In the validation cases considered in Chapter 5, the tolerance was set to 10^{-8}.

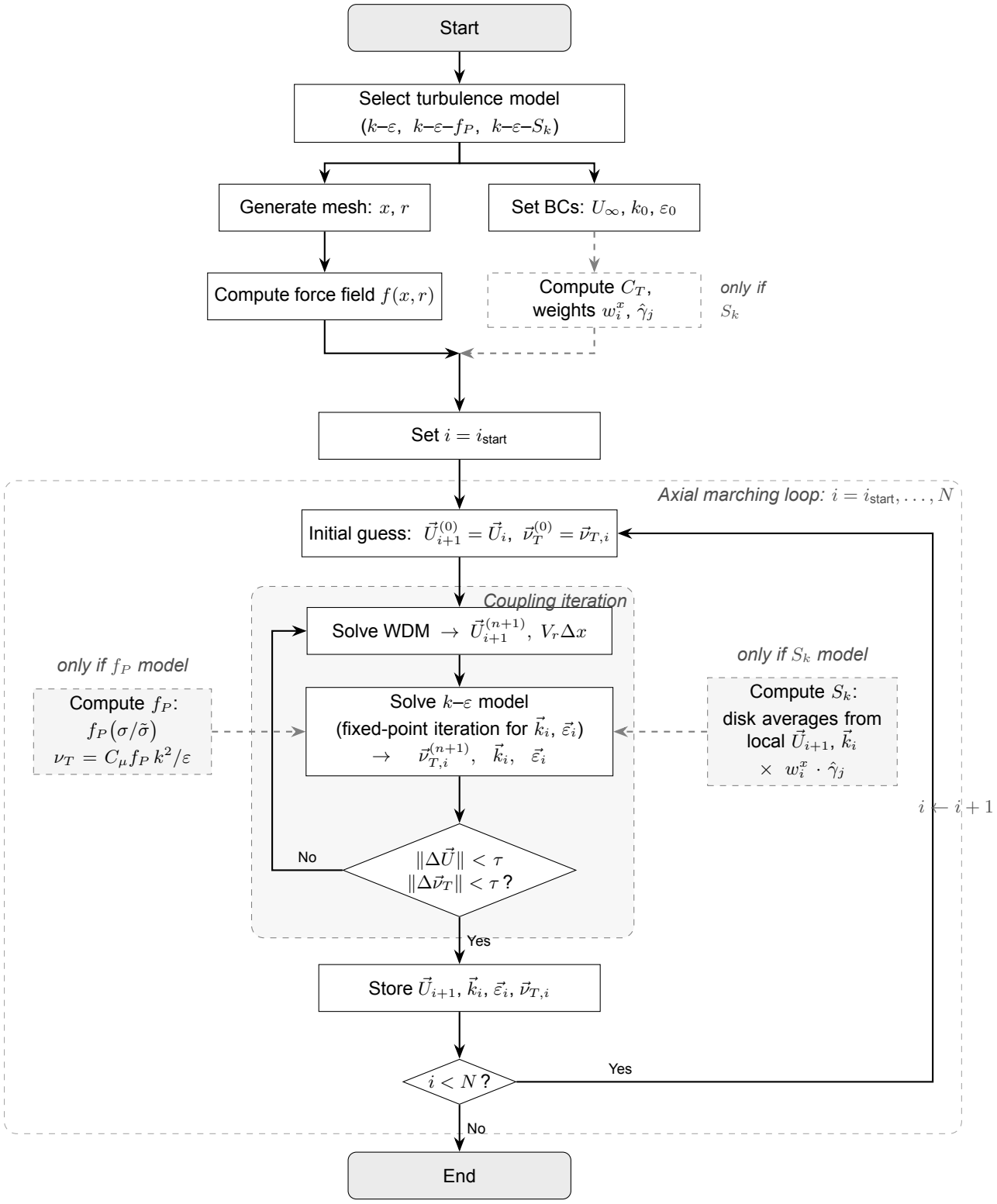

Figure 3.2: Flowchart of the coupled wake deficit and k–ε solver. At each axial column i, the wake deficit model (WDM) and the turbulence model exchange velocity and eddy viscosity until convergence. Dashed boxes indicate optional steps: the f_P correction is active only for the k–ε–f_P model, and the sink term S_k with its regularization weights is active only for the k–ε–S_k model.

4 Verification of the Numerical Implementation

Three steps are taken to verify the model. First, the standalone turbulence model is verified. This is done by simulating the canonical flow case of the decay of isotropic turbulence. This flow case has a power law as a known analytical solution, so it can be used to asses whether the k- and ε-equations have been properly coupled. The turbulence model is isolated by prescribing a uniform velocity field and excluding the wake deficit solver.

The second step uses the Method of Manufactured Solution (MMS) to verify the complete coupled solver. Because there is no known analytical solution that could be compared with results of the coupled solver, MMS prescribes a solution for U, k and ε. These manufactured solutions are substituted into the governing equations, which results in residual terms, since the given solutions are not actual solutions to the equations. The residual terms are then added as source terms to the model equations, forcing the model equations to agree with the manufactured solutions. This allows for a direct comparison between simulation results of the coupled solver and the manufactured solutions.

The last step involves simulating a coflowing jet. This is done using the coupled solver without any manufactured source terms. There is no known analytical solution to this flow case, but it is well known that the flow variable's profiles become self-similar in the far-field. This makes it possible to check whether the solver can reproduce the expected physical behaviour. The simulation results are compared against reference data from literature.

In the first two verification stages, a grid-convergence study will be performed. This is done to asses whether the observed order of accuracy matches with the order of the used discretization methods. This is done by determining the discretization error between the numerical and analytical solutions using the mean absolute percentage error (MAPE) and the relative root-mean-square error (RRMSE) using different mesh sizes. With each mesh refinement, the error should reduce according the discretization method's order. No grid-convergence study is performed for the self-similar test case, since there is no analytical solution to compare against.

The chapter has the following four sections. Section 4.1 explains the error metrics and the grid-convergence methodology. Section 4.2 presents the first test case of the canonical turbulent decay. Section 4.3 describes the MMS verification of first the standalone turbulence model and then the fully coupled solver. Finally, Section 4.4 shows the results of the the self-similar round-jet case.

4.1 Grid Convergence Methodology

For the first two verification methods, grid convergence studies will be performed. These are done to quantify the discretization error in the numerical solution. The same simulation will be run on meshes with different levels of refinement. With each finer grid, the discretization error should decrease and approach zero.

The discretisation error is defined as the difference between the numerical solution and the exact solution, which can be representented as a function of the cell size h by a power series, which is shown in Equation 4.1 Roache [58]. Here C is a constant, p is the order of accuracy, and H.O.T. denotes higher-order terms. The order of accuracy corresponds to the leading term of the truncation error. For a second-order method, $p = 2$. The observed order of accuracy can be expected to be lower than the formal order due to treatment of boundary conditions or a non-uniform grid. If in the first line of Equation 4.1 all higher order terms are neglect and the log is taken, a linear relation appears, as shown in the second line. The slope of this line is then the observed order of accuracy.

$$\begin{aligned} E &= f(h) - f_{\text{exact}} = C\,h^p + \text{H.O.T.}, \\ \log(E) &= \log(C) + p\,\log(h). \end{aligned} \tag{4.1}$$

The mean absolute percentage error (MAPE) and the relative root-mean-square error (RRMSE) are used as the two metrics to quantify the discretization error. Their definitions are given in Equation 4.2. The quantities $\phi_{\text{exact},i}$ and $\phi_{\text{num},i}$

are the exact and numerical values of a flow variable at point i, and n is the total number of points.

$$\begin{aligned} \text{MAPE} &= \frac{1}{n}\sum_{i=1}^{n}\left|\frac{\phi_{\text{exact},i}-\phi_{\text{num},i}}{\phi_{\text{exact},i}}\right|, \\ \text{RRMSE} &= \frac{\sqrt{\dfrac{1}{n}\displaystyle\sum_{i=1}^{n}\left(\phi_{\text{exact},i}-\phi_{\text{num},i}\right)^2}}{\dfrac{1}{n}\displaystyle\sum_{i=1}^{n}\left|\phi_{\text{exact},i}\right|}. \end{aligned} \tag{4.2}$$

Because each error metric has a limitation, both of them are used. Because MAPE normalises the error by the local exact value, the metric becomes unreliable when the solution becomes zero [59]. And RRMSE is sensitive to local outliers, since it squares the errors before averaging. If both metric are in agreement, this will improve the trustworthiness that the observed order of accuracy is indeed correctly reflects the model's order.

In numerical models, other error sources besides discretization errors are round-off and iterative error. Since only the discretization error decreases with grid refinement, the other two errors must be negligible compared tot he discretization errors in order for the grid-convergence study to be meaningful.

Round-off errors are limited by the floating-point precision. For the smooth solutions considered here, double-precision arithmetic ensure sufficiently small errors. Iterative errors arises from incomplete convergence of the nonlinear fixed-point iteration described in Section 3.3. Theoretically, they could be reduced to the same level of the round-off errors. However, this would make the simulations very expensive on very find and large meshes, or in the case of stiff source terms. In the next verification cases, the solver residuals are reduced to 10^{-12}, which is approximately six orders of magnitude below the smallest error observed in any of the tests. This ensures the calculated errors can be attributed to discretization errors only.

4.2 Canonical Flow

The first verification case is the decay of homogeneous isotropic turbulence. This test is done to verify the coupling between the k- and ε equations and the implementation of the destruction terms. The flow is uniform, homogeneous, isotropic and aligned with the axial direction, so there are no velocity gradients and no production and diffusion of any of the flow variables. The only leftover terms are the convective terms in axial direction and destruction terms.

This reduces the k–ε model reduces to a system of two ordinary differential equations, as shown in Equation 4.3. In these equations,the axial coordinate x has been replaced by a temporal coordinate t (using the unit convection velocity $U = 1$).

$$\frac{dk}{dt} = -\varepsilon, \tag{4.3a}$$

$$\frac{d\varepsilon}{dt} = -C_{2\varepsilon}\,\frac{\varepsilon^2}{k}. \tag{4.3b}$$

This system has an analytical solution that follows a power-law Pope [19]:

$$k(t) = k_0\left(\frac{t}{t_0}\right)^{-n}, \qquad \varepsilon(t) = \varepsilon_0\left(\frac{t}{t_0}\right)^{-(n+1)}, \tag{4.4}$$

where the decay exponent n is calculated through the model constant with $n\,C_{2\varepsilon} = n + 1$. The initial value of the dissipation rate follows from consistency with the power law at $t = t_0$:

$$\varepsilon_0 = \frac{n\,k_0}{t_0}. \tag{4.5}$$

The test has the following setup. The computational domain spans $x \in [1, 2]$, corresponding to $t \in [1, 2]$ with unit convection velocity and $r \in [0, 1]$. The initial conditions are $k_0 = 1$ and $C_{2\varepsilon} = 1.92$, which gives $n = 1/(C_{2\varepsilon} - 1) \approx 1.087$ and $\varepsilon_0 = n\,k_0/t_0 \approx 1.087$. Only the dissipation terms are active, while the production, diffusion, and radial convection terms are all disabled. Although the analytical solution is uniform in the radial direction, the problem is solved on the

full two-dimensional grid with $M = N$ cells in each direction. This confirms that the solver correctly reduces to a one-dimensional problem when the radial terms are inactive.

Six simulations are performed on continuously finer grids with $N \in \{8, 16, 32, 64, 128, 256\}$, where N is the number of cells in both axial and radial directions. The results of the grid-convergence study are shown in Figure 4.1. The left figure presents the global error metrics as a function of grid spacing. The nearly straight lines on the logarithmic scale indicate that the simulations are within the asymptotic convergence range. This confirms that the grid resolution is sufficiently fine for the truncation error to dominate, while round-off and iterative errors are negligible.

The right panel shows the estimated order of accuracy. For both k and ε, the observed order approaches the theoretical value of $p = 2$, which is in agreement with the second-order discretisation. The error levels for ε are larger than those for k, and its observed order is slightly lower. This can be explained by the fact that the ε-equation contains the nonlinear destruction term ε^2/k, which introduces stronger stiffness and sensitivity to numerical errors than the linear sink term in the k-equation.

A difference is visible between the convergence behaviour measured with MAPE and RRMSE. For both variables, the observed order based on RRMSE is slightly lower than that obtained from MAPE. This is because RRMSE is based on squared errors and is therefore more sensitive to outliers where the numerical error is large. In the turbulent decay case, such regions occur near $t = t_0$, where the dissipation rate is highest and the nonlinearity of the ε-equation is strongest. The fact that both metrics still approach second-order behaviour indicates that this discrepancy is caused by the sensitivity of the norm and not by an error in the implementation.

Overall, this test verifies the correct coupling between the k and ε equations and confirms the proper implementation of the dissipation terms.

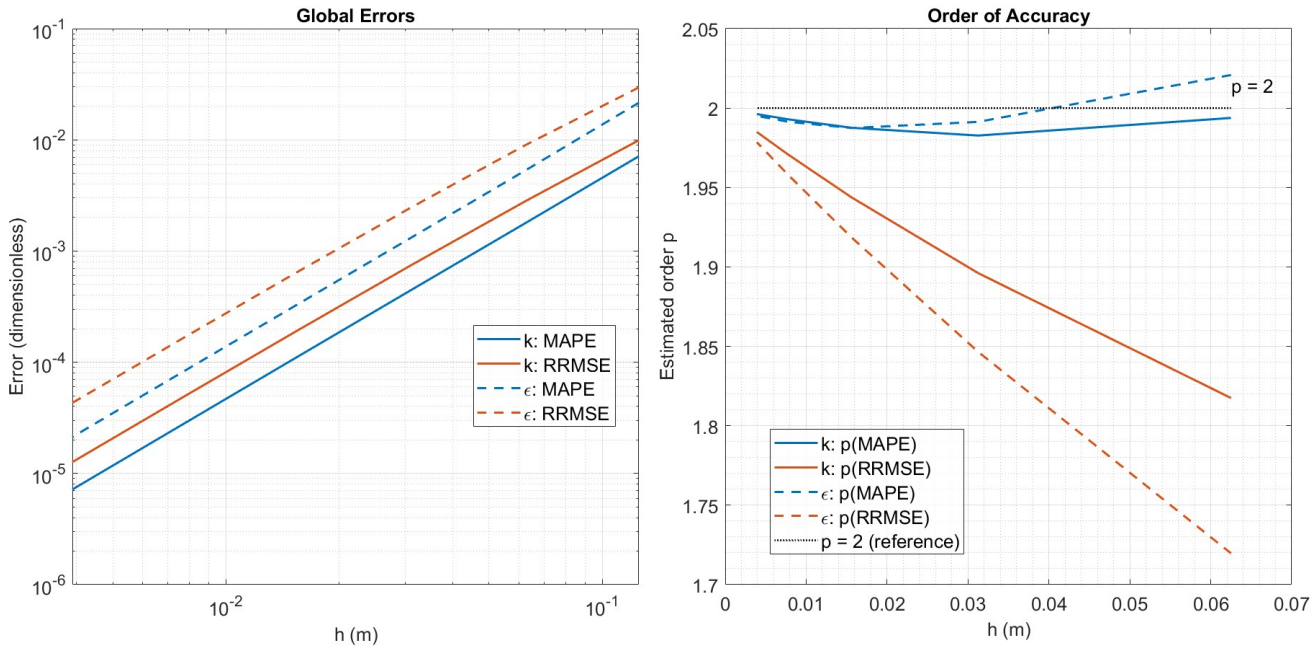

Figure 4.1: Grid-convergence results for the isotropic turbulence decay test. Left: global error metrics (MAPE and RRMSE) as a function of grid spacing h on a logarithmic scale. Right: estimated order of accuracy for each metric. Solid lines correspond to k, dashed lines to ε. The dotted line marks the theoretical reference $p = 2$.

4.3 Method of Manufactured Solutions

To verify the implementation and coupling of the complete model, the Method of Manufactured Solutions (MMS) is used. This is done in three steps. First, the standalone k–ε turbulence model is tested without the wake deficit solver. Second, the standalone k–$\varepsilon - f_P$ turbulence model is tested without the wake deficit solver. Lastly, the full coupled solver is tested, without the f_P correction. No analytical solution exists for these system of equations, so MMS is used to provide a means with which to asses the discretization error and the order of accuracy of the solver.

Manufactured solutions

The MMS procedure requires smooth, differentiable functions to be prescribed for all flow variables. These flow variables are the turbulent kinetic energy k, the dissipation rate ε, and the axial velocity U. Their manufactured solutions are given in Equation 4.6. Each field consists of a mean value and cosine perturbations in the axial and radial directions. The perturbation amplitudes (k_x, k_r, etc.), frequencies (a_{kx}, a_{kr}, etc.), and the domain length L are free parameters that can be adjusted to control the ratios between the different source terms.

$$k(x,r) = k_0 + k_x \cos\!\left(\frac{a_{kx}\,\pi\,x}{L}\right) + k_r \cos\!\left(\frac{a_{kr}\,\pi\,r}{L}\right) + k_{xr} \cos\!\left(\frac{a_{kxr}\,\pi\,x\,r}{L^2}\right), \tag{4.6a}$$

$$\varepsilon(x,r) = \varepsilon_0 + \varepsilon_x \cos\!\left(\frac{a_{\varepsilon x}\,\pi\,x}{L}\right) + \varepsilon_r \cos\!\left(\frac{a_{\varepsilon r}\,\pi\,r}{L}\right) + \varepsilon_{xr} \cos\!\left(\frac{a_{\varepsilon xr}\,\pi\,x\,r}{L^2}\right), \tag{4.6b}$$

$$U(x,r) = U_0 + U_x \cos\!\left(\frac{a_{Ux}\,\pi\,x}{L}\right) + U_r \cos\!\left(\frac{a_{Ur}\,\pi\,r}{L}\right) + U_{xr} \cos\!\left(\frac{a_{Uxr}\,\pi\,x\,r}{L^2}\right). \tag{4.6c}$$

The mean values must satisfy $k_0 > |k_x| + |k_r| + |k_{xr}|$ and $\varepsilon_0 > |\varepsilon_x| + |\varepsilon_r| + |\varepsilon_{xr}|$ so that both k and ε remain strictly positive over the entire domain. Also, U_0 must large enough to ensure a positive flow over the entire domain.

Two additional variable functions are required by the governing equations. The radial velocity V is calculated through the continuity equation,

$$V(x,r) = -\frac{1}{r}\int_0^r \tilde{r}\,\frac{\partial U}{\partial x}(\tilde{r},x)\,d\tilde{r}, \tag{4.7}$$

and the eddy viscosity is calculated through the turbulence closure,

$$\nu_T(x,r) = C_\mu\,\frac{k^2}{\varepsilon}\,. \tag{4.8}$$

In the test case of the k–ε–f_P turbulence model, the eddy viscosity is calculated with

$$\nu_T(x,r) = f_P C_\mu\,\frac{k^2}{\varepsilon}\,, \tag{4.9a}$$

$$f_P(x,r) = \frac{2f_0}{1+\sqrt{1+4f_0(f_0-1)\left(\frac{\sigma}{\tilde{\sigma}}\right)^2}}, \tag{4.9b}$$

$$\sigma(x,r) = \frac{k}{\varepsilon}\sqrt{\Phi}, \tag{4.9c}$$

$$\Phi(x,r) = 2\left(\frac{\partial U}{\partial x}\right)^2 + 2\left(\frac{\partial V}{\partial r}\right)^2 + \left(\frac{\partial U}{\partial r} + \frac{\partial V}{\partial x}\right)^2 + 2\left(\frac{V}{r}\right) \tag{4.9d}$$

Source term construction

Substituting the manufactured solutions into the governing equations produces a non-zero residual, because the given functions are not exact solutions to those equations. This residual is added to the right-hand side of the governing equations as a source term, so that the manufactured functions become solutions to the resulting equations. For the k-equation the MMS source term becomes

$$S_k^{\text{MMS}} = \underbrace{\frac{\partial(kU)}{\partial x}}_{\text{ax. conv.}} + \underbrace{\frac{1}{r}\frac{\partial(r\,k\,V)}{\partial r}}_{\text{rad. conv.}} - \underbrace{\frac{1}{r}\frac{\partial}{\partial r}\left(\frac{\nu_T}{\sigma_k}\,r\,\frac{\partial k}{\partial r}\right)}_{\text{diffusion}} - \underbrace{\nu_T\,\Phi}_{\text{production}} + \underbrace{\varepsilon}_{\text{dissipation}}\,, \tag{4.10}$$

where the $\Phi = 2S_{ij}S_{ij}$ is defined as

$$\Phi = 2\left(\frac{\partial U}{\partial x}\right)^2 + 2\left(\frac{\partial V}{\partial r}\right)^2 + \left(\frac{\partial U}{\partial r} + \frac{\partial V}{\partial x}\right)^2 + 2\left(\frac{V}{r}\right)^2. \tag{4.11}$$

The ε-equation source term is constructed similarly:

$$S_\varepsilon^{\text{MMS}} = \frac{\partial(\varepsilon\,U)}{\partial x} + \frac{1}{r}\frac{\partial(r\,\varepsilon\,V)}{\partial r} - \frac{1}{r}\frac{\partial}{\partial r}\left(\frac{\nu_T}{\sigma_\varepsilon}\,r\,\frac{\partial \varepsilon}{\partial r}\right) - C_{1\varepsilon}\,\frac{\varepsilon}{k}\,\nu_T\,\Phi + C_{2\varepsilon}\,\frac{\varepsilon^2}{k}\,. \tag{4.12}$$

For the coupled solver, a source term for the axial momentum equation is also needed:

$$S_U^{\text{MMS}} = \frac{\partial(U^2)}{\partial x} + \frac{1}{r}\frac{\partial(r\,V\,U)}{\partial r} - \frac{1}{r}\frac{\partial}{\partial r}\left(\nu_T\, r\,\frac{\partial U}{\partial r}\right). \tag{4.13}$$

All required expressions are evaluated analytically with MATLAB's Symbolic Math Toolbox and evaluated at the cell centres.

Parameters and test setup

The numerical values of all manufactured-solution coefficients are listed in Table 4.1. The model constants used in both tests are given in Table 4.2. All three tests use the same manufactured solutions and domain length $L = 1$.

Table 4.1: Manufactured-solution coefficients used in the MMS verification.

Variable	ϕ_0	ϕ_x	ϕ_r	ϕ_{xr}	$a_{\phi x}$	$a_{\phi r}$	$a_{\phi xr}$
k	5	0.4	2	0	1	1	1
ε	4	0.5	1	0	1	2	1
U	3	0.2	1	0	1	1	1

Table 4.2: Model constants and solver settings used in the MMS tests.

Parameter	Value
$C_{1\varepsilon}$	1.44
$C_{2\varepsilon}$	1.92
C_μ	0.03
σ_k	1.0
σ_ε	1.3
Domain	$x \in [0,1]$, $r \in [0,1]$ ($L = 1$)
Grid sizes	$N \in \{8,\ 16,\ 32,\ 64,\ 128\}$, $M = N$
Iterative tolerance	10^{-12}
f_P correction	Disabled in tests 1 and 3; enabled in test 2
Sink term S_k	Disabled

Three MMS tests are performed. In the first test, only the k–ε equations are solved. The axial velocity field U is prescribed for the turbulence model from Equation 4.6c, and the radial velocity V is computed from the continuity equation using this prescribed U. The solver therefore marches the k- and ε-equations only, verifying the turbulence model without the wake deficit model. In the second test, the k–ε–f_P equations are solved, in a similar way as in the first test.

In the third test, the full coupled U–k–ε system is solved. The axial velocity is no longer prescribed, and instead it is computed by the wake deficit model and iterated together with the k–ε equations until convergence.

In all three tests, the grid-convergence study is performed on five uniformly refined grids with $N \in \{8,\ 16,\ 32,\ 64,\ 128\}$ and $M = N$. Each refinement step reduces the grid spacing by a factor of two, which ensures a consistent refinement ratio for all grids. The iterative solver residual is set to 10^{-12} for all cases, which is roughly six orders of magnitude below the smallest error observed. This ensures that the iterative error does not influence the grid-convergence results.

Bug detection

During the verification process, the observed order of accuracy was lower than expected and decreased with grid refinement. This made it probable that there was a bug in the model implementation. By repeating the test cases several times, starting with few terms and increasingly activating more terms of the transport equations, the error source could be isolated. It was found that the production term contained a bug due to a mistake in the calculation of the velocity gradients. After correcting the calculation, the grid-convergence tests displayed the expected second-order convergence across all variables. This illustrates the value of MMS. Even though the manufactured solutions have no physical meaning, they can highlight implementation errors that might otherwise remain hidden in tests using analytical solutions where not all terms are activated at the same time.

4.3.1 Standalone k–ε model

In the first MMS test, only the k–ε equations are solved while the axial velocity field is prescribed. The radial velocity is then calculated from the continuity equation using this prescribed velocity field. This setup isolates the turbulence model from the momentum equation, so that any discretisation error can be blamed on the implementation of the k- and ε-equations.

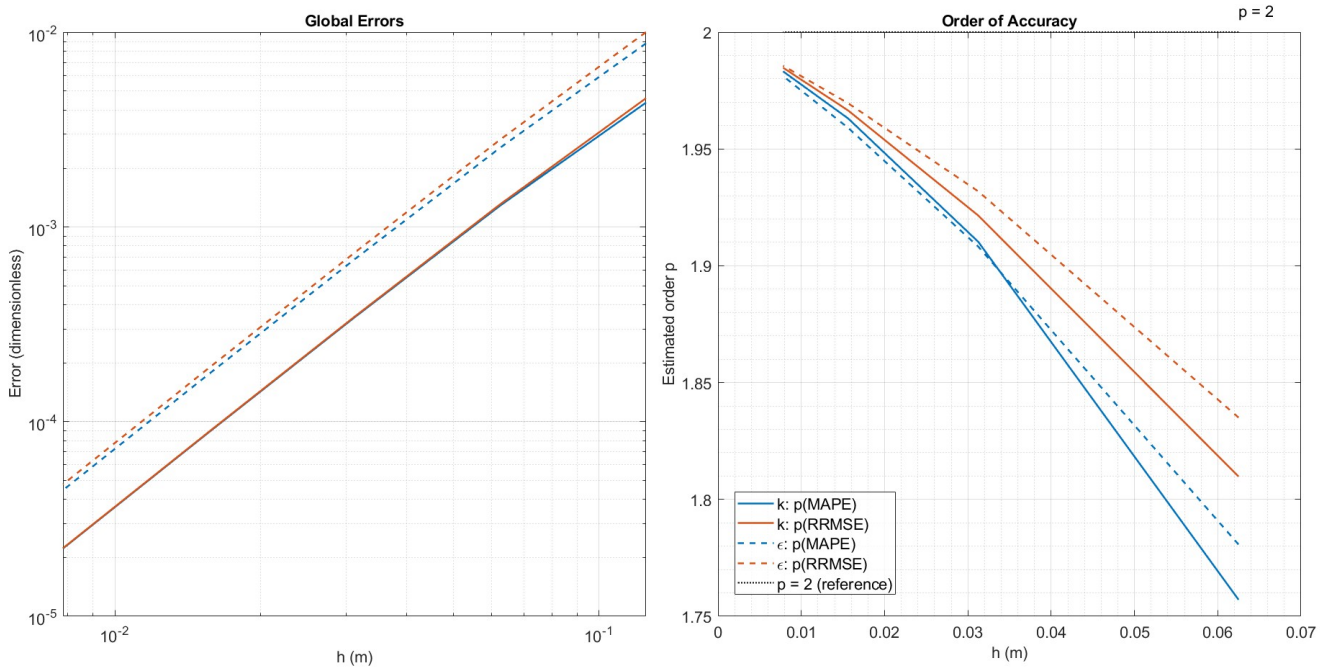

Figure 4.2: Grid-convergence results for the MMS test of the standalone k–ε model with prescribed velocity field. Left: global error metrics as a function of grid spacing h. Right: order of accuracy. Solid lines correspond to k, dashed lines to ε.

The results can be seen in Figure 4.2. The left figure shows the global error metrics as a function of grid spacing on a logarithmic scale. For both k and ε, the MAPE and RRMSE decrease with decreasing h, and the straight lines confirm that all the considered meshes lie within the asymptotic convergence range. The error levels for ε are higher than those for k, which is expected given the stronger nonlinearity of the ε-equation. For k, the MAPE and RRMSE lines nearly coincide, which indicates that over the domain the error of k must be more or less uniform. For ε, a small difference between the two metrics is visible, suggesting that in some regions of the mesh the error in ε is somewhat larger than the average over the domain.

The right figure shows the observed order of accuracy computed between consecutive finer grids. On the finest grids, all four curves approach the theoretical order of $p = 2$. On coarser grids the estimated order decreases to approximately 1.80 at the coarsest grid. This behaviour is expected, since on coarse grids, the higher-order terms in the truncation error function, Equation 4.1, are not negligible, which lowers the observed order. As the grid is refined, these terms vanish, and the leading second-order term becomes dominant and the estimated order converges toward $p = 2$. Both metrics indicate an order of accuracy approaching $p = 2$, confirming that the implementation of the standalone k–ε turbulence model is second-order accurate.

4.3.2 Standalone k–ε–f_P model

In the second test the f_P term is activated. This changes the eddy viscosity to $\nu_T = C_\mu f_P k^2/\varepsilon$. f_P is a function of k, ε and U through the shear parameter σ. This means the MMS source terms for both transport equations must be calculated again with the modified eddy viscosity implemented. The manufactured solutions and all other settings used by the solver remain the same as in the previous test, as listed in Table 4.1 and Table 4.2.

Figure 4.3 shows the results of the second test. The errors and convergence behaviour are the same as those of the standard k–ε in the previous test (Figure 4.2). Again, both k and ε converge at second order. This confirms that the f_P correction and its coupling with the eddy viscosity are implemented correctly.

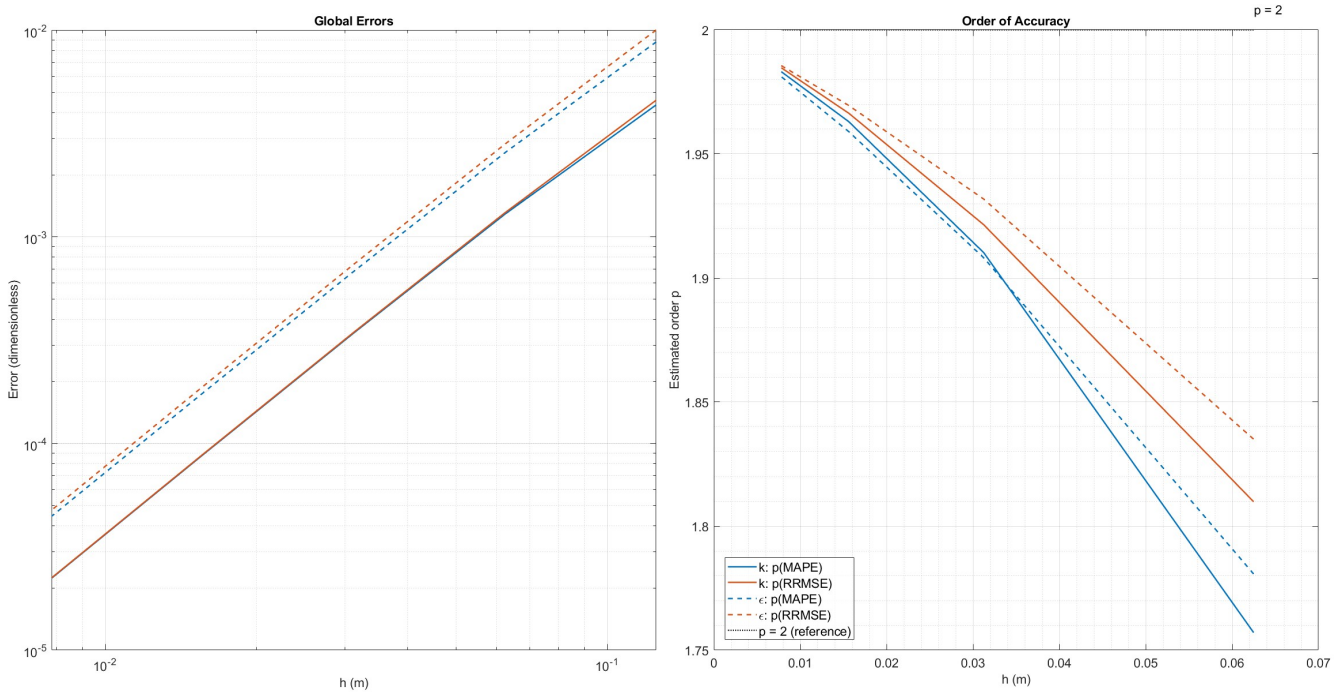

Figure 4.3: Grid-convergence results for the MMS test of the standalone k–ε–f_P model with prescribed velocity field. Left: global error metrics (MAPE and RRMSE) as a function of grid spacing h. Right: estimated order of accuracy. Solid lines correspond to k, dashed lines to ε.

4.3.3 Coupled U–k–ε solver

In the final MMS test, the axial velocity is no longer prescribed in the standalone turbulence model but is computed by the wake deficit model. The wake deficit model is then iterated together with the turbulence model until convergence. This setup tests the complete coupling between the momentum equation and the k–ε model.

This test is carried out in two parts. In the first part, only the axial direction is refined while the radial spacing is kept fixed. In the second part, only the radial direction is refined while the axial spacing is kept fixed. Splitting the refinement study in this way is done because the discretisation of the momentum equation is not uniform in both directions, as described in Section 2.2.4: the axial convection term uses a first-order upwind scheme, while the radial convection and diffusion terms are discretised with central differences. The expected order of accuracy therefore differs between the two directions, and a combined refinement would mix both rates and obscure the underlying convergence behaviour.

The axial refinement study shows an observed order of accuracy close to $p = 1$ for the axial velocity U, which is in agreement with the first-order upwind scheme used in the momentum equation. The corresponding convergence plot is omitted for brevity. Because it adds little beyond confirming the expected first-order behaviour. The radial refinement study, shown in Figure 4.4, is discussed in the remainder of this subsection.

The results of the radial refinement study are shown in Figure 4.4. In the left figure, all three variables show a decrease of the error metrics with decreasing grid spacing, and the almost straight lines on the logarithmic scale imply that the solutions are within the asymptotic convergence range. The axial velocity U reaches the lowest error levels of the three variables, roughly half an order of magnitude below k and ε on each grid. This is expected, since the momentum equation is less stiff than the turbulence-transport equations, because it does not have the nonlinear source terms that are a part of the k–ε model equations. k and ε have comparable errors, with ε's errors being slightly larger, which is consistent with the standalone test.

The right figure shows the observed order of accuracy. The axial velocity matches the theoretical value of $p = 2$ across all grid levels. The observed orders following from RRMSE are slightly lower than the ones following from MAPE, especially for k and ε. This is consistent with the standalone test.

Overall, the error decreases with each refinement and the observed orders on the finest grid pair are consistent with second-order accuracy for all three variables. Together with the standalone test and the axial refinement study, these results confirm that the fully coupled U–k–ε solver is correctly implemented and achieves the formal order of accuracy of the discretisation in each direction.

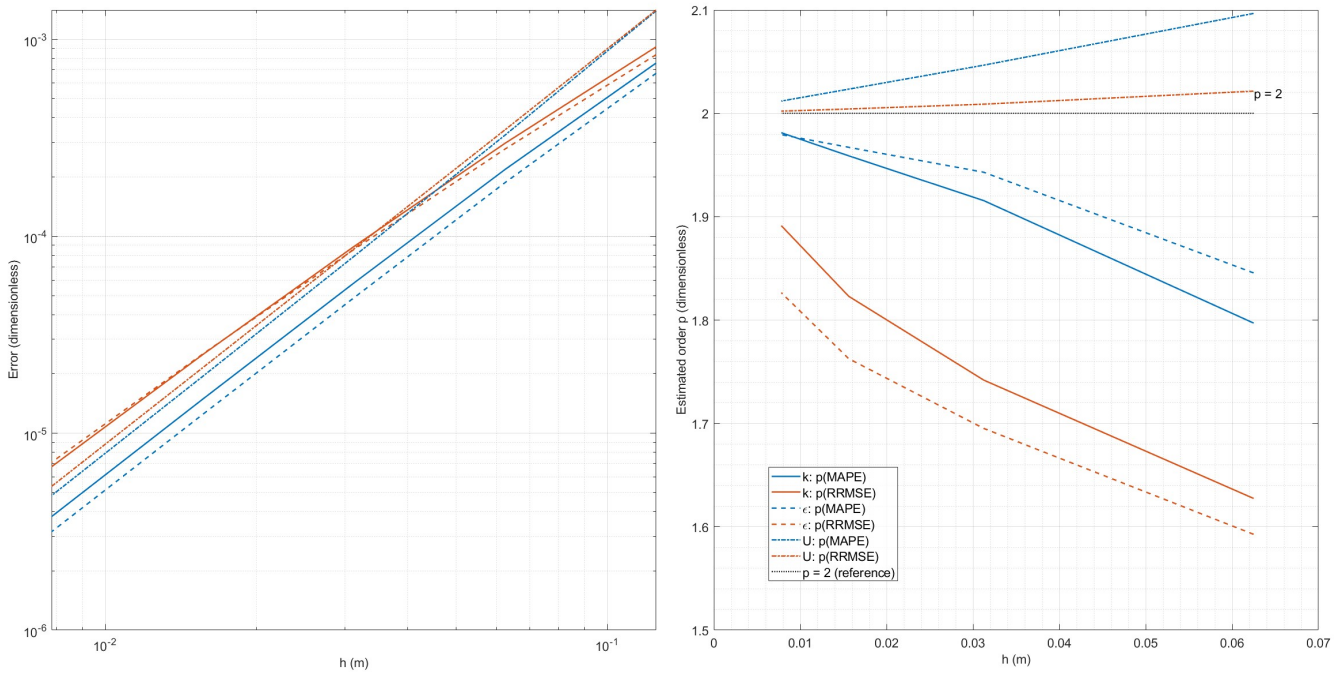

Figure 4.4: Grid-convergence results for the MMS test of the fully coupled U–k–ε solver under radial refinement. Left: global error metrics (MAPE and RRMSE) as a function of grid spacing h. Right: estimated order of accuracy. Solid lines correspond to k, dashed lines to ε, and dash-dotted lines to U. The dotted line marks the reference $p = 2$.

4.4 Turbulent Coflowing Jet

In this section, the test results of simulating a turbulent coflowing jet are discussed. In the previous test cases, verification was done through known analytical solutions. A turbulent coflowing jet has no known analytical solution however. But because a jet develops a self-similar region far downstream, this test is used to verify the solver's ability to capture the correct asymptotic decay and spreading rates of a jet.

4.4.1 Reference experiment

The reference experiment is the axisymmetric turbulent coflowing jet measured by Nickels and Perry [1]. A round jet with nozzle diameter $D = 25.4$ mm is ejected into a uniform background flow with velocity $U_1 = 3.5$ m/s. The turbulence intensity of the background flow is less than $0.6\,\%$, and the ejected flow has a turbulence intensity below $0.5\,\%$ at the nozzle exit. Three velocity ratios $\lambda_J = U_j/U_1 = 2$, 10, and 20 were tested, but in this test case only $\lambda_J = 10$ is considered, corresponding to a jet exit velocity of $U_j = 35$ m/s and a Reynolds number $\mathrm{Re} = U_j D/\nu \approx 59\,300$. $\lambda_J = 2$ is not considered, because this yields a low jet exit velocity and a Reynolds number that is on the low range of a turbulent flow. $\lambda_J = 20$ is also not considered, because this yields a relatively large jet exit velocity compared to the coflow. This is difficult to handle for the model due to its parabolized nature and hence causes stability issues. Therefore, only $\lambda_J = 10$ is considered.

One of a coflowing jet's features is that its flow behaviour becomes self-similar far downstream. The self-similar profile can be characterized a an axial and a radial length scale Pope [19]. Nickels and Perry [1] relates this behaviour using the momentum radius θ as the axial length scale and the jet width Δ as the radial length scale, which are defined as

$$U_1^2\,\theta^2 = \int_0^\infty U\big(U - U_1\big)\,2\pi r\,\mathrm{d}r, \tag{4.14}$$

$$\Delta^2 = \frac{\displaystyle\int_0^\infty r^2\big(U - U_1\big)\,\mathrm{d}r}{\displaystyle\int_0^\infty \big(U - U_1\big)\,\mathrm{d}r}. \tag{4.15}$$

The momentum radius does not change with downstream distance because the momentum flux is conserved. When the local velocity excess ratio $\lambda = U_o/U_1 = (U_c - U_1)/U_1$ and the scaled jet width Δ/θ are plotted against x/θ, the measurements for all three λ_J cases coincide on the same curve. Nickels and Perry [1] show that, at large x/θ, the centreline velocity excess decays with $\lambda \sim (x/\theta)^{-2/3}$ and the jet width grows with $\Delta/\theta \sim (x/\theta)^{1/3}$. A curve fit for the

centreline decay that captures both the near-field and far-field behaviour is given by

$$\lambda = C\,\frac{\left(A_1 + (x/\theta)^2\right)^{1/6}}{x/\theta}\,, \qquad C \approx 2.67,\ A_1 \approx 299. \tag{4.16}$$

For the self-similar velocity profile, all results from the three velocity ratios coincide when plotted as $(U - U_1)/U_o$ against $\eta = r/\Delta$. The experimental profiles are given by the curve fit

$$f(\eta) = \exp\!\left(-0.677\,\eta^2 + 0.364\,\eta^3 - 0.121\,\eta^4\right). \tag{4.17}$$

4.4.2 Numerical setup

The simulation uses flow conditions of the $\lambda_J = 10$ experiment as closely as possible. The nozzle diameter, coflow velocity, and velocity ratio match the experimental values. The initial axial velocity profile is given by a Gaussian distribution superimposed on the background flow:

$$U(r) = U_1 + U_0\,\exp\!\left(-\frac{r^2}{\sigma^2}\right), \tag{4.18}$$

where $U_0 = U_j - U_1 = 31.5$ m/s is the excess velocity and the width parameter $\sigma^2 = (D/2)^2$ is chosen such that the volume flux of the Gaussian profile matches that of a top-hat profile with diameter D. The computational domain extends to $100\,D$ in the axial direction and to $25\,D$ in the radial direction. It is discretised with $N = 1000$ uniformly spaced axial cells and $M = 250$ radial cells. The radial cells are distributed exponentially, such that the cells near the axis of symmetry have the smallest volumes.

The turbulence model uses the standard k–ε constants as given by Pope [19]: $C_{1\varepsilon} = 1.44$, $C_{2\varepsilon} = 1.92$, $C_\mu = 0.09$, $\sigma_k = 1.0$, $\sigma_\varepsilon = 1.3$. The initial turbulent kinetic energy is $k(r) = \frac{3}{2}(\mathrm{TI}\cdot U(r))^2$ with $\mathrm{TI} = 0.5\,\%$, as reported for the coflow in the experiment description. The dissipation rate is estimated using a mixing-length argument with the jet diameter as the integral length scale: $\varepsilon = C_\mu^{3/4}\,k^{3/2}/D$. The initial eddy viscosity is calculated from the eddy viscosity relation $\nu_T = C_\mu\,k^2/\varepsilon$. The f_P correction and the forcing sink term are both disabled in this test case.

4.4.3 Results

Figure 4.5 presents the centreline velocity excess decay and the jet width growth on logarithmic axes, using the momentum radius θ as the axial length scale. The momentum radius computed from the simulated inflow profile is $\theta/D \approx 8.4$.

The figure on the left shows the local velocity excess ratio $\lambda = U_o/U_1$ as a function of x/θ. After the curve stays constant due to the potential core, the curve starts to decay monotonically. At large x/θ, the simulation approaches the $(x/\theta)^{-2/3}$ asymptote, which is the far-field power law derived by Nickels and Perry [1] for the self-similar coflowing jet. In the near field, the initial conditions have a larger influence on the the flow and the flow depends on λ_J. The convergence of the simulation to $-2/3$ slope further downstream x/θ confirms that the solver replicates the correct asymptotic decay behaviour as observed by the experiment. The figure on the right represents the normalised jet width Δ/θ as a function of x/θ. The simulated jet width increases with downstream distance, but does not precisely follow the $(x/\theta)^{1/3}$ power-law trend until only at the end of the domain.

Figure 4.6 shows normalised radial profiles at five downstream locations between $x/D = 100$ and $x/D = 900$. The normalised excess velocity profiles (panel a) collapse across all four locations, which confirms the self-similar behaviour. The simulation overshoots the experimental curve fit of Nickels and Perry [1] (Equation 4.17) for $r/\Delta \lesssim 2.0$, but decays to zero more rapidly near the jet edge. This steeper decay is caused by the low eddy viscosity outside the jet, which reduces radial diffusion at the boundary and underpredicts entrainment between the jet and the coflow.

The normalised turbulent kinetic energy (panel b) peaks at the centreline, plateaus for $r/\Delta \lesssim 0.6$, and then decays. The eddy viscosity (panel c) behaves similarly, dropping to a small plateau minimum value $r/\Delta \gtrsim 2.5$ The dissipation rate (panel d) peaks at a larger r/Δ than k. This reflects the stronger production in the shear layer. All four quantities collapse well across all the axial locations.

The simulation is able to reproduce the most important self-similar features of the coflowing jet, namely the centreline decay and jet width growth that follow power laws, and the radial profiles that reach a self-similar state. Together with the verifcation tests earlier in this chapter, these results confirm that the solver is correctly implemented and that the interactions between convection, diffusion, production, and dissipation are captured accurately.

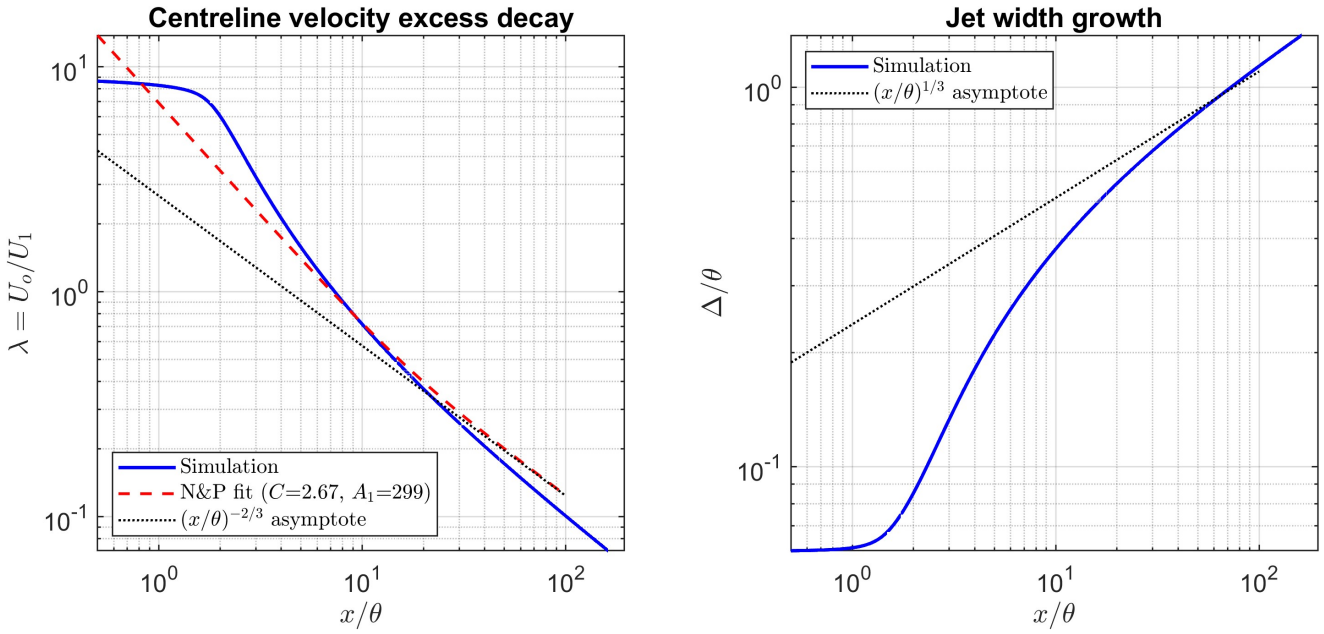

Figure 4.5: Centreline velocity excess decay (left) and jet width growth (right) on logarithmic axes, using the momentum radius θ as the axial length scale. The dashed red line shows the curve fit of Nickels and Perry [1] (Equation 4.16). The dotted lines indicate the asymptotic power laws for a self-preserving coflowing jet.

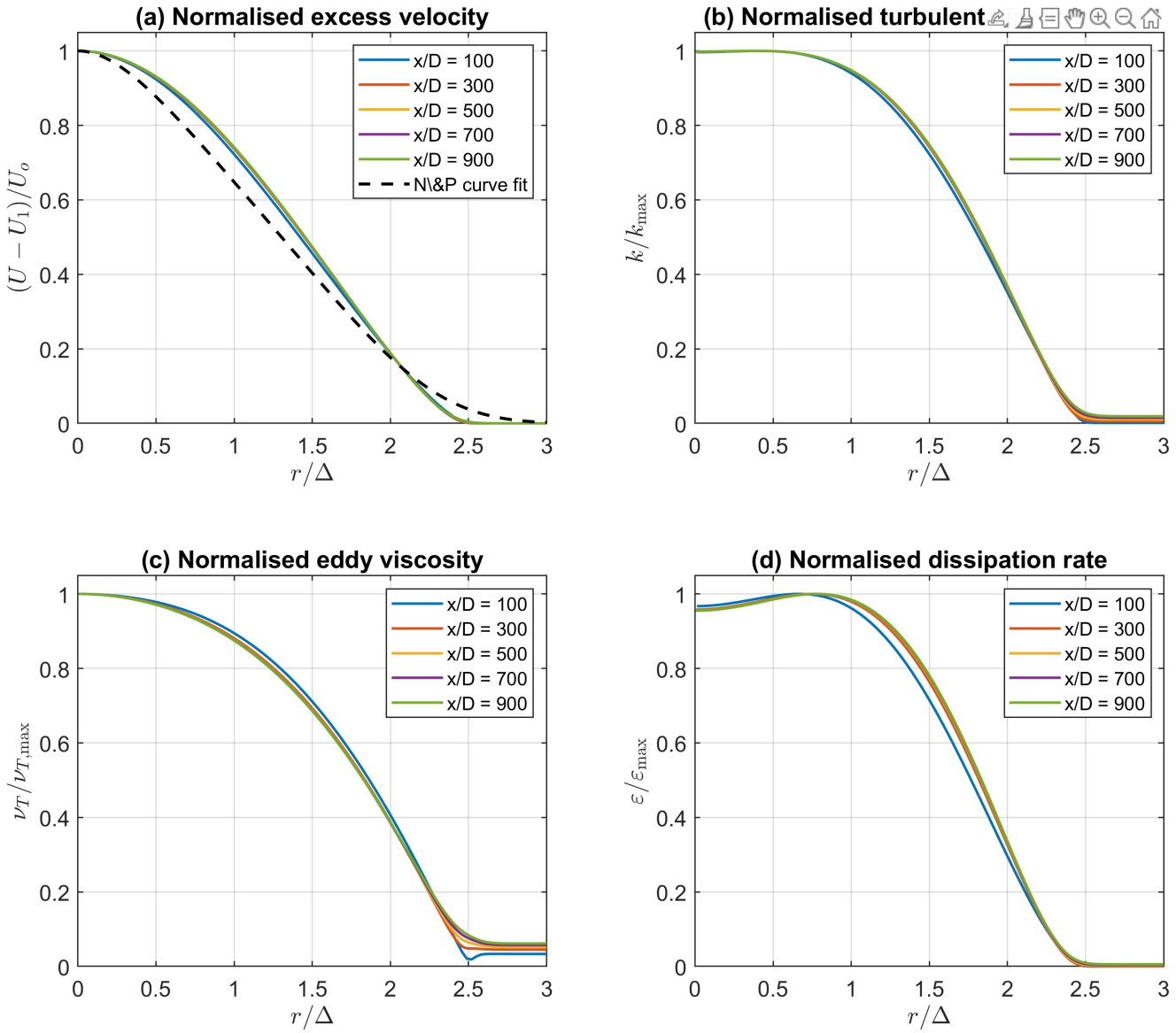

Figure 4.6: Self-similar profiles at four downstream locations between $x/D = 45$ and $x/D = 90$. (a) Normalised excess velocity $(U - U_1)/U_o$ with the curve fit of Nickels and Perry [1] (Equation 4.17, dashed). (b) Normalised turbulent kinetic energy $k/k_{\max}$. (c) Normalised eddy viscosity $\nu_T/\nu_{T,\max}$. (d) Normalised dissipation rate $\varepsilon/\varepsilon_{\max}$.

5 Results and Discussion

This chapter presents the validation of the coupled FAWM solver against high-fidelity LES data. Section 5.1 presents the four reference LES cases that are used, which span a range of wind speeds and thrust settings. Section 5.2 discusses numerical stability problems that occurred during the simulations. The root cause of these instabilities is identified, after which two solutions are proposed. The subsequent two sections present the results obtained from two model formulations. Section 5.3 shows the results of the original model, where most cases diverged or produced nonphysical results. Section 5.4 shows the results from the modified formulation of the production term, in which $\frac{\partial V}{\partial x}$ is neglected in the computation of the strain-rate invariant. This modification led to more stable simulations and a better agreement with the LES data.

5.1 Reference Large Eddy Simulations

In this section the LES data that was used for validation of the coupled solver is presented. This data was generated by the finite volume library YALES2 Moureau and Lartigue [18]. It uses fourth-order numerical schemes in space and time to solve multi-physics problem on unstructured meshes. The sub-grid scale (SGS) stresses are modeled using the Dynamic Smagorinsky formulation Lilly [60].

Four reference cases are available for validation and they are shown in Figure 5.1. The I_{REF} that characterises each case is based on the IEC Standard 61400-1's definition of turbulence intensity International Electrotechnical Commission [33]:

$$TI = \frac{\sigma_1}{U_\infty}, \quad \sigma_1 = I_{\text{REF}}(0.75\,U_\infty + 5.6), \tag{5.1}$$

where σ_1 is the standard deviation of the velocity fluctuations in the main flow direction.

Configuration 1 ($U_\infty = 4.0\,$m/s, $I_{\text{REF}} = 0.16$) represents a case where the turbine operates below the rated wind speed with a high thrust setting. Configurations 2 ($U_\infty = 11.4\,$m/s, $I_{\text{REF}} = 0.12$) and 3 ($U_\infty = 11.4\,$m/s, $I_{\text{REF}} = 0.16$) correspond to a turbine that operates close to the rated wind speed with a medium thrust setting. Finally, configuration 4 ($U_\infty = 19.25\,$m/s, $I_{\text{REF}} = 0.16$) corresponds to a high wind speed with a low thrust setting. Since configurations 2 and 3 share the same inflow velocity but differ in turbulence intensity, they make it possible to assess the influence of the inlet turbulence level on the wake development.

In the LE simulations, the rotor of the DTU-10MW reference wind turbine Bak et al. [17] is represented by the Actuator Line Method (ALM) Sørensen and Shen [61]. The ALM is applied without any of the classical corrections that are typically used in the Blade Element Method. For example, tip-loss or rotational corrections. Because the actuator disk formulation used in the FAWM simulations does not include cone or tilt angles, both are set to zero in all LES runs, despite the fact that their design values are non-zero. The design data is used to prescribe a rotor speed and pitch angle for each case. assuming the blades are infinitely rigid. The inflow conditions are made axisymmetric by setting a uniform flow at the inlet and prescribing a synthetic homogeneous and isotropic turbulence.

The LES data was originally collected for the study of Warncke et al. [2], where the setup description is given in more detail. The computational domain and the corresponding cell size distribution are shown in Figure 5.1. The mesh has over 230 milltion cells and is most refined in the close to rotor and its near wake, $-4D < x < 10D$, $0 < r < 4D$. Upstream, downstream and outboard the mesh becomes coarser, and becomes significantly coarser beyond $x = 20D$. At the end of the domain, some viscosity is artificially added. This is necessary to guarantee numerical stability, by preventing reflections at the domain's boundaries.

There was a complication with the LES data base. As said before the data was initially gathered for Warncke et al. [2]. After this study, the meshes for configuration 2-4 were removed to save storage space. This was done under the assumption that all meshes were identical. However, it turned out YALES2 applied some post-processing to the meshes, making them slightly different for each case. This has resulted in some artifacts that appear in the results for configurations 2-4, as can be seen from Figure 5.2.

The blade loads are gathered from the LES data in order to determine the correct actuator disk parameters to be used in the FAWM simulations. This is done in the following two steps. First, the simulation is run for a duration of $T_1 = T_{ft}$, where T_{ft} denotes the flow-through time of the injected turbulence fields. This allows the turbine wake to develop and become statistically stationary. Second, the time history of the blade loads is recorded for as long as $T_2 = 2\,T_{ft}$. These loads are then averaged in time per blade and spanwise element. The axial forcing strengths of the actuator disk rings

Config. #	U_∞ [m/s]	I_{REF}
1	4.0	0.16
2	11.4	0.12
3	11.4	0.16
4	19.25	0.16

Table 5.1: Operating conditions of the four configurations simulated with the YALES2 library Warncke et al. [2].

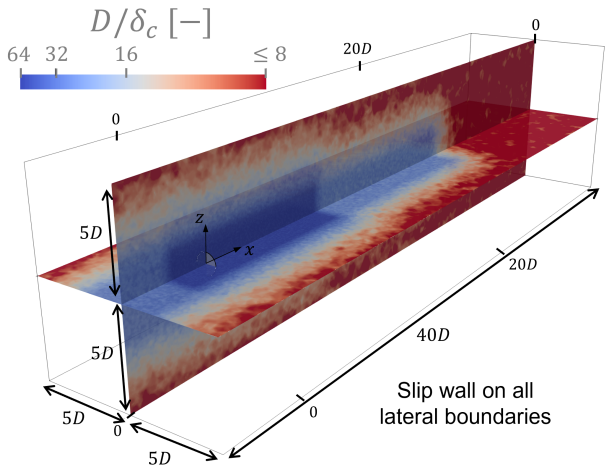

Figure 5.1: Domain size and cell size δ_c distribution used in all configurations from Figure 5.1 Warncke et al. [2].

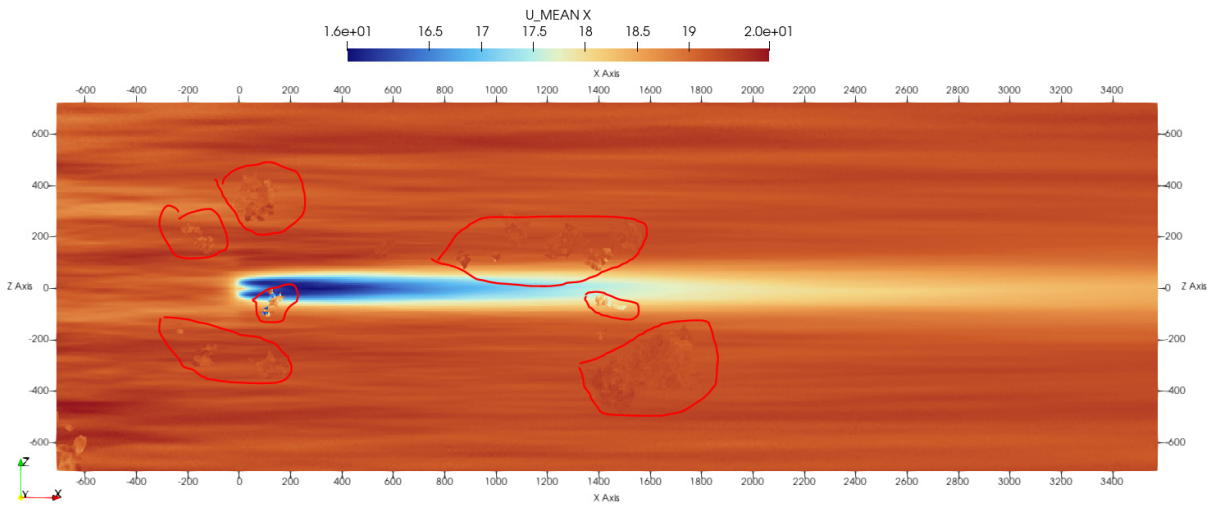

Figure 5.2: Mesh-induced artefacts observed in the LES data for configurations 2–4, caused by the unintended loss of the original YALES2 meshes.

$F_{x,i}$ are then calculated with

$$F_{x,i} = \frac{1}{\rho}\left(\frac{\sum_{j=1,2,3} F_{i,j}}{\pi\left(r_{i+1}^2 - r_i^2\right)} - \frac{\sum_{j=1,2,3} F_{i-1,j}}{\pi\left(r_i^2 - r_{i-1}^2\right)}\right). \tag{5.2}$$

These force densities are used as the vortex ring strengths used by the FAWM solver to reconstruct part of the pressure term as explained in Section 2.2.3. The force distributions for all four cases can be seen in Figure 5.3.

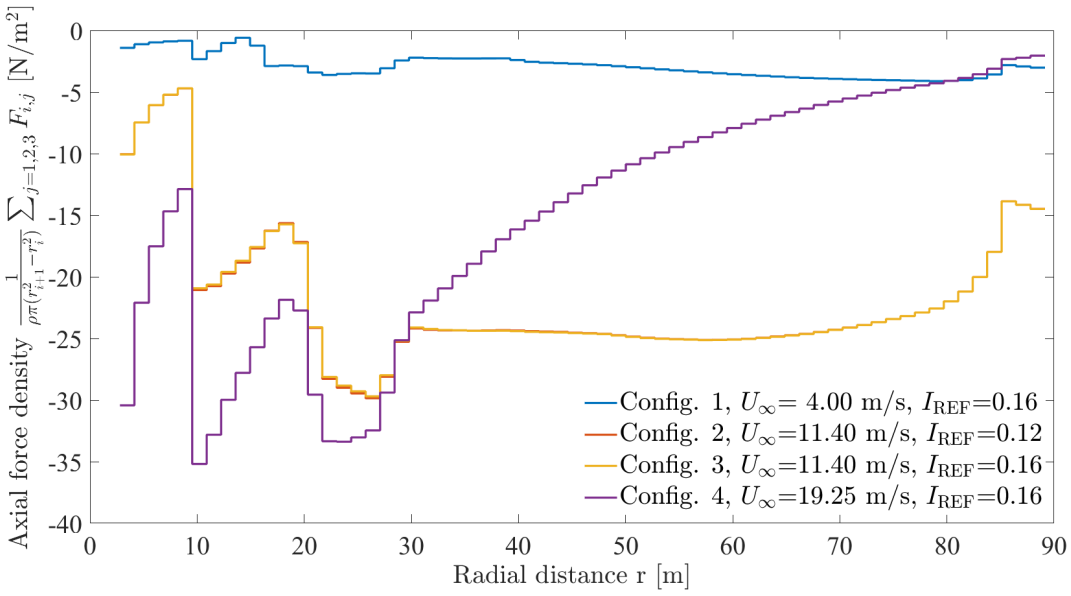

Figure 5.3: Piecewise constant axial force densities derived from the time-averaged blade loads of the YALES2 simulations for all four configurations Warncke et al. [2].

The inflow conditions of k and ε are determined separately for each FAWM simulation. They are chosen such to reproduce the TKE at $x_1 = -0.5D$ upstream of the actuator disk as predicted by the LES, to ensure a close match between the LES and FAWM data. The ε to be matched is taken as average production of TKE upstream of the rotor, according to the assumption that the production and dissipation of k are in equilibrium. To determine the right inflow conditions of k and ε at $x_1 = -10D$ such that they achieve approximately the correct values at $x_1 = -0.5D$, it is assumed that the only term acting in this region is ε. This significantly simplifies the model equations and together with the homogeneity of the inflow conditions allows for them to be solved analytically:

$$\text{Decay equations:} \qquad U_0 \frac{\mathrm{d}k}{\mathrm{d}x} = -\varepsilon, \quad U_0 \frac{\mathrm{d}\varepsilon}{\mathrm{d}x} = -C_{2\varepsilon}\frac{\varepsilon^2}{k}, \tag{5.3a}$$

$$\text{Solution with initial point } x_1: \qquad k(x) = \left[k(x_1)^{1-C_{2\varepsilon}} + \frac{(C_{2\varepsilon}-1)\,\varepsilon(x_1)}{U_0\,k(x_1)^{C_{2\varepsilon}}}(x - x_1)\right]^{\frac{1}{1-C_{2\varepsilon}}}, \tag{5.3b}$$

$$\varepsilon(x) = \varepsilon(x_1)\left(\frac{k(x)}{k(x_1)}\right)^{C_{2\varepsilon}}. \tag{5.3c}$$

The same error metrics as in the previous chapter (Section 4.1) are used to compare the predictions of the FAWM solver with YALES2: the Mean Absolute Percentage Error (MAPE) and the Relative Root Mean Square Error (RRMSE). They are defined as follows:

$$\begin{aligned} \text{MAPE} &= \frac{1}{n}\sum_{i=1}^{n}\left|\frac{\phi_{Y2,i} - \phi_{F,i}}{\phi_{Y2,i}}\right|, \\ \text{RRMSE} &= \frac{\sqrt{\sum_{i=1}^{n}\left(\phi_{Y2,i} - \phi_{F,i}\right)^2}}{\sum_{i=1}^{n}|\phi_{Y2,i}|}. \end{aligned} \tag{5.4}$$

To distinguish between the near and far wake, two masks are defined on which the error metrics are calculated:

$$\mathcal{M}_{\text{near}} = (|r| \leq D) \ \wedge \ (x \geq -2D) \ \wedge \ (x < 3D) \ \wedge \ \left(\left| \frac{U_F - U_\infty}{U_\infty} \right| \geq 0.01 \right), \tag{5.5}$$

$$\mathcal{M}_{\text{far}} = (|r| \leq D) \ \wedge \ (x \geq 3D) \ \wedge \ (x < 10D) \ \wedge \ \left(\left| \frac{U_F - U_\infty}{U_\infty} \right| \geq 0.01 \right). \tag{5.6}$$

The near-wake mask lays around the actuator disk ($-2D \leq x < 3D$) and the far-wake extends beyond this region ($3D \leq x < 10D$) . A minimum velocity deficit is used in order to prevent data points from the free-stream to obscure the error metrics calculations.

The comparison between the FAWM and LES data is done as follows. First, the error metrics for the turbulent kinetic energy are first presented in a table. Then contour plots of each flow variable (U, V, k, ν_T and ε) are shown, together with radial profiles for U, V and k. The contourplots of U, V and k are accompanied with contourplots of the LES data, while these are not included for ν_T and ε. The SGS eddy viscosity only represent the effect of the unresolved small scale eddies below the filter width and not the large eddies. Therefore, it has a much smaller value than FAWM's eddy viscosity, which represents the entire range of eddies. Similarly, the SGS dissipation represents the energy transfer from resolved eddies to the unresolved eddies, which depends on the filter width and therefore changes with the mesh resolution. This makes it impossible to compare with the FAWM dissipation rate.

5.2 Stability of the Coupled Solver

This section shows numerical stability issues that occurred during the simulations of the validation cases by the coupled FAWM solver. This section is organized as follows. Firstly, a test matrix of all simulated cases is presented in Section 5.2.1. Secondly, a possible cause for the instability is searched for in Section 5.2.2. And finally, two solutions are discussed in Section 5.2.3.

5.2.1 Observed Instabilities

The coupled solver is used for all four LES cases using each of the three turbulence models, resulting in a total of twelve simulations. In seven of those cases, the simulation diverges in the region right before or right after the actuator disk. And in some of the cases that do converge, the values of k and ν_T explode to nonphysical values. An overview of the test matrix is provided in Table 5.2, where converged simulations are marked in green and divergent ones in red.

Because of the numerical instabilities, slight variations of the model setup are tested. The original setup is labeled as "Original ($\partial V/\partial x$ incl.)" in Table 5.2. The first variation includes a change in the force field used in the axial momentum equation. The original loading results in some sharp spikes in the force field. Therefore, the original loadings are replaced by a smoother loading with an identical total force, in order to get rid of the spikes. This variation is labeled as "Original (Smooth Loading)" in Table 5.2. The second variation excludes the velocity gradient $\frac{\partial V}{\partial x}$ from the calculation of the production term, while retaining the original loading. This variation is is labeled as "Modified ($\partial V/\partial x$ excl.)" in Table 5.2.

Table 5.2: Test matrices for the validation cases. From left to right: original formulation with the full production term using the LES-derived loading, original formulation with a smoothed loading distribution, and modified formulation with $\partial V/\partial x$ excluded from the production term. Green indicates convergence; red indicates divergence.

	Original ($\partial V/\partial x$ incl.)			**Original (Smooth Loading)**			**Modified ($\partial V/\partial x$ excl.)**		
	Std.	S_k	f_P	**Std.**	S_k	f_P	**Std.**	S_k	f_P
Config. 1									
Config. 2									
Config. 3									
Config. 4									

5.2.2 Root Cause Analysis

To determine the source of the instabilities, the size of the terms in the solver were examined. From this followed that the production term exploded in the region of divergence. The ratio P_k/ε grew to a magnitude of $\mathcal{O}(10^{12})$ at the axial location of the actuator disk, which is of course physically impossible. To research the cause of the overproduction, all contributions to the production were examined. The production of turbulent kinetic energy is given by $P_k = \nu_T \Phi$, where

the strain-rate invariant $\Phi = 2S_{ij}S_{ij}$ consists of five velocity-gradient components:

$$\Phi = 2\left(\frac{\partial U}{\partial x}\right)^2 + 2\left(\frac{\partial V}{\partial r}\right)^2 + \left(\frac{\partial U}{\partial r} + \frac{\partial V}{\partial x}\right)^2 + 2\left(\frac{V}{r}\right)^2. \tag{5.7}$$

Figure 5.4 compares the five velocity-gradient components computed by the FAWM solver with the corresponding LES values at the rotor plane ($x/D = 0$) for configuration 2. The components $\partial U/\partial x$, $\partial V/\partial r$, $\partial U/\partial r$ and V/r are of comparable magnitude between the two approaches. However, the $\partial V/\partial x$ term from the FAWM result is approximately two orders of magnitude larger than its LES counterpart. This suggests an overestimation of the axial gradient of the radial velocity by the FAWM solver.

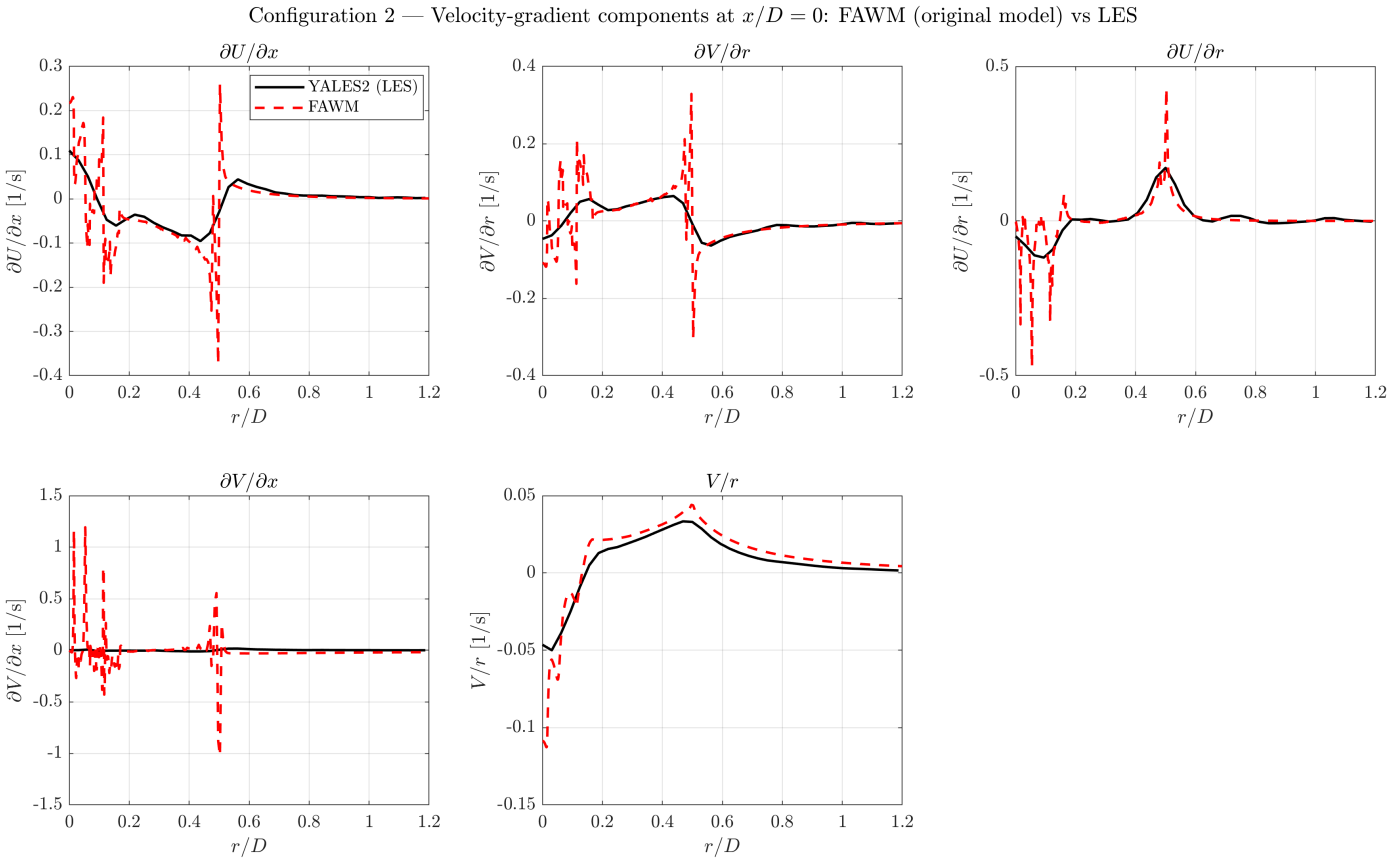

Figure 5.4: Velocity-gradient components entering the production term at $x/D = 0$ for configuration 2: FAWM (original model) versus LES. All components except $\partial V/\partial x$ are of comparable magnitude between the two approaches.

The cause of the overestimation of $\partial V/\partial x$ can be explained through the following. In the axisymmetric solver, the radial velocity is not solved for directly by a transport equation but is derived from the axial velocity using the continuity equation,

$$\frac{\partial U}{\partial x} + \frac{1}{r}\frac{\partial (rV)}{\partial r} = 0, \tag{5.8}$$

which yields

$$V(r,x) = -\frac{1}{r}\int_0^r \frac{\partial U}{\partial x}\,\tilde{r}\,\mathrm{d}\tilde{r}. \tag{5.9}$$

Differentiating with respect to x gives

$$\frac{\partial V}{\partial x} = -\frac{1}{r}\int_0^r \frac{\partial^2 U}{\partial x^2}\,\tilde{r}\,\mathrm{d}\tilde{r}, \tag{5.10}$$

which shows that $\partial V/\partial x$ depends on the second axial derivative of U, i.e. $\partial^2 U/\partial x^2$. Any spikes in U_{xx} is therefore transferred over to $\partial V/\partial x$.

Now the axial momentum equations can be rearranged as follows:

$$\frac{\partial U}{\partial x} = \frac{1}{U}\left(\frac{1}{r}\frac{\partial}{\partial r}\left(\nu_T \frac{\partial U}{\partial r}\right) + F - V\frac{\partial U}{\partial r}\right), \tag{5.11}$$

which shows that $\partial U/\partial x$ is depended on the force term F. This means that the second derivative $\partial^2 U/\partial x^2$ depends on $\partial F/\partial x$. If the forcing contains irregularities, these will propagate to the axial velocity and the axial gradient of the radial velocity through Equation 5.10. The complete chain can be summarized as

$$\text{Sharp } F \longrightarrow \text{Large } \frac{\partial U}{\partial x} \longrightarrow \text{Large } \frac{\partial^2 U}{\partial x^2} \xrightarrow{\text{continuity}} \text{Large } \frac{\partial V}{\partial x} \longrightarrow P_k \gg \varepsilon \longrightarrow \text{Divergence.} \tag{5.12}$$

The actuator disk loading resulting from the LES data is divided into 64 rings, which causes a strong variation in the radial direction next to the sharp gradients in the axial direction. The parabolized FAWM model neglects axial diffusion, while this term would normally smoothen sharp gradients in a fully elliptic RANS solver. The remaining radial diffusion is not enough to dampen large gradients, so any irregularities persist and amplify in the solution. In Section 5.3.2, figures of the k field are shown. Figure 5.6 makes it clearly visible that the the standard and S_k model produce nonphysical behaviour, since k is being produced outside of the wake and above physical levels.

5.2.3 Remedial Measures

To solve the instabilities, two solutions were attempted.

Smoothing the actuator disk forcing

First the original irregular loading was replaced by a smooth loading. The smooth loading had an elliptical distribution while conserving the total actuator disk force. This smoothens the forcing term in radial direction, but does nothing to smoothen the axial variations. Using the smooth loading distribution, the solver still converged and diverged in exactly the same pattern for all simulations, as shown in Table 5.2. This suggests that smoothening the radial variation alone is not enough and that the sharp axial gradients alone are enough to cause instabilities. Therefore, this solution was abandoned.

Removing $\partial V/\partial x$ from the production term

During the second attempt the velocity gradient $\partial V/\partial x$ was neglected in the calculation of the strain-rate invariant. As can be seen from Table 5.2, this yielded a better numerical stability. Only one simulation did not converge, the k–ε–f_P model in configuration 1. This is explained by the fact that configuration 1 has the largest thrust setting and thus also has the largest velocity gradients. The f_P factor reduces the eddy viscosity in regions of large shear to keep P_k/ε in balance, while a large eddy viscosity is necessary to smoothen the large gradients in these regions. Therefore the combination of large thrust coefficient with the k–ε–f_P model increases the chance of divergence.

In the next section, the results obtained from the original model with the original loading is presented. In the section thereafter, the results are presented that were obtained from the modified model with $\frac{\partial V}{\partial r}$ neglected in the production term.

5.3 Results From Original Model with $\frac{\partial V}{\partial x}$ Included

In this section, result from the original model are presented. Only five of the 12 simulations converged. The standard k–ε and k–ε–S_k models converge for configurations 3 and 4, and the k–ε–f_P model converges for configuration 3 only. No model converges for configuration 1, which corresponds to the highest thrust coefficient. All error metric tables and contourplots are also shown in Appendix A and Appendix B.

5.3.1 Axial Velocity

The error metrics for the combined near- and far-wake are shown in Table 5.3. The standard k–ε model converged in three configurations. Both MAPE and RRMSE values increase with decreasing wind speed and increasing thrust coefficient.

In configuration 3, the k–ε–S_k model has a MAPE of 9.1%, which is exactly the same as the standard model. The k–ε–f_P model's error metrics are both about a third lower than the other two closures. Breaking these down by wake region (see Appendix A), the near-wake MAPE is 9.5% for the standard and k–ε–S_k models versus 4.5% for k–ε–f_P, while the difference in the far wake becomes smaller, with MAPEs of 8.9% versus 7.7%.

For configuration 4 only the standard and k–ε–S_k models converged and both error metrics are almost identical. The standard model has a MAPE of 2.2% and the k–ε–S_k model 2.1% in configuration. Their RRMSEs are 3.3% and 3.2%.

Table 5.3: Full-wake error metrics for the axial velocity U, original model (with $\frac{\partial V}{\partial x}$ included). Dashes indicate non-converged cases.

(a) MAPE [%]

Config.	Std. k–ε	k–ε–S_k	k–ε–f_P
1	–	–	–
2	–	–	–
3	9.14	9.14	6.34
4	2.24	2.13	–

(b) RRMSE [%]

Config.	Std. k–ε	k–ε–S_k	k–ε–f_P
1	–	–	–
2	–	–	–
3	12.91	12.91	8.65
4	3.34	3.17	–

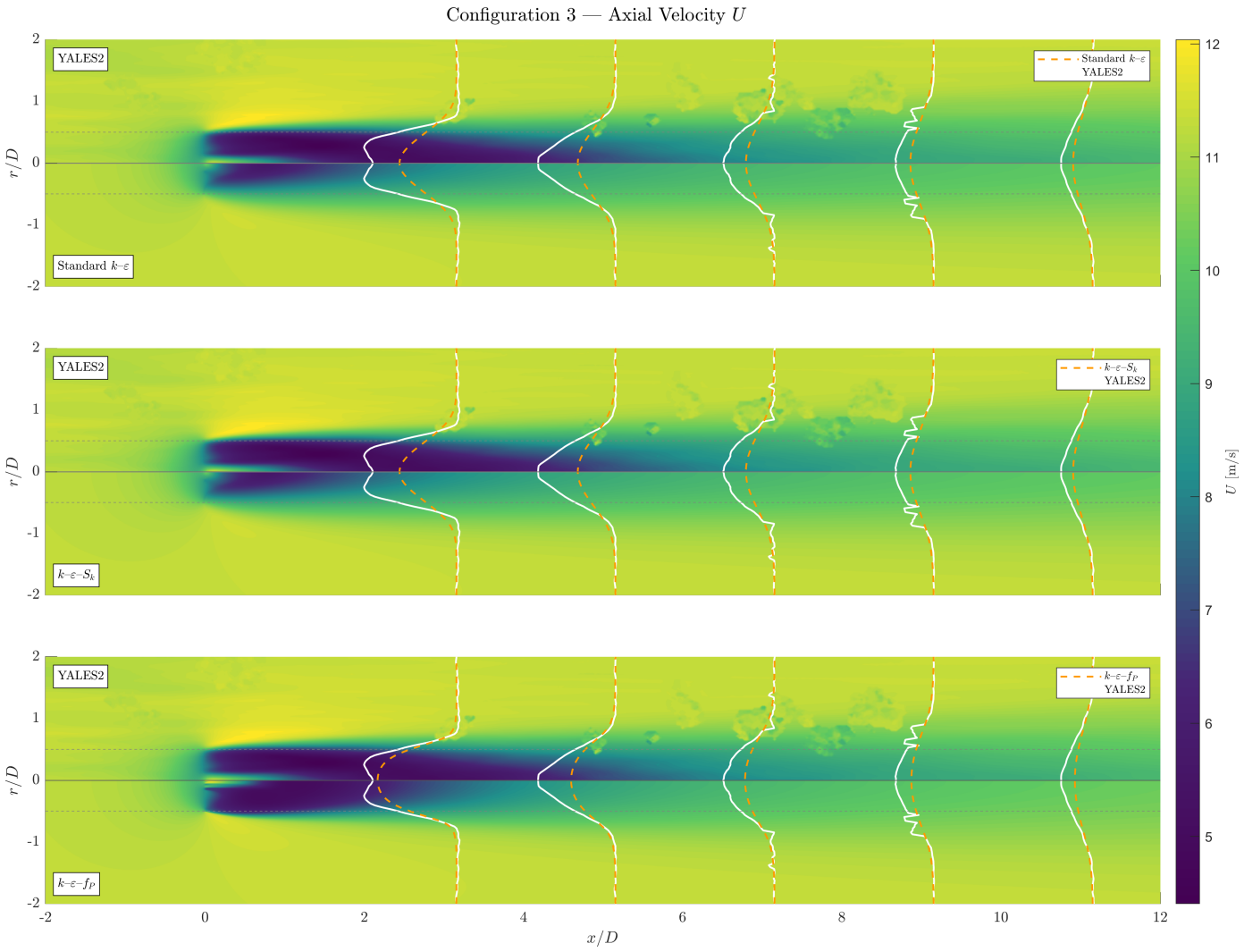

Figure 5.5: Axial velocity U for configuration 3, original model ($\frac{\partial V}{\partial x}$ included). Upper half: YALES2 LES; lower half: FAWM. Rows from top to bottom: standard k–ε, k–ε–S_k, k–ε–f_P. Radial profiles at $x/D = 2, 4, 6, 8, 10$ are overlaid (solid: YALES2, dashed: FAWM).

The contour plots for configuration 3 are shown in Figure 5.5. The standard and k–ε–S_k models produce nearly identical wake shapes. Both underpredict the velocity deficit in the near wake relative to the LES, and the radial profiles show that the FAWM wake recovers faster than the LES wake. The k–ε–f_P model preserves a deeper and wider velocity deficit, particularly in the region between $x/D = 0$ and $x/D = 4$, where the dashed FAWM profiles are closer to the solid LES profiles. Further downstream, the three models converge and the differences between them become smaller. The remaining configurations are shown in Appendix B.

5.3.2 Turbulent Kinetic Energy

The full-wake error metrics for the turbulent kinetic energy k are presented in Table 5.4. They have substantially larger error metrics, which also vary strongly between configurations and turbulence closures.

Table 5.4: Full-wake error metrics for the turbulent kinetic energy k, original model (with $\frac{\partial V}{\partial x}$ included). Dashes indicate non-converged cases.

(a) MAPE [%]

Config.	Std. k–ε	k–ε–S_k	k–ε–f_P
1	–	–	–
2	–	–	–
3	1063.25	1223.31	99.94
4	78.91	74.63	–

(b) RRMSE [%]

Config.	Std. k–ε	k–ε–S_k	k–ε–f_P
1	–	–	–
2	–	–	–
3	3123.02	8544.15	117.63
4	87.46	83.13	–

It can be seen that the standard model and model with S_k have ridiculous large error metric for config 3. From the contourplots it can be seen that k explodes at the actuator disk, after which k slowly dissipates. There is also a very large difference between MAPE and RRMSE for both models, which is caused by the fact that the largest overprediction is in the near-wake. It is remarkable that these large overpredictions only occur for config 3, even though all other simulations also have large metrics. For configuration 3, the k–ε–f_P model has a relatively low error metric.

In Figure 5.6 the contour plots for configuration 3 are shown. They make the scale of the overprediction visible. For the standard and k–ε–S_k models, k in the region downstream of the rotor is in the order of 10^3, while the LES case has an approximate maximum of 4 $\mathrm{m}^2/\mathrm{s}^2$. Both models produce the same result. The third model k–ε–f_P performs much better, since the excessive production is dampened by the f_P correction. But is still overpredicting k across the entire wake and by a large margin.

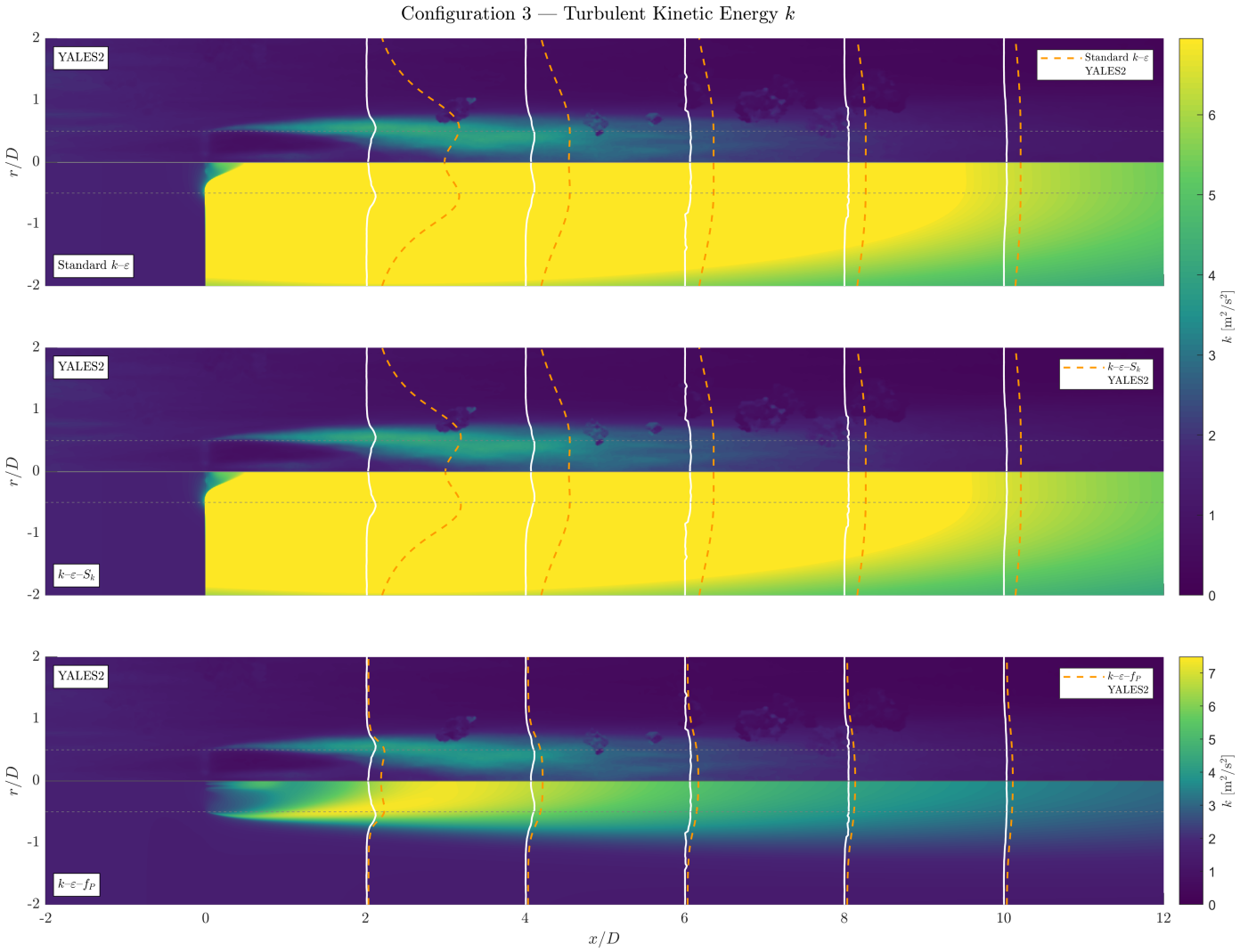

Figure 5.6: Turbulent kinetic energy k for configuration 3, original model ($\frac{\partial V}{\partial x}$ included). Upper half: YALES2 LES; lower half: FAWM. Rows from top to bottom: standard k–ε, k–ε–S_k, k–ε–f_P. Note the different colourbar scales between the models.

5.3.3 Radial Velocity Near the Actuator Disk

Figure 5.6 and Figure 5.9 show a sudden increase of k and ε at the axial location of the actuator disk for the standard k–ε and k–ε–S_k models. As explained in Section 5.2.2, this is caused by an overestimation of the production term, due to the $\frac{\partial V}{\partial x}$ contribution to the strain-rate invariant. Figure 5.7 shows radial profiles of the radial velocity at three locations close to the actuator disk for configuration 3, $x/D = -0.1$, 0.0 and $+0.1$. The FAWM models predict a much larger change in V across the actuator disk than YALES2. They also predict a higher radial velocity at larger radial distances. This increase in V is caused by the blockage of the actuator disk, which locally decreases U and forces the flow radially outward. In the parabolic formulation, there is no axial diffusion to smoothen large gradients in the streamwise direction, so the second axial derivative $\frac{\partial^2 U}{\partial x^2}$ becomes very large at the disk. Since $\frac{\partial V}{\partial x}$ depends on $\frac{\partial^2 U}{\partial x^2}$ through the continuity equation (Equation 5.10), it blows up as well, and with it the production term.

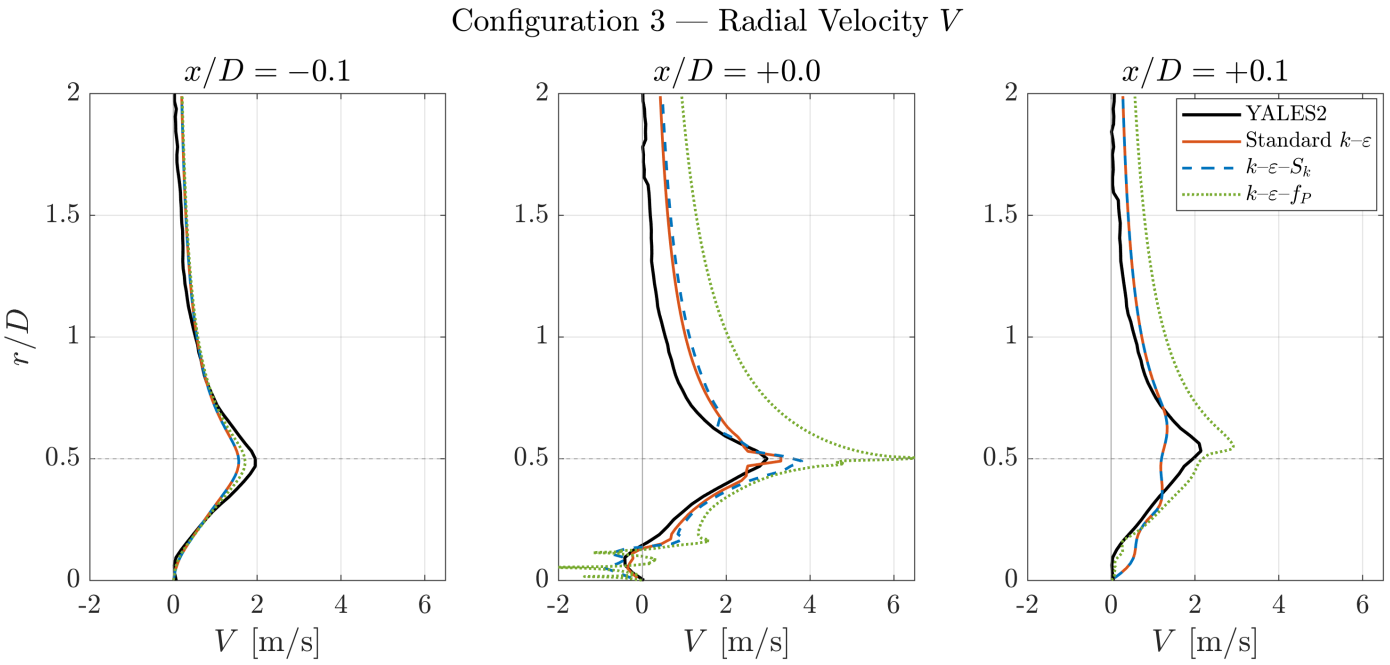

Figure 5.7: Radial profiles of the radial velocity V at $x/D = -0.1$, 0.0 and $+0.1$ for configuration 3, original model ($\frac{\partial V}{\partial x}$ included). The FAWM models predict a much larger step change in V across the actuator disk than YALES2. This causes overproduction of k at the x-coordinate of the AD.

5.3.4 Eddy Viscosity and Dissipation Rate

There is no relevant LES reference data available for the eddy viscosity ν_T or the dissipation rate ε. Therefore, there is no error metric table shown here and the contourplots are only compared to each other. This subsection only disscuses configuration 3, since that is the only configuration for which all three converged. The other contourplots are shown in Appendix B.

For the eddy viscosity the contour plots can be seen in Figure 5.8. The standard and k–ε–S_k models are identical. Just as for k, ν_T also explodes beyond the actuator disk, but only in the outboard region. Here ν_T reaches a maximum value in the order of 10^2. The k–ε–f_P model has an increased value in the inboard region of the near-wake.

The dissipation rate contours are shown in Figure 5.9. The difference between the models is large. Again the plots of the standard and k–ε–S_k models are oversaturated since they have nonphysical large values, with a peak in the order of 10^3, similar as k. The third model k–ε–S_k shows more moderate values, with the dissipation rate being produced in the shear layer which is then advected downstream and diffused throughout the wake.

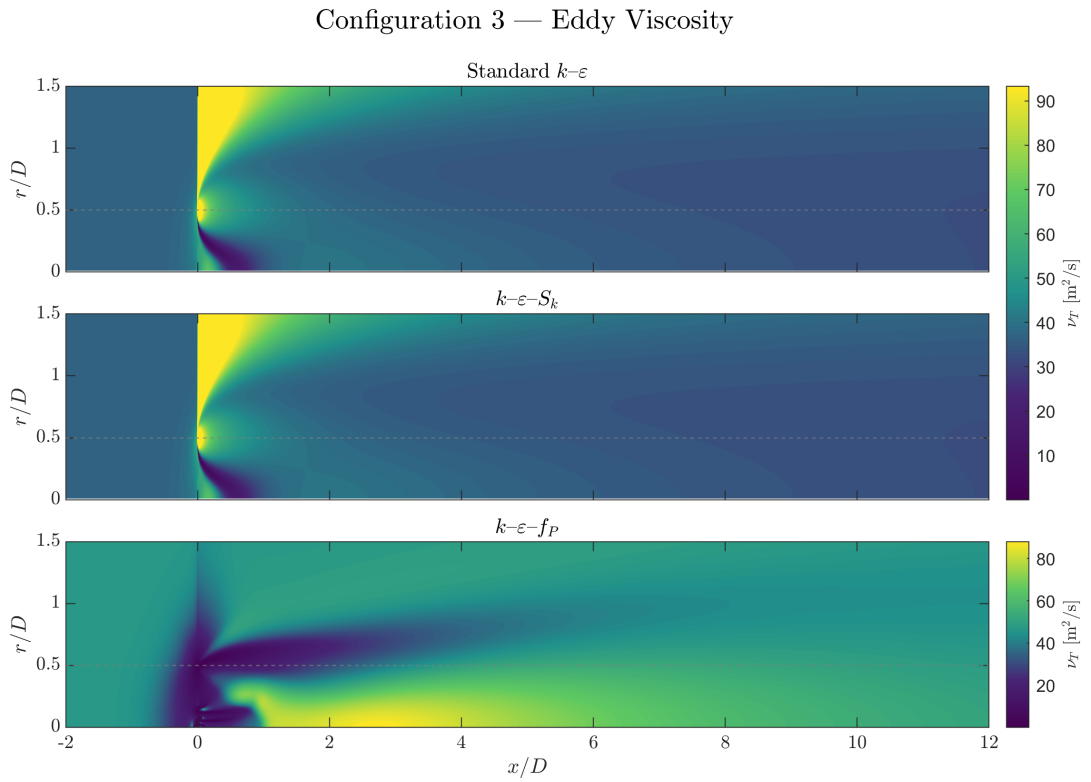

Figure 5.8: Eddy viscosity ν_T contours for configuration 3, original model ($\frac{\partial V}{\partial x}$ included). From top to bottom: standard k–ε, k–ε–S_k, k–ε–f_P. No LES reference is available for this quantity.

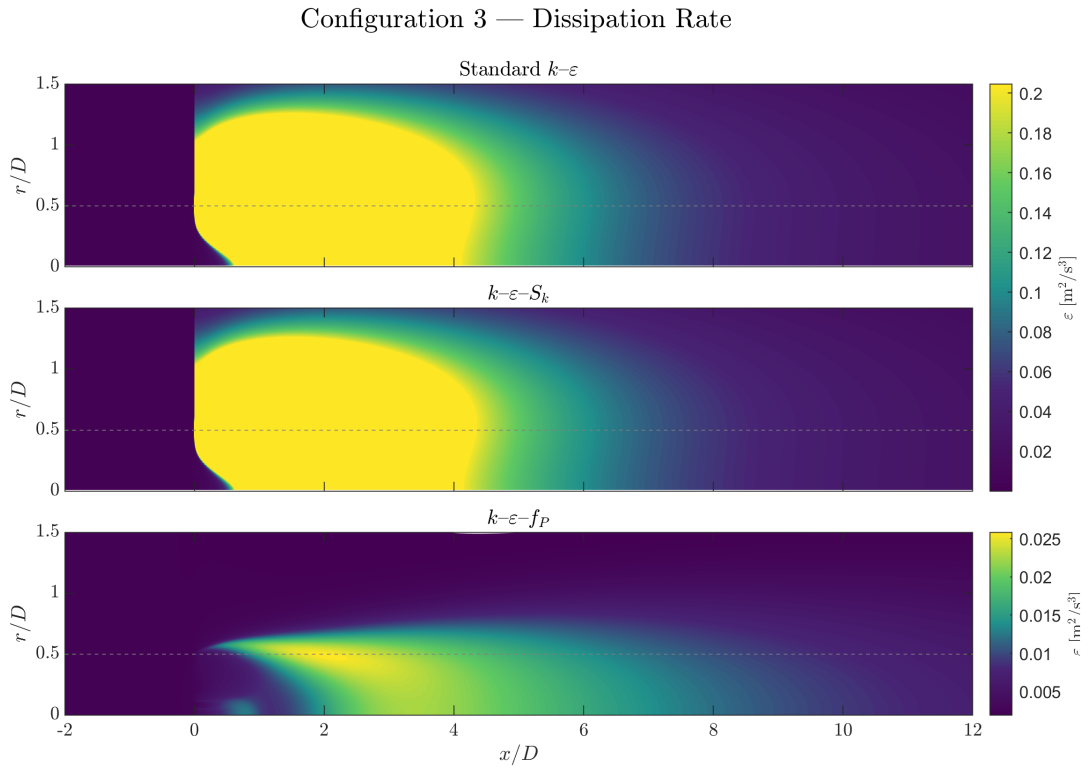

Figure 5.9: Dissipation rate ε contours for configuration 3, original model ($\frac{\partial V}{\partial x}$ included). From top to bottom: standard k–ε, k–ε–S_k, k–ε–f_P. No LES reference is available for this quantity. Note the different colourbar scales.

5.4 Results From Modified Model with $\frac{\partial V}{\partial x}$ Neglected

In this section the results from the modified model formulation are presented. In the modified model, the $\frac{\partial V}{\partial x}$ term is neglected in the strain-rate invariant, in an attempt to improve numerical stability. This led to the solver converging in eleven out of twelve cases, as opposed to only five cases converging for the original model formulation. Although the results are not obtained with the original model formulation, the increased number of converged cases makes it possible to better compare the turbulence models. Only the k–ε–f_P model in configuration 1 did not converge.

5.4.1 Axial Velocity

The error metrics of the axial velocity in the near-, far- and full- wake are shown in Table 5.5, Table 5.6 and Table 5.7. The k–ε–f_P model has lower errors in every configuration in the near- and full- wake, while k–ε–S_k performs better in the far-wake. The standard model performs the worst in both near- and far-wake. The RRMSE values are larger than the MAPE values in every case, suggesting that errors are mostly locally concentrated instead of evenly spread out. Similar as for the original model results, the errors are largest for configuration 1 and smallest for configuration 4. Hence, the error increases with decreasing wind speed and increasing thrust coefficient. Configurations 2 and 3 have very similar errors, with configuration 2 having slightly larger errors suggesting that a lower turbulence intensity increases the error of the velocity predictions.

Table 5.5: Error metrics for the axial velocity U in the near wake ($-2D \leq x < 3D$), $\partial V/\partial x$ neglected.

	MAPE [%]				RRMSE [%]			
Model	C 1	C 2	C 3	C 4	C 1	C 2	C 3	C 4
Standard k–ε	11.03	9.61	9.20	1.55	16.57	14.87	14.36	2.48
k–ε–S_k	7.51	6.18	5.70	1.44	11.15	9.28	8.59	2.26
k–ε–f_P	–	3.64	3.66	1.11	–	5.36	5.41	1.55

Table 5.6: Error metrics for the axial velocity U in the far wake ($3D \leq x < 10D$), $\partial V/\partial x$ neglected.

	MAPE [%]				RRMSE [%]			
Model	C 1	C 2	C 3	C 4	C 1	C 2	C 3	C 4
Standard k–ε	11.67	9.48	9.12	2.21	14.66	12.82	12.01	3.11
k–ε–S_k	7.20	4.43	4.21	2.08	8.92	6.56	5.85	2.92
k–ε–f_P	–	4.85	5.22	1.99	–	6.52	6.78	2.77

Table 5.7: Error metrics for the axial velocity U over the full wake ($-2D \leq x < 10D$), $\partial V/\partial x$ neglected.

	MAPE [%]				RRMSE [%]			
Model	C 1	C 2	C 3	C 4	C 1	C 2	C 3	C 4
Standard k–ε	11.40	9.53	9.16	1.93	15.50	13.73	13.06	2.86
k–ε–S_k	7.33	5.17	4.84	1.81	9.94	7.83	7.14	2.66
k–ε–f_P	–	4.34	4.56	1.62	–	6.06	6.24	2.33

Figure 5.10 shows the contourplots from the configuration 3 results compared to the LES data. The other configurations' contourplots can be seen in Appendix D. One can see that the standard model has by far the largest overprediction of the wake recovery, showing already a very large difference between the LES and FAWM velocity profiles at the $x/D = 2$. The k–ε–f_P has the best prediction of the wake deficit in the near-wake, while The k–ε–S_k has a better prediction in the far-wake. This is consistent with the observations from the error metrics. In the far-wake, the difference between the three results become smaller, although it stays clear that the k–ε–S_k model matches the LES prediction best.

Configuration 2 shows a very similar result as configuration 3. In configuration, only the standard and k–ε–S_k models are available. They show that the k–ε–S_k model performs better than the standard model. However, the k–ε–S_k model does not perform as well in the far-wake as it does in configurations 2 and 3. Configuration 4 uses the lowest turbine thrust coefficient, which is clearly visible from its reduced wake deficit compared to the other models. All three models perform more or less similar, all though the k–ε–f_P model still predicts the near-wake deficit better. The wake expansion is also overpredicted by all three models already in the near-wake and in all configurations. In the far-wake,

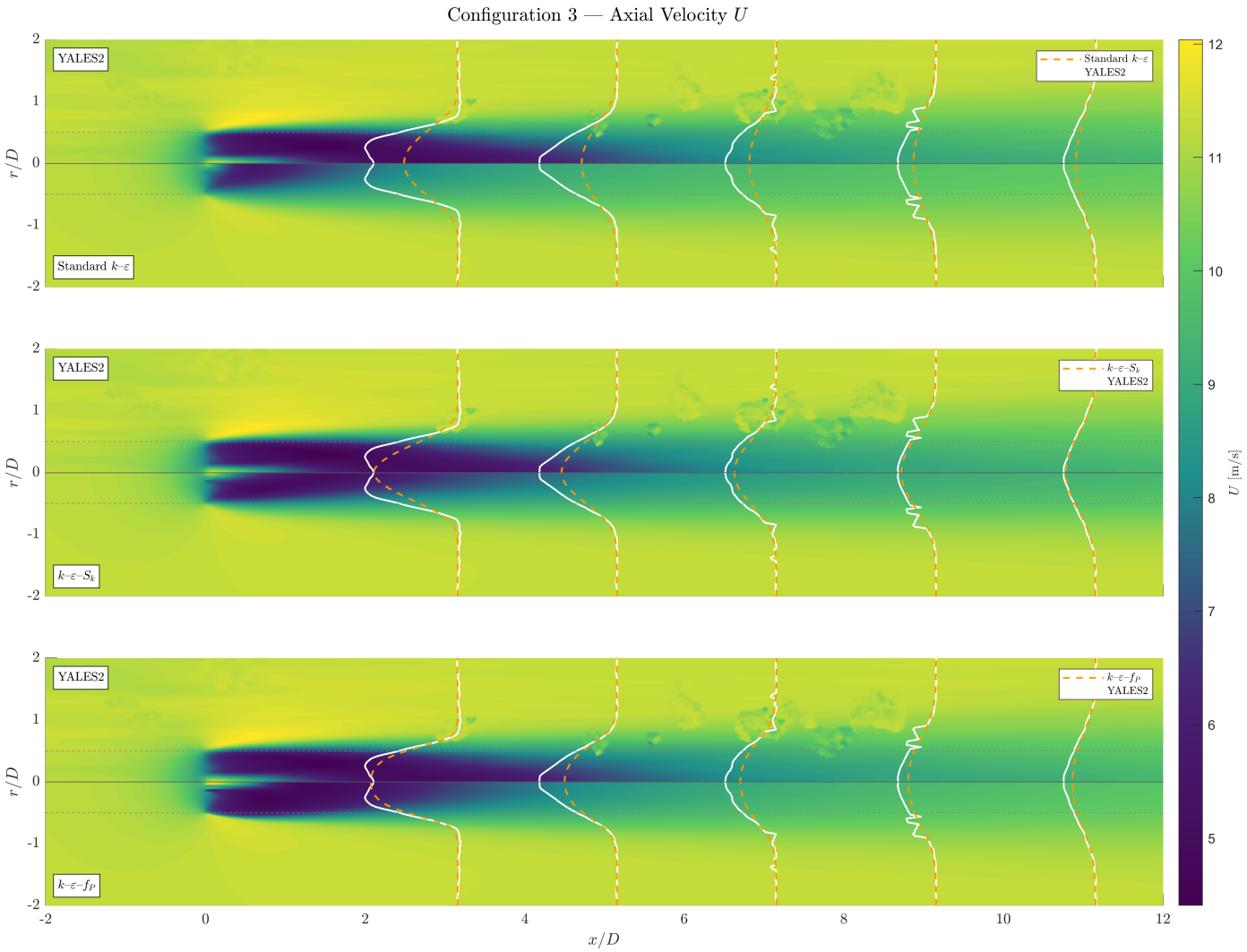

Figure 5.10: Axial velocity U for configuration 3, modified model ($\frac{\partial V}{\partial x}$ neglected). Upper half: YALES2 LES; lower half: FAWM. From top to bottom: standard k–ε, k–ε–S_k, k–ε–f_P. Radial profiles at selected downstream stations are overlaid (solid: YALES2, dashed: FAWM).

the wake expansions approximately matches the LES prediction. However, in configurations 1 and 4 the expansion is also overpredicted in the far-wake.

5.4.2 Turbulent Kinetic Energy

The error metrics of k in the near-wake, far-wake and full-wake are shown in Table 5.8, Table 5.9 and Table 5.10. All three models overpredict k by a large margin in both the near- and far-wake, with errors ranging from 49% to 126%. The k–ε–S_k model produces the lowest errors in all configurations and in both parts of the wake. The k–ε–f_P model performs better than the standard k–ε model in the near-wake, while the standard model performs better in the far-wake. When considering the full-wake, k–ε and k–ε–f_P produce similar errors.

It is less clear which configurations cause the smallest and largest errors, since this differs per wake region. In the near- and full-wake, configuration 4 produces the lowest errors and also gives similar results for all three models. The other configurations show more variation between the models. For configuration 1, the standard model has much larger errors than k–ε–S_k, while k–ε–f_P did not converge. For configurations 2 and 3, the standard model performs better in the far-wake and k–ε–f_P performs better in the near-wake, but in the full-wake they produce similar errors.

Table 5.8: Error metrics for the turbulent kinetic energy k in the near wake ($-2D \leq x < 3D$), $\partial V/\partial x$ neglected.

	MAPE [%]				RRMSE [%]			
Model	C 1	C 2	C 3	C 4	C 1	C 2	C 3	C 4
Standard k–ε	98.14	113.29	89.78	22.92	132.65	163.86	127.21	25.75
k–ε–S_k	53.01	64.50	48.61	21.03	67.89	93.99	67.36	24.00
k–ε–f_P	–	70.91	62.90	21.72	–	106.12	89.38	24.89

Table 5.9: Error metrics for the turbulent kinetic energy k in the far wake ($3D \leq x < 10D$), $\partial V/\partial x$ neglected.

	MAPE [%]				RRMSE [%]			
Model	C 1	C 2	C 3	C 4	C 1	C 2	C 3	C 4
Standard k–ε	156.69	73.54	70.46	101.52	158.54	75.74	73.15	103.20
k–ε–S_k	119.43	54.22	49.82	96.09	120.11	56.44	52.22	97.97
k–ε–f_P	–	104.51	95.98	102.49	–	111.38	101.70	104.30

Table 5.10: Error metrics for the turbulent kinetic energy k over the full wake ($-2D \leq x < 10D$), $\partial V/\partial x$ neglected.

	MAPE [%]				RRMSE [%]			
Model	C 1	C 2	C 3	C 4	C 1	C 2	C 3	C 4
Standard k–ε	126.41	87.63	78.11	53.29	146.00	110.29	97.02	57.74
k–ε–S_k	85.07	57.86	49.34	50.04	93.44	70.24	58.39	54.64
k–ε–f_P	–	92.60	82.88	52.93	–	110.80	97.39	57.91

The contour plots for configurations 1 and 2 are shown in Figure 5.12 and Figure 5.11. The remaining contour plots are shown in Appendix D. All models greatly overpredict the production of turbulence in the near-wake, but especially the standard k–ε model. The k–ε–S_k and k–ε–f_P models reproduce a radial profile shape similar to LES in the near-wake, while the standard model does not. However, the width of the region where k is produced is much wider than in the LES results. In the far-wake, the shape and width of the radial profiles predicted by the models become similar to those predicted by LES, although the magnitudes remain much larger. The LES shows strong production at the rotor edge and almost none at the centreline, while the FAWM results also show significant production at the centreline. The standard model in particular shows production across the entire rotor disk. The other two models produce a better result, with the most production at the tip and some production near the centre.

Configuration 3 shows a similar trend to configuration 2, but configuration 4 is a strong outlier. Configuration 4 has the lowest thrust coefficient and therefore produces the least amount of turbulence. This is captured by the FAWM models. However, the turbulent kinetic energy in the LES data dissipates much faster than in the FAWM data, which leads to a large overprediction across the entire wake. All three models behave similarly for configuration 4.

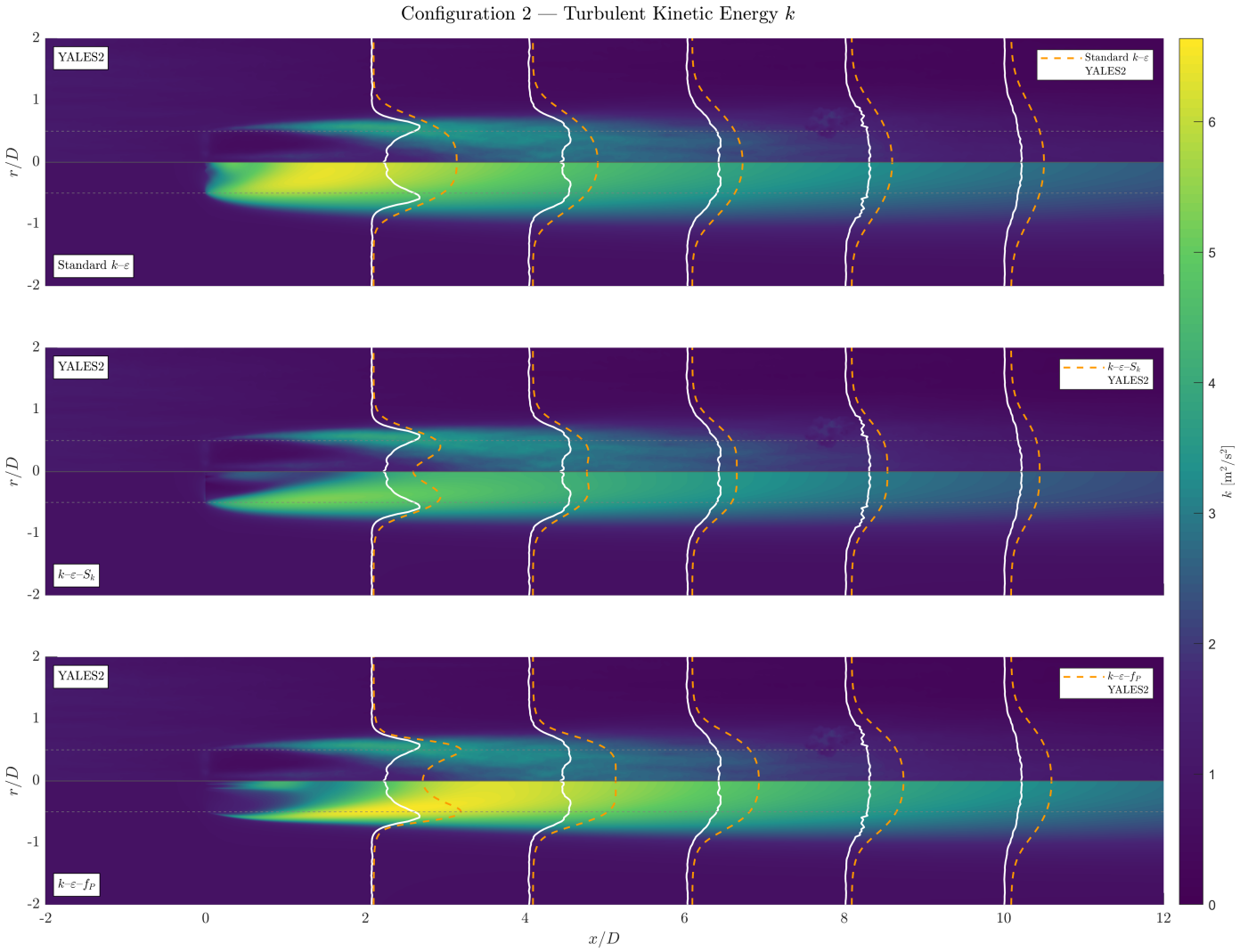

Figure 5.11: Turbulent kinetic energy k for configuration 2, modified model ($\frac{\partial V}{\partial x}$ neglected). Upper half: YALES2 LES; lower half: FAWM. From top to bottom: standard k–ε, k–ε–S_k, k–ε–f_P. Note the different colourbar scales between the models.

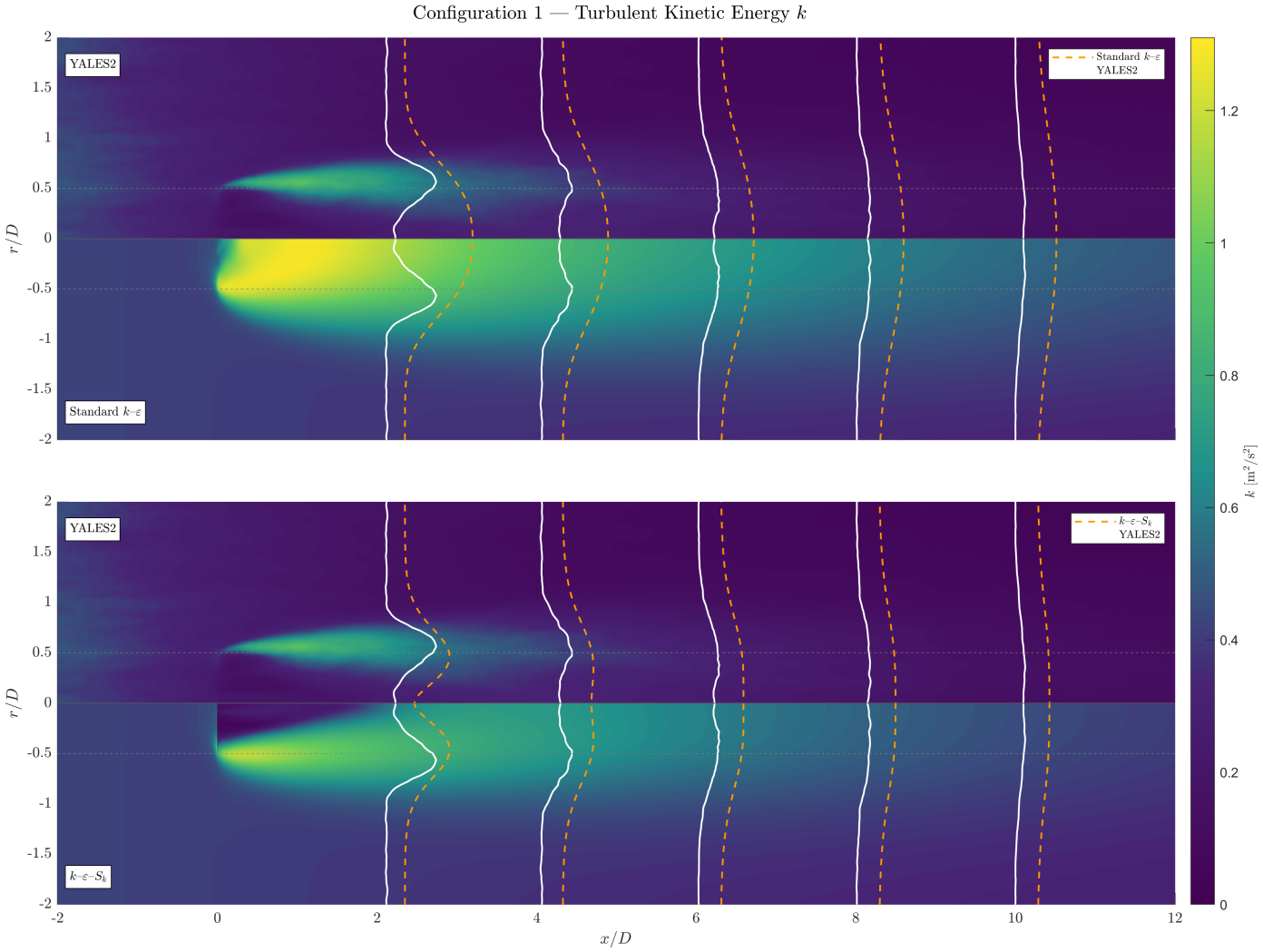

Figure 5.12: Turbulent kinetic energy k for configuration 1, modified model ($\frac{\partial V}{\partial x}$ neglected). Upper half: YALES2 LES; lower half: FAWM. Top: standard k–ε; bottom: k–ε–S_k. The k–ε–f_P model did not converge for this configuration.

5.4.3 Radial Velocity

The contour plots and radial profiles of the radial velocity for configuration 3 are shown in Figure 5.13. The remaining contour plots are shown in Appendix D. The LES data shows a relatively large velocity gradient at the rotor disk, caused by the expansion of the wake. Further downstream, the radial velocity decreases and becomes negative. The LES profiles also contain a considerable amount of noise. In this configuration, the standard k–ε and k–ε–S_k models show relatively good agreement with the LES data near the rotor. But the FAWM results quickly underpredict the radial velocity profiles when moving further downstream. In the far-wake, the FAWM predicts almost no radial velocity, while the LES data still shows a substantial negative radial flow.

For configurations 1, 2 and 3, the k–ε–S_k model performs best and the k–ε–f_P model performs worst. In configuration 4, all models perform poorly and the radial profiles predicted by LES are unexpected. The LES predicts that the radial velocity increases at the outboard region of the shown domain.

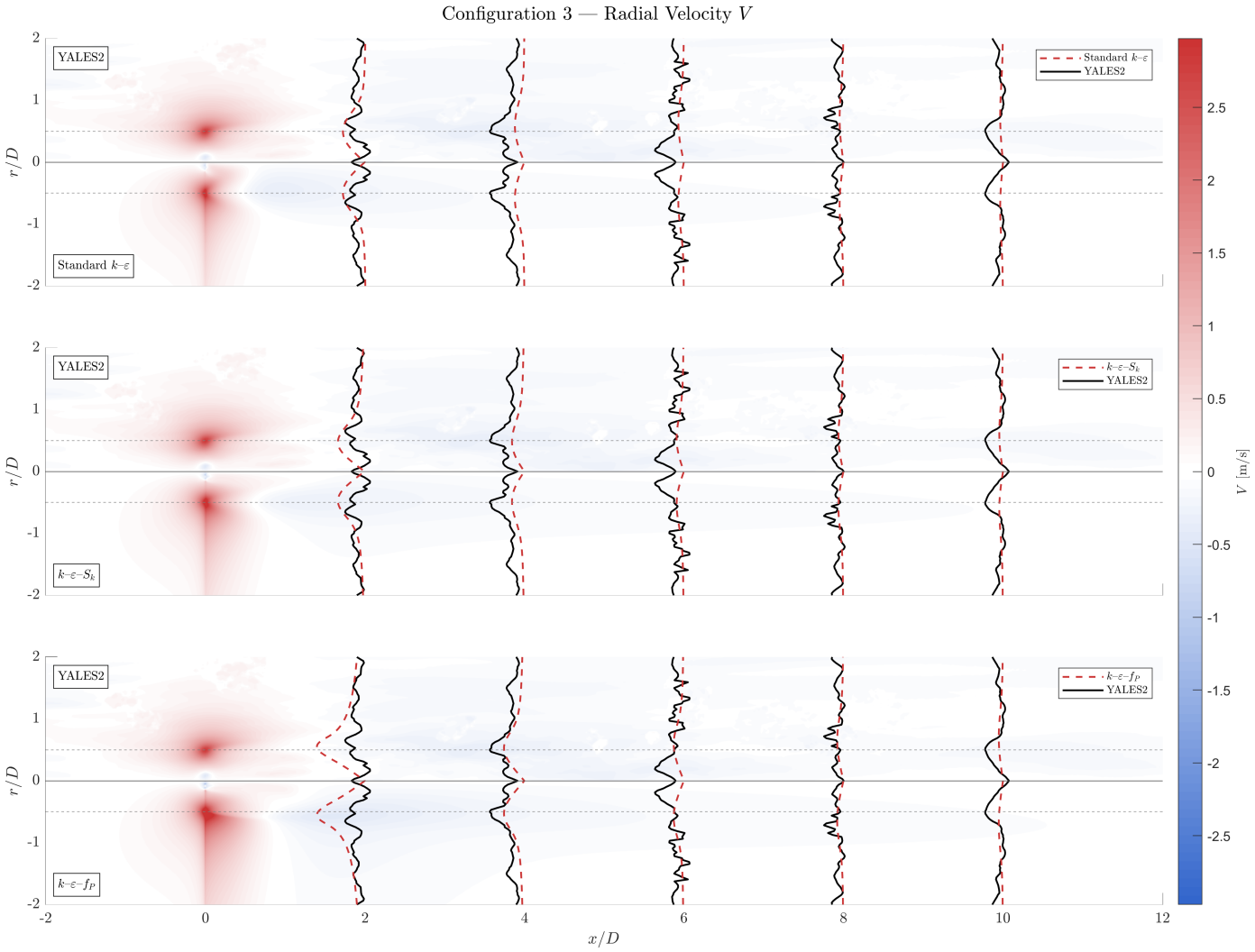

Figure 5.13: Radial velocity V for configuration 3, modified model ($\frac{\partial V}{\partial x}$ neglected). Upper half: YALES2 LES; lower half: FAWM. From top to bottom: standard k–ε, k–ε–S_k, k–ε–f_P. Radial profiles at selected downstream stations are overlaid (solid: YALES2, dashed: FAWM).

5.4.4 Eddy Viscosity

Since no LES data is available for the eddy viscosity, the FAWM models are only compared among themselves in this subsection. The contour plots resulting from configuration 2 are shown in Figure 5.14. The remaining contour plots are shown in Appendix D. All three models produce distinctly different spatial distributions of ν_T, consistent across most configurations. The standard k–ε model has the largest eddy viscosity in the near-wake, after which it slowly decreases when moving downstream. The k–ε–S_k model shows a slight increase right in front of the actuator disk, after which it abruptly declines. This decline is caused by the sink term applied at the actuator disk in the k-equation. The k–ε–f_P model shows the most variation of ν_T across the domain. Its minimum regions are located at the actuator disk and the wake boundary, where the increased velocity gradients lower f_P and therefore decrease the eddy viscosity. It also

produces the smallest values of ν_T, smaller than the k–ε–S_k model. In the centre of the near-wake, ν_T increases sharply due to the produced k and declined velocity gradients. It reaches its maximum at around $x/D = 3$, after which it slowly reduces in the far-wake.

It can also be seen that outside of the wake, the eddy viscosity predicted by the k–ε–f_P model is larger than predicted by the other two models. This is because the model is calibrated for an atmospheric boundary layer, where dissipation and production are in equilibrium. When the ratio P_k/ε increases or decreases, f_P decreases or increases accordingly. In a fully 3D elliptic RANS solver, the atmospheric boundary layer is usually modelled, which causes production of k outside of the wake. However, in the present FAWM model the ABL is not modelled and hence there is no P_k outside of the wake. The k–ε–f_P model interprets this as P_k/ε being below the calibrated value and compensates by increasing the eddy viscosity. This causes the increased ν_T outside of the wake in the k–ε–f_P predictions.

The results from configurations 2 and 3 look more or less identical, while the results from configuration 1 look qualitatively similar but have much lower values. Configuration 1 has the smallest maximum value of approximately 35 m^2/s. The contour plots from configuration 4 look different from the other results. For the standard k–ε and k–ε–S_k models, ν_T is only slightly increased in the wake. Furthermore, the latter model only reduces the eddy viscosity moderately at the rotor disk. Meanwhile, the k–ε–f_P model shows a much larger decrease of the eddy viscosity with a similar spatial distribution as in the other configurations. Across all configurations, the three models show a consistent ordering of the eddy viscosity magnitude. The standard k–ε model produces the highest values, while the k–ε–f_P model produces the lowest.

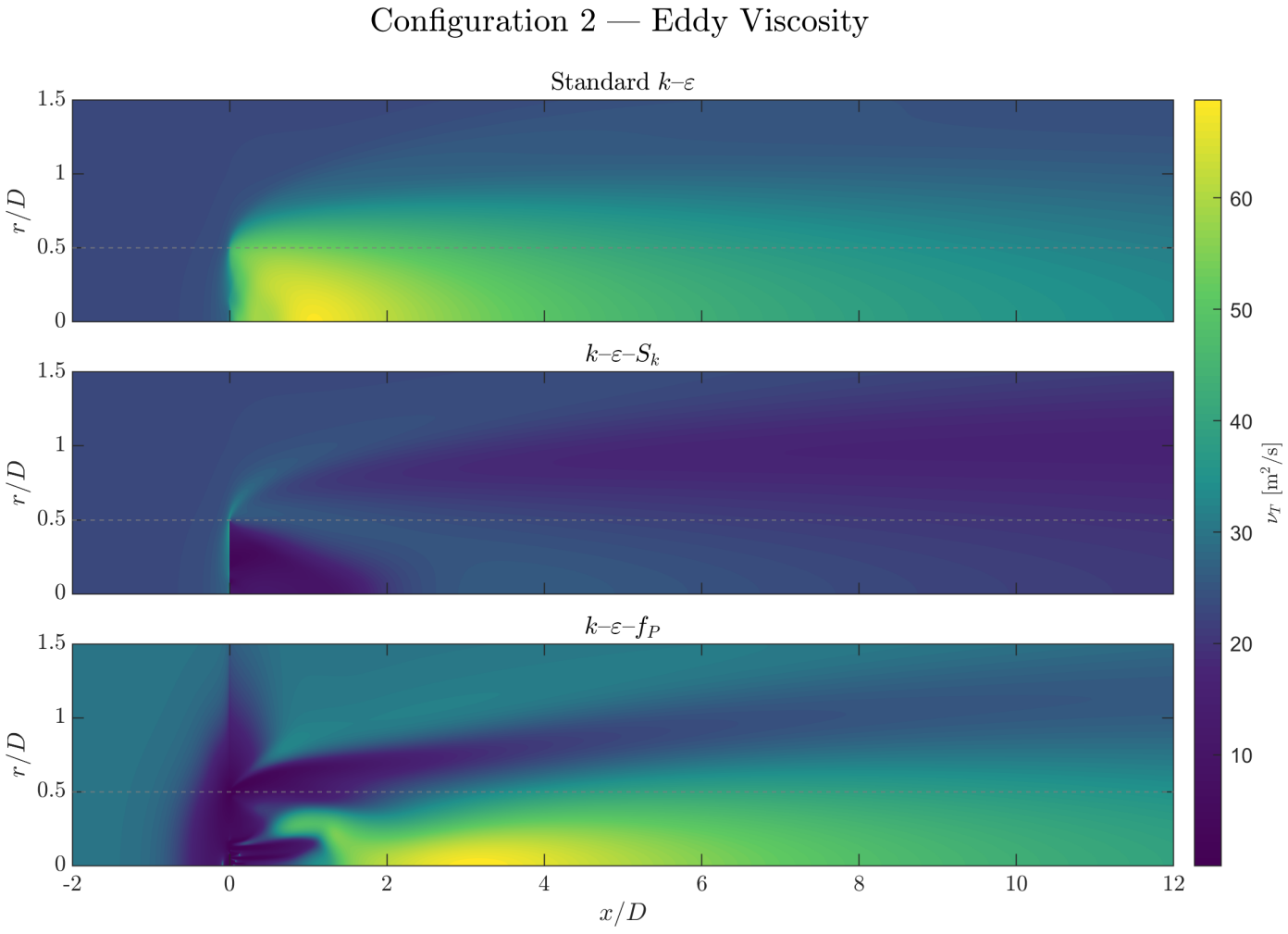

Figure 5.14: Eddy viscosity ν_T contours for configuration 2, modified model ($\frac{\partial V}{\partial x}$ neglected). From top to bottom: standard k–ε, k–ε–S_k, k–ε–f_P. No LES reference is available for this quantity.

5.4.5 Dissipation Rate

There is no LES data available for the dissipation rate. Hence, the FAWM results are only compared among themselves in this section and no error metrics are available. The dissipation rate contours for configuration 2 are shown in Figure 5.15. The remaining contour plots are shown in Appendix D. All models show that dissipation is produced primarily at the rotor tip and to a lesser extent in the middle region of the disk. The k–ε–S_k model has the largest maximum dissipation, occurring at the wake boundary at approximately $x/D = 2$. The standard k–ε model predicts the lowest dissipation rate. The standard model also shows the fastest reduction of ε, while the dissipation rate in the k–ε–S_k and k–ε–f_P models extends further downstream to approximately the same axial distance.

The spatial distributions, maximum and minimum values and downstream extent in configurations 2 and 3 are more or less identical. Configuration 1 shows a similar trend, but with a much quicker decrease of ε, especially for the standard model. The values in configuration 1 are also an order of magnitude lower than in configurations 2 and 3. In configuration 4, the standard k–ε and k–ε–S_k results look identical. The k–ε–f_P model has a similar shape but with a smaller maximum value. All three models decay at a similar rate.

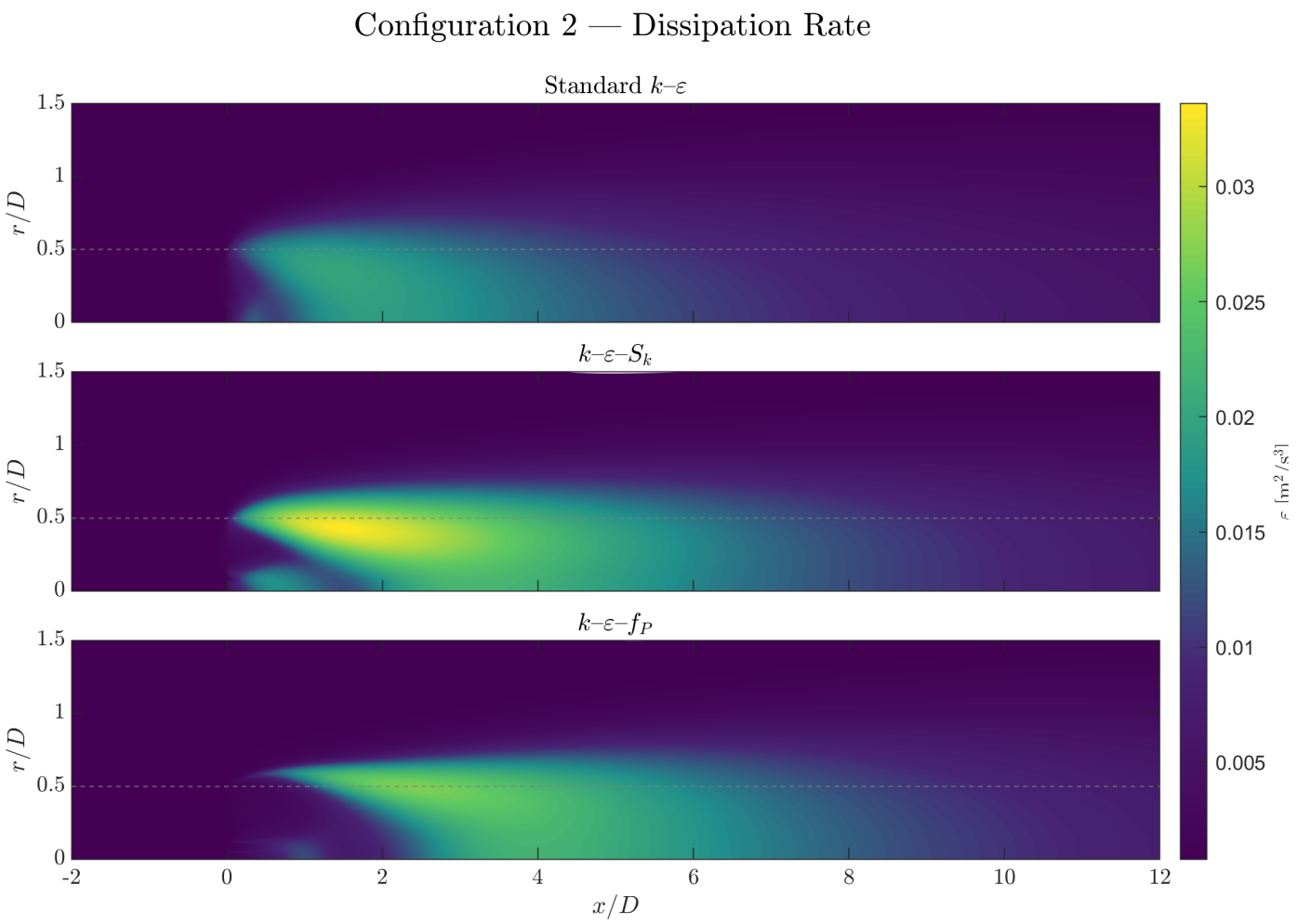

Figure 5.15: Dissipation rate ε contours for configuration 2, modified model ($\frac{\partial V}{\partial x}$ neglected). From top to bottom: standard k–ε, k–ε–S_k, k–ε–f_P. No LES reference is available for this quantity. Note the same colourbar scale for all three models.

5.4.6 Behaviour of the Extended-Model Correction Terms

In Figure 5.16, the S_k sink term computed in all four configurations is shown. Configurations 2 and 3 have by far the largest sink term, with configuration 3 being significantly larger than configuration 2. This is expected, since configuration 3 corresponds to a higher turbulence intensity case than configuration 2, leading to more turbulent kinetic energy being absorbed by the actuator disk. Configuration 4 has an almost negligible magnitude, which explains the small differences between the results of the standard k–ε and k–ε–S_k models in configuration 4 in the previous subsections. Configuration 1 lies in between the largest and smallest magnitudes. Even though it operates at the largest thrust coefficient, the wind speed is by far the smallest, leading to a smaller turbulent kinetic energy and therefore a smaller sink term.

Figure 5.17 shows the contour plots of the spatial distribution of f_P for the three configurations that converged. The distributions look very similar, with configuration 4 having a smaller region where f_P is reduced. This can be explained by the fact that configuration 4 has the smallest thrust coefficient and velocity gradients, so its ratio P_k/ε is closer to equilibrium than in the other configurations. It is also clear that f_P is at its maximum value everywhere outside the wake. As explained before, the axisymmetric nature of the FAWM solver makes it impossible to model the ABL, so $P_k = 0$ outside of the wake, causing f_P to increase.

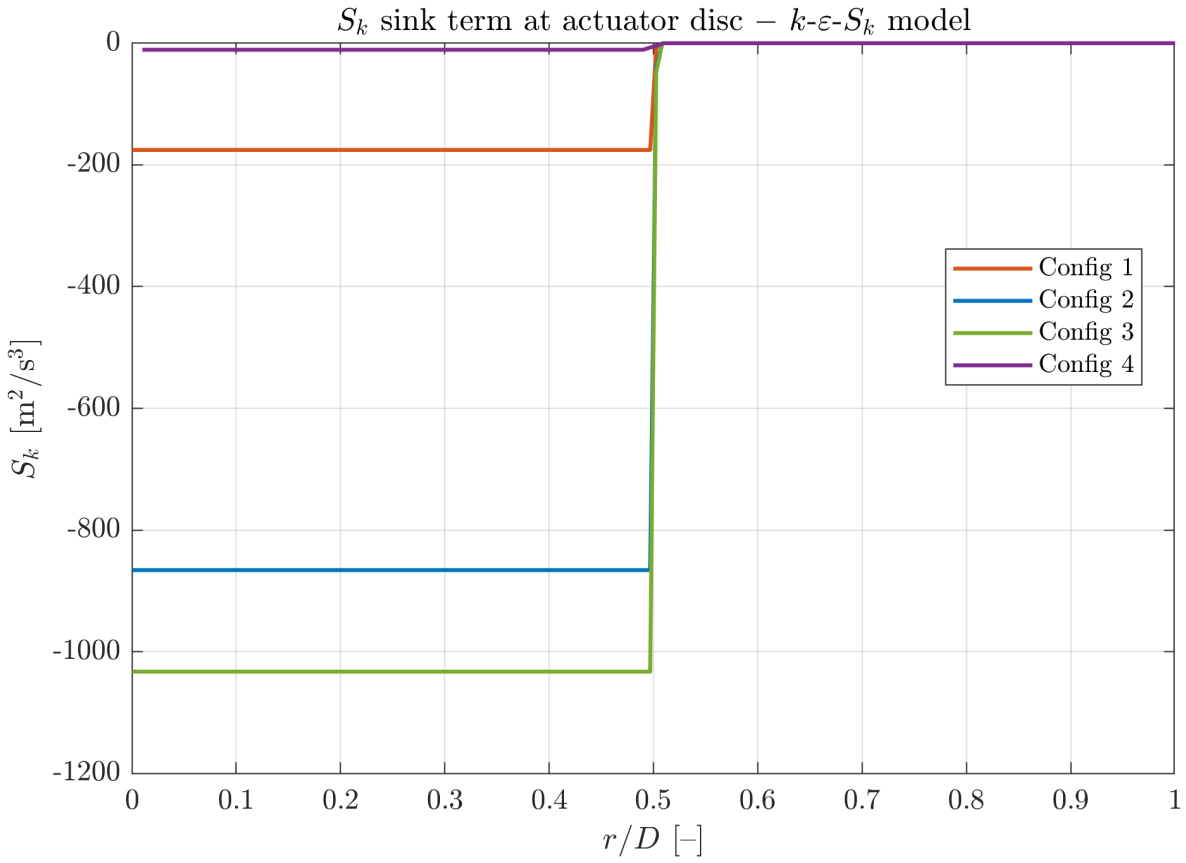

Figure 5.16: Radial distribution of the S_k sink term at the actuator disk plane for all four configurations. The correction acts only inside the rotor disk ($r/D < 0.5$) and vanishes outside.

5.4.7 Comparison Between Original and Modified Model

By comparing the axial velocity predictions of the original model, with the $\frac{\partial V}{\partial x}$ term included in the production term with those of the modified model, with the $\frac{\partial V}{\partial x}$ term excluded in the production term, it becomes clear that the latter performs better, although the differences are relatively small. For the turbulent kinetic energy, the differences are much more substantial. In two of the cases with the original model, k diverged to nonphysical values. For the cases where the original model does produce reasonable predictions of k, the modified model with $\frac{\partial V}{\partial x}$ neglected in the production term still outperforms it in both the near- and far-wake. The eddy viscosity predicted by the original model is substantially larger than that predicted by the modified model. In contrast, the dissipation rates predicted by both models are of similar magnitude, when considering only the cases of the original model that remained within reasonable bounds.

In short, neglecting $\frac{\partial V}{\partial r}$ in the production term leads to an improved convergence behaviour of the FAWM, with only one configuration diverging instead of five. Additionally, all produced values remain within reasonable bounds, although k is still widely overpredicted by all three models. Overall, the modified model leads to a better agreement between the FAWM and LES results for all considered flow variables.

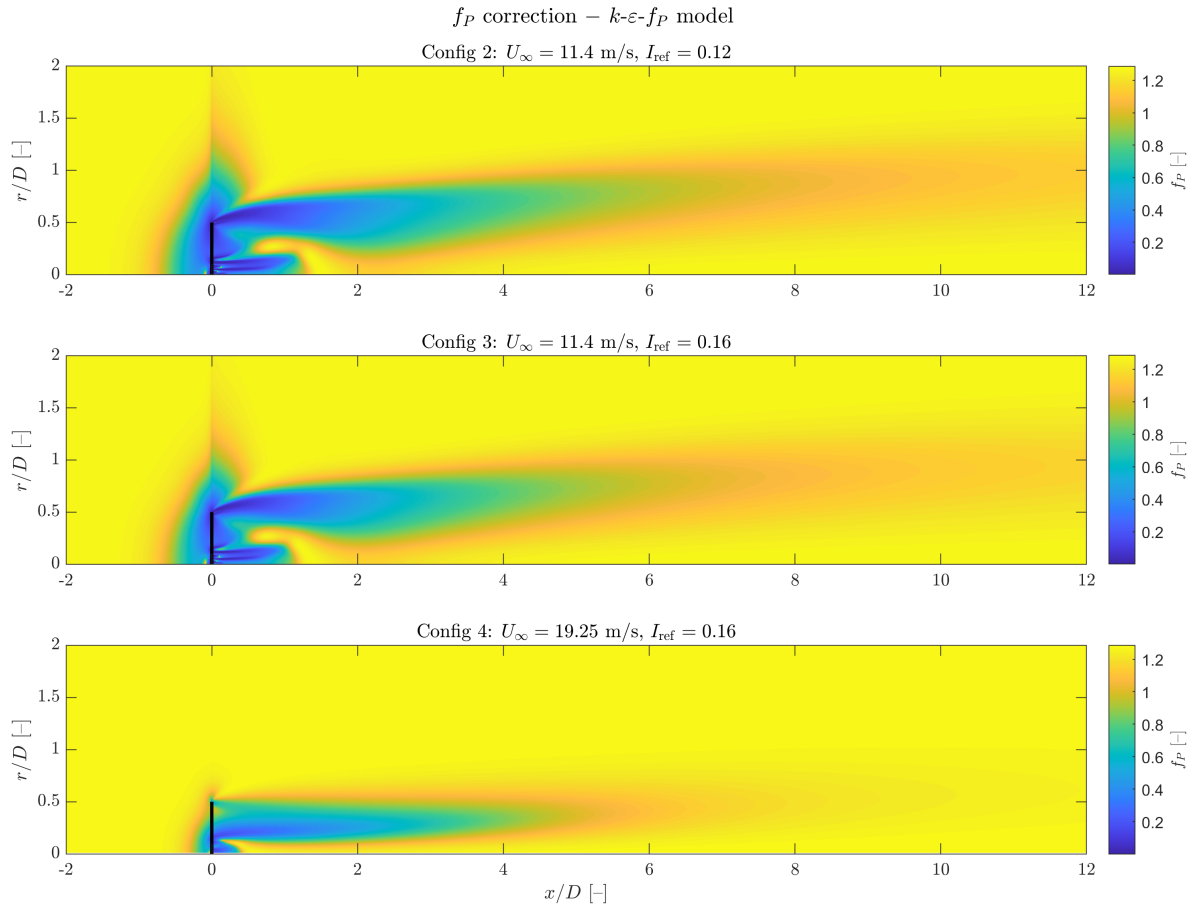

Figure 5.17: Contours of the f_P correction function for configurations 2–4 ($\frac{\partial V}{\partial x}$ neglected). The function reaches its minimum values at the wake shear layer near the blade tip and recovers towards unity in the far wake.

6 Conclusions and Recommendations

The objective of thesis was to develop a parabolized, axisymmetric turbulence model that could be coupled to Siemens Energy's Forced Ainslie Wake Model. This chapter addresses the research questions formulated in Section 2.4.4, presents the conclusions drawn from the results, and offers recommendations for future work. It is structured into two sections. Firstly, Section 6.1 answers the research questions and presents the overall conclusions. Secondly, Section 6.2 discusses suggestions for future work.

6.1 Conclusions

The primary research question of this thesis was whether the standard k–ε model and its two extended variations could be successfully implemented into the parabolic FAWM solver. The two model extensions are a TKE sink term S_k at the actuator disk [7] and the f_P factor that limits the eddy viscosity in regions where P_k/ε is out of equilibrium. The answer to this question remains uncertain. The original model formulations, with $\frac{\partial V}{\partial x}$ included in the production term, led to numerical instabilities in over half the simulated cases. Furthermore, in some of the cases that did converge, nonphysical values of k and ε were predicted. The source of the instabilities was found to be the axial gradient of the radial velocity, $\frac{\partial V}{\partial x}$, which was two orders of magnitude larger in the FAWM solver than in the LES data. This can be explained by the irregular forcing term and the parabolized nature of the solver. The force term in the axial momentum equation has large axial gradients in the region close to the actuator disk, which are propagated to the axial velocity. Using the axisymmetric continuity equation, it can be shown that $\frac{\partial V}{\partial x}$ depends on $\frac{\partial^2 U}{\partial x^2}$, so sharp gradients in the forcing term are amplified in $\frac{\partial V}{\partial x}$. In a fully elliptic RANS solver, the axial diffusion and pressure terms act as stabilisers and smoothen large gradients. But in the parabolized solver these terms are neglected, making the solver less able to handle large gradients. The first research question can therefore not be answered positively, since the original model formulation is not reliably integrated.

In an attempt to improve the stability of the solver, a modified model formulation was proposed in which $\frac{\partial V}{\partial x}$ was neglected in the production term. This led to improved results. The modified model converged in eleven out of twelve cases, as opposed to only five for the original model. Furthermore, the modified model's predictions stayed within physical bounds and showed a better agreement with the LES data. The second research question, which asks how the FAWM predictions compare against LES data, is therefore answered with the modified model in mind.

For the axial velocity, the k–ε–f_P model performs best in the near-wake, while the k–ε–S_k model performs best in the far-wake. The standard k–ε model has the largest errors in both regions. The velocity errors increase with increasing thrust coefficient and decreasing wind speed, which is expected since higher thrust generates stronger shear layers that cause the equilibrium assumptions of the k–ε model to break down. For the turbulent kinetic energy, the ranking reverses. The k–ε–S_k model produces the lowest TKE errors, while the standard model and k–ε–f_P model have larger and comparable errors. This leads to a trade-off between the two extended models. The f_P correction reduces the eddy viscosity in the near-wake where the strain-rate is high, which limits turbulent diffusion and improves the velocity predictions. But f_P recovers further downstream as the shear decays, so its effect on the TKE is mainly confined to the near-wake. The S_k term, on the other hand, removes a fixed amount of TKE at the actuator disk, which reduces the overall TKE level that is advected through the entire wake.

The k–ε–f_P model overpredicting TKE relative to the standard model in some configurations can be explained by its calibration. Since the FAWM is not able to model an atmospheric boundary layer, the ratio P_k/ε drops below its calibrated equilibrium value outside of regions with large velocity gradients. This causes f_P to increase and therefore also increases the eddy viscosity beyond the standard value.

The TKE errors are larger than the velocity errors across all configurations and models. This is expected, since RANS turbulence modelling for wind turbine wakes is known to overpredict the production of k. The k–ε–S_k model makes the best predictions of k in both the near- and far-wake, although it still overpredicts the LES values. The TKE overprediction is not unique to the parabolic FAWM solver but is consistent with the findings of Laan and Andersen [41], who showed that the standard model overpredicts the turbulence length scale in the near wake. Furthermore, it was found that the k–ε–f_P model and other models tested in that study also overpredict k in the far-wake, since their formulations approach the standard model in that region.

The sink term S_k is now only applied directly at the actuator disk. An option was added to the model to regularize the sink term over a larger region in axial and radial directions. However, this was not applied in the validation simulations, since it did not improve stability and the regularization method does not conserve the total unregularized sink term. Because the sink term is only applied at the disk, there is still some production of k in front of the AD in the k–ε–S_k model that is not there in the LES field. Right after the actuator disk there is a sharp decrease of k. Spreading S_k over

multiple axial cells would reduce this stepwise behaviour and might improve predictions in the near-wake.

In summary, the extended closures improve predictions compared to the standard k–ε model for both the velocity deficit and the turbulent kinetic energy. The k–ε–f_P model provides the best velocity predictions, while the k–ε–S_k model provides the best TKE predictions. No single model is best for all variables, and the choice between them depends on whether velocity or turbulence accuracy is more important for the application at hand. However, these conclusions are based on results from the modified formulation, where $\frac{\partial V}{\partial x}$ was not included in the production term due to stability constraints.

6.2 Recommendations

It should be noted, that the results discussed in the previous section were obtained with the modified model in which the velocity gradient $\frac{\partial V}{\partial x}$ is neglected in the production term. This was done because the original formulation, with $\frac{\partial V}{\partial x}$ included in the production term, was unstable in most cases and produced nonphysical results. Further research should be done towards the origin of the stability issue and how it can be mitigated. One possible solution might be to alter the boundary conditions of the FAWM. At the outer boundary $r = r_{\text{max}}$, Robin boundary conditions for the axial velocity U are applied. This means the radial velocity V is not forced to reduce to zero toward the boundary, as is the case in the far-field of a real wake. Altering the boundary conditions so that $V = 0$ is satisfied at the boundary, might help to reduce V and its axial derivative along the axial coordinate of the AD. However, this hypothesis was tested by a fellow graduate intern at Siemens Energy. This student implemented the FAWM formulation that is currently in FVM into FEM. He was able to change the boundary conditions in his model such that the radial velocity V was forced to zero at the outer boundary. However, this did not affect the behaviour of of V along the largest region of the domain, but only forced it to quickly drop at the vicinity of the outer boundary. Further work is needed to improve the prediction of V at the axial coordinate of the AD.

In the case of the modified model, with $\frac{\partial V}{\partial x}$ omitted in the production term, the k–ε–f_P model failed to converge for the configuration with the highest thrust coefficient. Coupling the f_P correction with the parabolic FAWM solver may require additional numerical stabilization at high thrust settings, for example by imposing a lower bound on the effective eddy viscosity. Furthermore, the f_P function was originally calibrated for neutral atmospheric boundary layer flows. In the axisymmetric FAWM formulation no boundary layer is present, which causes f_P to exceed unity outside of the wake and in the far wake. Recalibrating the constant C_R for the axisymmetric wake geometry could improve the TKE predictions.

The S_k and f_P corrections address different aspects of the turbulence modelling problem. Therefore, a combined model that applies S_k at the actuator disk and f_P in the wake could be possible, so that the benefits of both approaches can be applied.

Finally, all validation in this thesis has been performed for a single wind turbine. It is recommended to extend the validation to other turbine configurations and to full wind farms. This would test whether the k–ε models can handle increased inflow turbulence and non-uniform velocity profiles, and whether the errors observed for a single turbine accumulate when multiple wakes interact.

References

[1] T. B. Nickels and A. E. Perry, “An experimental and theoretical study of the turbulent coflowing jet,” *Journal of Fluid Mechanics*, vol. 309, pp. 157–182, 1996.

[2] N. G. W. Warncke et al., “Ainslie Wake Model with forcing term,” *Journal of Physics: Conference Series*, vol. 3016, no. 1, p. 012 016, 2025. DOI: 10.1088/1742-6596/3016/1/012016.

[3] IPCC, *Climate Change 2013: The Physical Science Basis. Contribution of Working Group I to the Fifth Assessment Report of the Intergovernmental Panel on Climate Change*, T. F. Stocker et al., Eds. Cambridge, United Kingdom and New York, NY, USA: Cambridge University Press, 2013, p. 1535.

[4] F. D. Santos, P. L. Ferreira, and J. S. T. Pedersen, “The climate change challenge: A review of the barriers and solutions to deliver a Paris solution,” *Climate*, vol. 10, no. 5, p. 75, 2022.

[5] W. J. Ripple et al., “The 2024 state of the climate report: Perilous times on planet Earth,” *BioScience*, vol. 74, no. 12, pp. 812–824, 2024.

[6] United Nations Framework Convention on Climate Change, “Paris agreement,” in *Report of the Conference of the Parties to the United Nations Framework Convention on Climate Change (21st Session, 2015: Paris)*, HeinOnline, vol. 4, 2015, p. 2.

[7] N. Zehtabiyan-Rezaie and M. Abkar, “An extended k–ε model for wake-flow simulation of wind farms,” *Renewable Energy*, vol. 222, p. 119 904, 2024.

[8] L. J. Vermeer, J. N. Sørensen, and A. Crespo, “Wind turbine wake aerodynamics,” *Progress in Aerospace Sciences*, vol. 39, no. 6–7, pp. 467–510, 2003.

[9] K. S. Hansen, “Presentation of Lillgrund offshore wind farm and the Siemens SWT-2.3-93 wind turbine,” *Siemens: Munich, Germany*, 2013.

[10] J. Annoni, P. Gebraad, and P. Seiler, “Wind farm flow modeling using an input-output reduced-order model,” in *2016 American Control Conference (ACC)*, IEEE, 2016, pp. 506–512.

[11] M. P. van der Laan et al., “Power curve and wake analyses of the Vestas multi-rotor demonstrator,” *Wind Energy Science*, vol. 4, no. 2, pp. 251–271, 2019.

[12] N. Zehtabiyan-Rezaie and M. Abkar, “A short note on turbulence characteristics in wind-turbine wakes,” *Journal of Wind Engineering and Industrial Aerodynamics*, vol. 240, p. 105 504, 2023.

[13] S. D. Hornshøj-Møller et al., “Quantifying structural uncertainties in Reynolds-averaged Navier–Stokes simulations of wind turbine wakes,” *Renewable Energy*, vol. 164, pp. 1550–1558, 2021. DOI: 10.1016/j.renene.2020.10.148.

[14] M. P. van der Laan et al., “An improved k–ε model applied to a wind turbine wake in atmospheric turbulence,” *Wind Energy*, vol. 18, no. 5, pp. 889–907, 2015. DOI: 10.1002/we.1736.

[15] J. F. Ainslie, “Calculating the flowfield in the wake of wind turbines,” *Journal of Wind Engineering and Industrial Aerodynamics*, vol. 27, no. 1, pp. 213–224, 1988. DOI: 10.1016/0167-6105(88)90037-2.

[16] J. Paddeu, “Finite element method for wind turbine wake modelling,” M.S. thesis, Delft University of Technology, 2024.

[17] C. Bak et al., “The DTU 10-MW reference wind turbine,” Technical University of Denmark (DTU), Tech. Rep., 2013. [Online]. Available: https://orbit.dtu.dk/en/publications/the-dtu-10-mw-reference-wind-turbine.

[18] V. Moureau and G. Lartigue, *YALES2*, https://www.coria-cfd.fr/index.php/YALES2, Accessed: 2025, 2023.

[19] S. B. Pope, *Turbulent Flows*. Cambridge: Cambridge University Press, 2000.

[20] A. N. Kolmogorov, “The local structure of turbulence in incompressible viscous fluid for very large Reynolds numbers,” *Dokl. Akad. Nauk SSSR*, vol. 30, pp. 301–305, 1941.

[21] L. A. Martínez-Tossas, M. J. Churchfield, and S. Leonardi, “Large eddy simulations of the flow past wind turbines: Actuator line and disk modeling,” *Wind Energy*, vol. 18, no. 6, pp. 1047–1060, 2015. DOI: 10.1002/we.1747.

[22] J. Boussinesq, *Essai sur la théorie des eaux courantes*. Paris: Impr. nationale, 1877.

[23] A. N. Kolmogorov, “Equations of turbulent motion in an incompressible fluid,” in *Dokl. Akad. Nauk SSSR*, vol. 30, 1941, pp. 299–303.

[24] D. C. Wilcox, *Turbulence Modeling for CFD*, 3rd. La Cañada, CA: DCW Industries, 2006.

[25] W. P. Jones and B. E. Launder, “The prediction of laminarization with a two-equation model of turbulence,” *International Journal of Heat and Mass Transfer*, vol. 15, no. 2, pp. 301–314, 1972.

[26] B. E. Launder and B. I. Sharma, “Application of the energy-dissipation model of turbulence to the calculation of flow near a spinning disc,” *Letters in Heat and Mass Transfer*, vol. 1, no. 2, pp. 131–137, 1974.

[27] P. Knabner and L. Angermann, *Numerical Methods for Elliptic and Parabolic Partial Differential Equations*. New York: Springer, 2003.

[28] S. G. Rubin and J. C. Tannehill, “Parabolized/reduced Navier–Stokes computational techniques,” *Annual Review of Fluid Mechanics*, vol. 24, pp. 117–144, 1992. DOI: 10.1146/annurev.fl.24.010192.001001.

[29] J. F. Thompson, “Conservation properties and numerical accuracy of parabolic Navier–Stokes formulations,” NASA, Tech. Rep., 1991.

[30] A. Mittal, “A parabolized Navier–Stokes method for wind farm applications,” M.S. thesis, University of Tennessee at Chattanooga, 2015.

[31] A. Mittal, “A parabolic velocity-decomposition method for wind turbines,” *Journal of Computational Physics*, vol. 330, pp. 650–666, 2017.

[32] D. Cabezón, E. Migoya, and A. Crespo, “A semi-parabolic wake model for large offshore wind farms based on the open source CFD solver OpenFOAM,” in *ITM Web of Conferences*, EDP Sciences, vol. 6, 2014, p. 06 002.

[33] International Electrotechnical Commission, *IEC 61400-1 Ed. 4: Wind Turbine Generator Systems—Part 1: Design Requirements*. Geneva: International Electrotechnical Commission, 2019.

[34] T. J. Larsen et al., “Validation of the dynamic wake meander model for loads and power production in the Egmond aan Zee wind farm,” *Wind Energy*, vol. 16, no. 4, pp. 605–624, 2013.

[35] P. S. Bernard and J. M. Wallace, *Turbulent Flow: Analysis, Measurement, and Prediction*. Hoboken, NJ: John Wiley & Sons, 2002.

[36] P.-E. Réthoré, “Wind turbine wake in atmospheric turbulence,” Ph.D. dissertation, Risø National Laboratory for Sustainable Energy, 2009.

[37] L. Prandtl, “Über die ausgebildete Turbulenz,” *Z. Angew. Math. Mech.*, vol. 5, pp. 136–139, 1925.

[38] L. Prandtl, *Über ein neues Formelsystem für die ausgebildete Turbulenz*. Göttingen: Vandenhoeck & Ruprecht, 1945.

[39] P. R. Spalart and S. R. Allmaras, “A one-equation turbulence model for aerodynamic flows,” in *30th Aerospace Sciences Meeting and Exhibit*, 1992, p. 439.

[40] D. C. Wilcox, “Formulation of the k–ω turbulence model revisited,” *AIAA Journal*, vol. 46, no. 11, pp. 2823–2838, 2008.

[41] M. P. van der Laan and S. J. Andersen, “The turbulence scales of a wind turbine wake: A revisit of extended k–ε models,” in *Journal of Physics: Conference Series*, IOP Publishing, vol. 1037, 2018, p. 072 001.

[42] D. Cabezón, E. Migoya, and A. Crespo, “Comparison of turbulence models for the computational fluid dynamics simulation of wind turbine wakes in the atmospheric boundary layer,” *Wind Energy*, vol. 14, no. 7, pp. 909–921, 2011.

[43] L. Tian et al., “Effects of turbulence modelling in AD/RANS simulations of single wind and tidal turbine wakes and double wake interactions,” *Energy*, vol. 208, p. 118 440, 2020. DOI: 10.1016/j.energy.2020.118440.

[44] U. Schumann, “Realizability of Reynolds-stress turbulence models,” *The Physics of Fluids*, vol. 20, no. 5, pp. 721–725, 1977.

[45] B. E. Launder, G. J. Reece, and W. Rodi, “Progress in the development of a Reynolds-stress turbulence closure,” *Journal of Fluid Mechanics*, vol. 68, no. 3, pp. 537–566, 1975.

[46] M. P. van der Laan, “Efficient turbulence modeling for CFD wake simulations,” Ph.D. dissertation, Technical University of Denmark, 2014.

[47] W. Rodi, “A new algebraic relation for calculating the Reynolds stresses,” in *Gesellschaft Angewandte Mathematik und Mechanik Workshop*, vol. 56, Paris, France, 1976, pp. 219–221.

[48] S. B. Pope, “A more general effective-viscosity hypothesis,” *Journal of Fluid Mechanics*, vol. 72, no. 2, pp. 331–340, 1975.

[49] D. D. Apsley and M. A. Leschziner, “A new low-Reynolds-number nonlinear two-equation turbulence model for complex flows,” *International Journal of Heat and Fluid Flow*, vol. 19, no. 3, pp. 209–222, 1998.

[50] M. P. van der Laan et al., “Nonlinear eddy viscosity models applied to wind turbine wakes,” in *Proceedings of the 2013 International Conference on Aerodynamics of Offshore Wind Energy Systems and Wakes (ICOWES2013)*, Technical University of Denmark, 2013, pp. 514–525.

[51] M. P. van der Laan et al., “The k–ε–f_P model applied to double wind turbine wakes using different actuator disk force methods,” *Wind Energy*, vol. 18, no. 12, pp. 2223–2240, 2015. DOI: 10.1002/we.1804.

[52] A. El Kasmi and C. Masson, “An extended k–ε model for turbulent flow through horizontal-axis wind turbines,” *Journal of Wind Engineering and Industrial Aerodynamics*, vol. 96, no. 1, pp. 103–122, 2008.

[53] Y.-S. Chen and S.-W. Kim, “Computation of turbulent flows using an extended k–ε turbulence closure model,” NASA Marshall Space Flight Center, Tech. Rep. NASA CR-179204, 1987.

[54] J. M. Prospathopoulos et al., “Evaluation of the effects of turbulence model enhancements on wind turbine wake predictions,” *Wind Energy*, vol. 14, no. 2, pp. 285–300, 2011.

[55] P. A. Durbin, “Separated flow computations with the k–ε–$\overline{v^2}$ model,” *AIAA Journal*, vol. 33, no. 4, pp. 659–664, 1995. DOI: 10.2514/3.12628.

[56] I. Reinwardt et al., “Dynamic wake meandering model calibration using nacelle-mounted lidar systems,” *Wind Energy Science*, vol. 5, no. 2, pp. 775–792, 2020.

[57] F. Moukalled, L. Mangani, and M. Darwish, *The Finite Volume Method in Computational Fluid Dynamics: An Advanced Introduction with OpenFOAM and Matlab* (Fluid Mechanics and Its Applications). Cham: Springer, 2016, vol. 113. DOI: 10.1007/978-3-319-16874-6.

[58] P. J. Roache, “Verification of codes and calculations,” *AIAA Journal*, vol. 36, no. 5, pp. 696–702, 1998. DOI: 10.2514/2.457.

[59] R. J. Hyndman and A. B. Koehler, “Another look at measures of forecast accuracy,” *International Journal of Forecasting*, vol. 22, no. 4, pp. 679–688, 2006.

[60] D. K. Lilly, “A proposed modification of the Germano subgrid-scale closure method,” *Physics of Fluids A: Fluid Dynamics*, vol. 4, no. 3, pp. 633–635, 1992.

[61] J. N. Sørensen and W. Z. Shen, “Numerical modeling of wind turbine wakes,” *Journal of Fluids Engineering*, vol. 124, no. 2, pp. 393–399, 2002.

A Error Metrics — Original Model

This appendix summarises error metrics between the FAWM predictions (original model that includes $\partial V/\partial x$) and the LES reference data. Two metrics are reported for each validation case: the mean absolute percentage error (MAPE) and the relative root-mean-square error (RRMSE), defined in **??**. The same three wake regions are used: the near wake ($-2D \leq x < 3D$), the far wake ($3D \leq x < 10D$), and the full wake ($-2D \leq x < 10D$).

Because the original model was less stable than the modified model with $\frac{\partial V}{\partial x}$ neglected in the production term, the number of converged test cases is smaller. The standard k–ε and k–ε–S_k model converged only for Configurations 3 and 4, and the k–ε–f_P model converged only for Configuration 3.

A.1 Axial Velocity

Table A.1: Error metrics for the axial velocity U in the near wake ($-2D \leq x < 3D$), original model.

	MAPE [%]				RRMSE [%]			
Model	C 1	C 2	C 3	C 4	C 1	C 2	C 3	C 4
Standard k–ε	–	–	9.50	1.78	–	–	14.58	2.93
k–ε–S_k	–	–	9.50	1.67	–	–	14.58	2.72
k–ε–f_P	–	–	4.48	–	–	–	6.88	–

Table A.2: Error metrics for the axial velocity U in the far wake ($3D \leq x < 10D$), original model.

	MAPE [%]				RRMSE [%]			
Model	C 1	C 2	C 3	C 4	C 1	C 2	C 3	C 4
Standard k–ε	–	–	8.88	2.57	–	–	11.51	3.61
k–ε–S_k	–	–	8.88	2.47	–	–	11.51	3.47
k–ε–f_P	–	–	7.70	–	–	–	9.75	–

Table A.3: Error metrics for the axial velocity U over the full wake ($-2D \leq x < 10D$), original model.

	MAPE [%]				RRMSE [%]			
Model	C 1	C 2	C 3	C 4	C 1	C 2	C 3	C 4
Standard k–ε	–	–	9.14	2.24	–	–	12.91	3.34
k–ε–S_k	–	–	9.14	2.13	–	–	12.91	3.17
k–ε–f_P	–	–	6.34	–	–	–	8.65	–

A.2 Turbulent Kinetic Energy

Table A.4: Error metrics for the turbulent kinetic energy k in the near wake ($-2D \leq x < 3D$), original model.

	MAPE [%]				RRMSE [%]			
Model	C 1	C 2	C 3	C 4	C 1	C 2	C 3	C 4
Standard k–ε	–	–	1998.63	29.15	–	–	5068.82	36.08
k–ε–S_k	–	–	2396.25	26.13	–	–	13958.51	32.03
k–ε–f_P	–	–	80.51	–	–	–	117.89	–

Table A.5: Error metrics for the turbulent kinetic energy k in the far wake ($3D \leq x < 10D$), original model.

	MAPE [%]				RRMSE [%]			
Model	C 1	C 2	C 3	C 4	C 1	C 2	C 3	C 4
Standard k–ε	–	–	450.13	157.93	–	–	482.52	158.76
k–ε–S_k	–	–	454.48	151.64	–	–	487.12	152.63
k–ε–f_P	–	–	112.67	–	–	–	117.27	–

Table A.6: Error metrics for the turbulent kinetic energy k over the full wake ($-2D \leq x < 10D$), original model.

	MAPE [%]				RRMSE [%]			
Model	C 1	C 2	C 3	C 4	C 1	C 2	C 3	C 4
Standard k–ε	–	–	1063.25	78.91	–	–	3123.02	87.46
k–ε–S_k	–	–	1223.31	74.63	–	–	8544.15	83.13
k–ε–f_P	–	–	99.94	–	–	–	117.63	–

B Validation Figures — Original Model

This appendix presents contour comparisons for the original FAWM model (including $\partial V/\partial x$) and the YALES2 LES reference data. Because the original model with $\frac{\partial V}{\partial x}$ included in the production term had stability problems, there are only a few available converged cases. The standard k–ε model and the k–ε–S_k model converged for Configurations 3 and 4. The k–ε–f_P model converged only for Configuration 3.

B.1 Axial Velocity

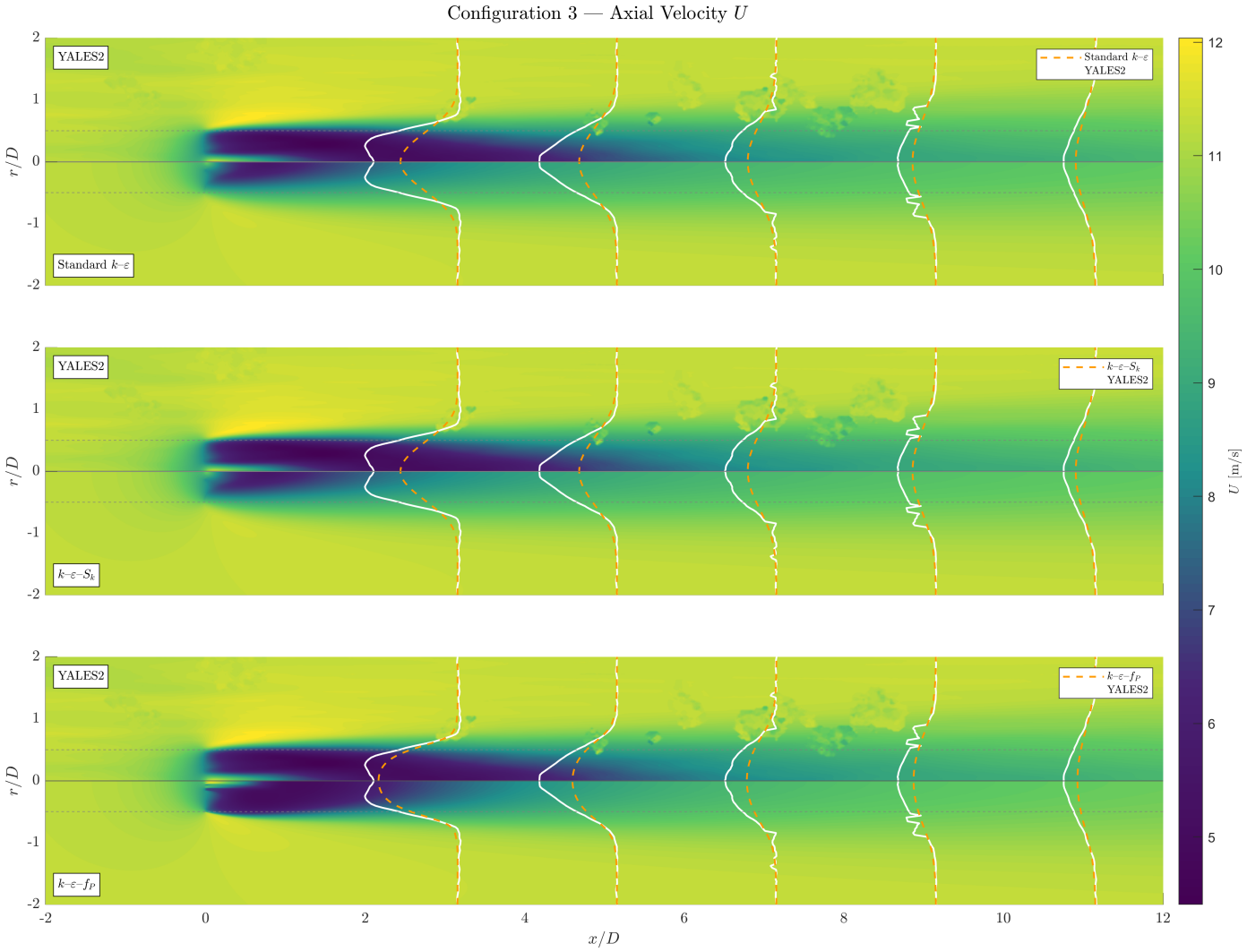

Figure B.1: Axial velocity U for Configuration 3. Upper half: YALES2; lower half: FAWM. Rows correspond to the Standard k–ε, k–ε–S_k, and k–ε–f_P models.

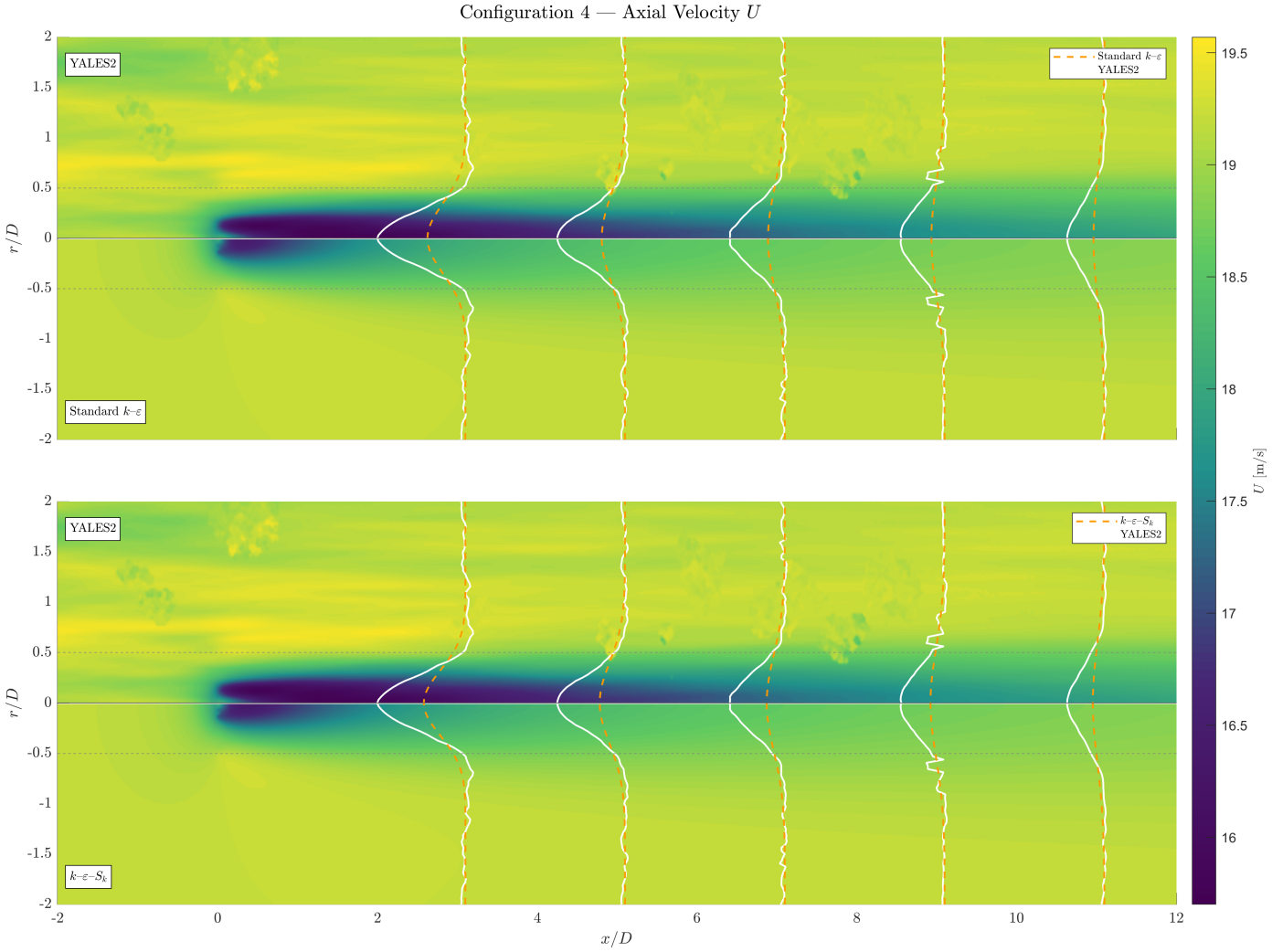

Figure B.2: Axial velocity U for Configuration 4. Upper half: YALES2; lower half: FAWM. Rows correspond to the Standard k–ε and k–ε–S_k models. The k–ε–f_P model did not converge for this configuration.

B.2 Turbulent Kinetic Energy

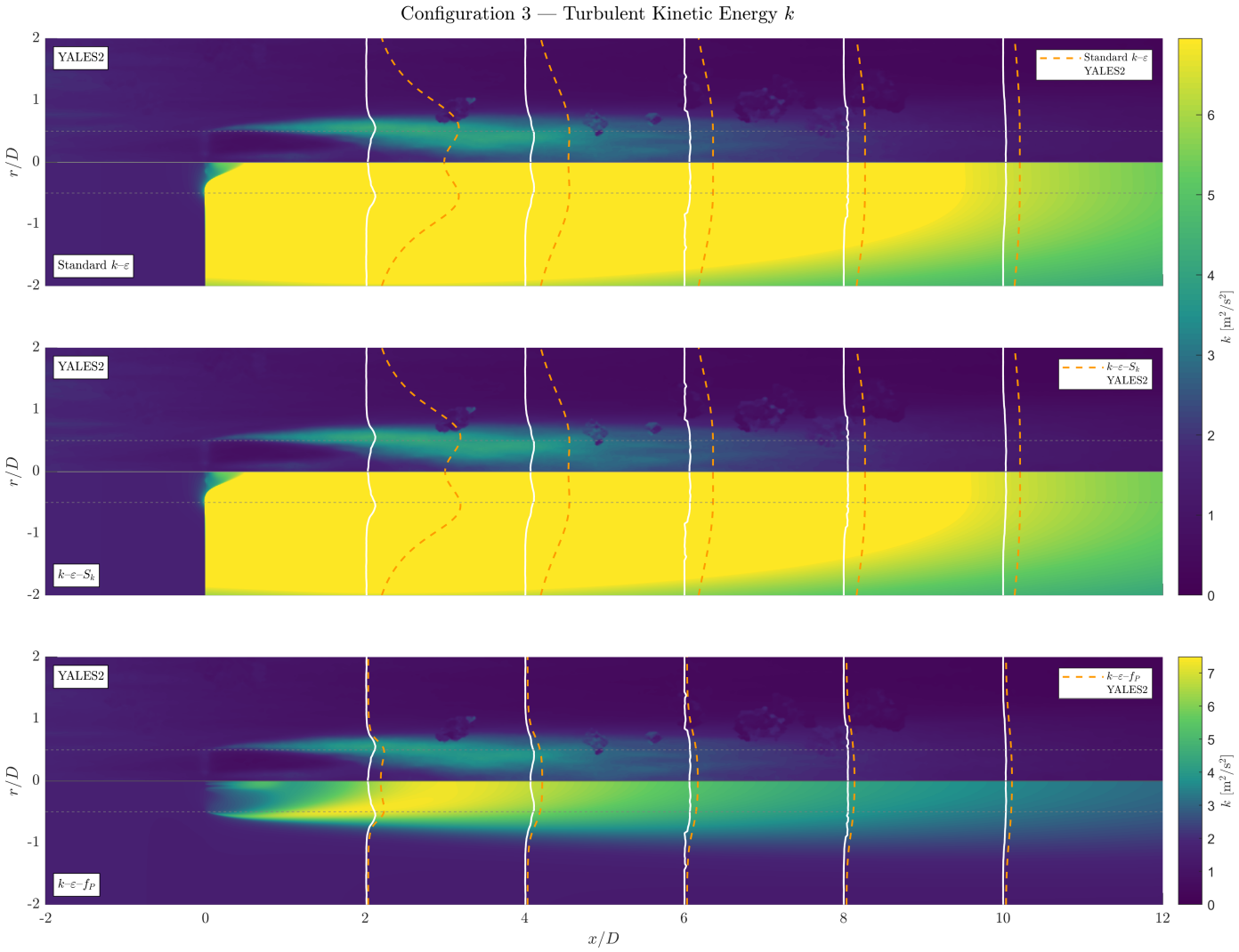

Figure B.3: Turbulent kinetic energy k for Configuration 3. Upper half: YALES2; lower half: FAWM. Rows correspond to the Standard k–ε, k–ε–S_k, and k–ε–f_P models.

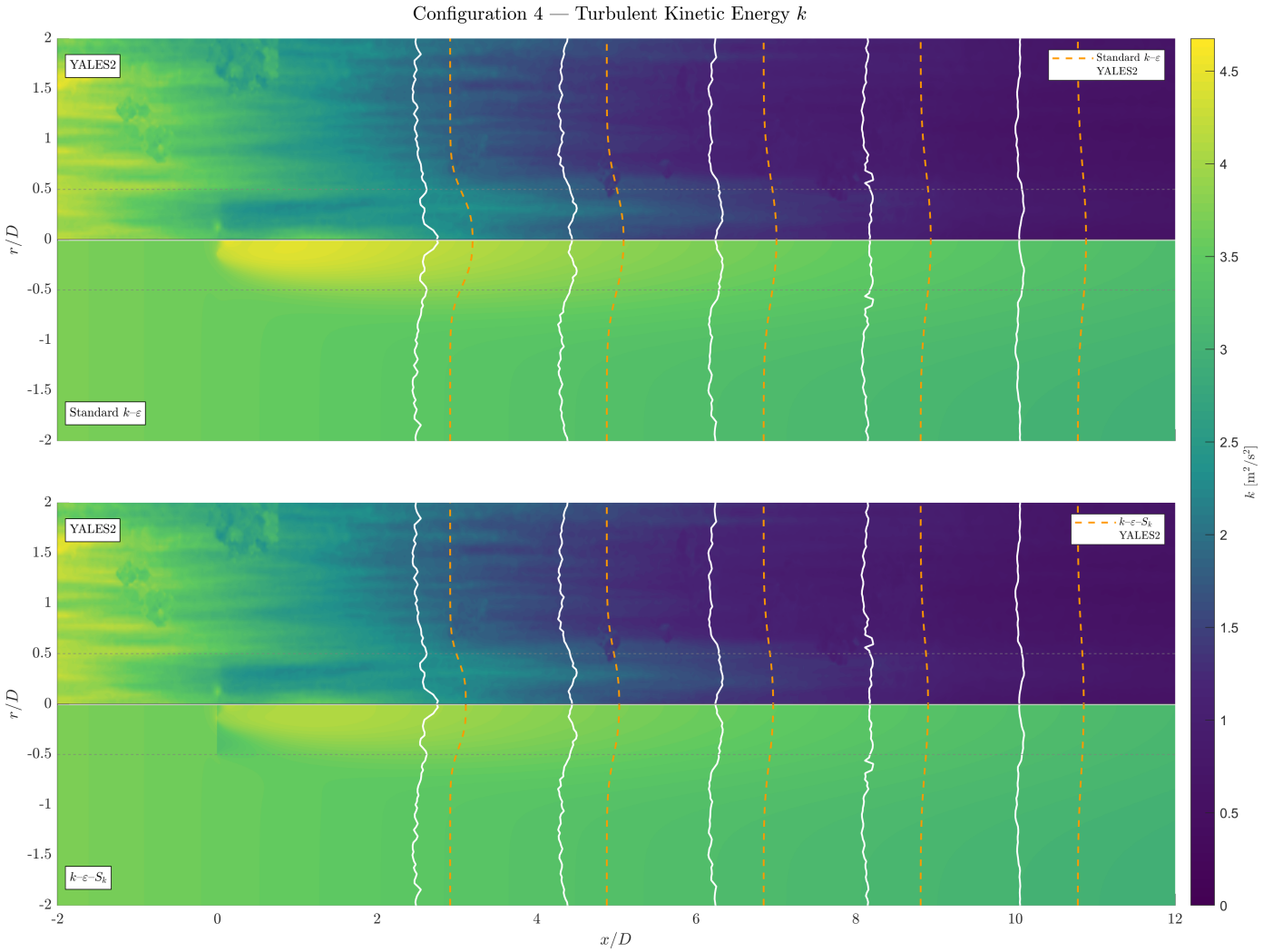

Figure B.4: Turbulent kinetic energy k for Configuration 4. Upper half: YALES2; lower half: FAWM. Rows correspond to the Standard k–ε and k–ε–S_k models. The k–ε–f_P model did not converge for this configuration.

B.3 Eddy Viscosity

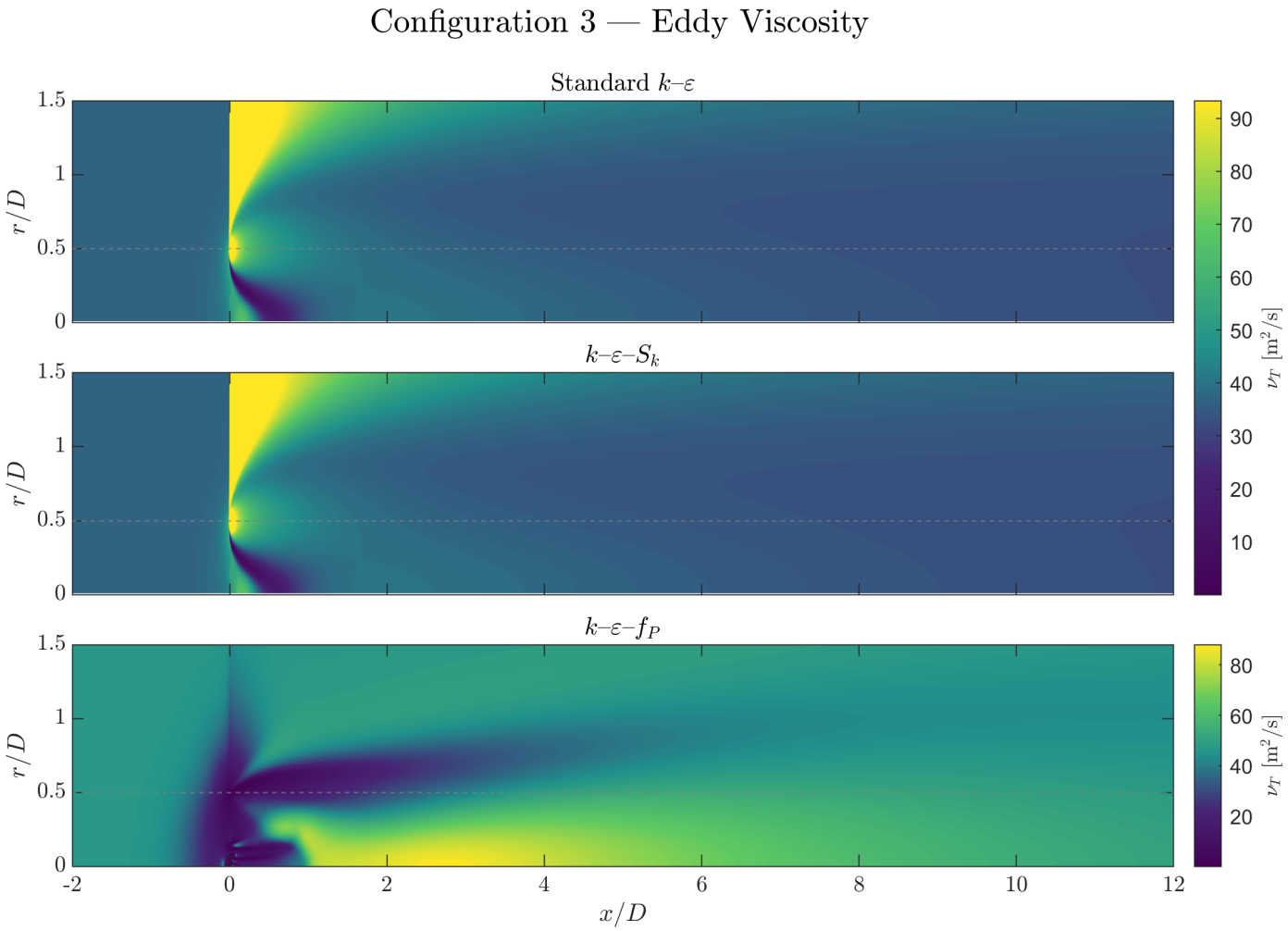

Figure B.5: Eddy viscosity ν_T contours for Configuration 3. Shown are the Standard k–ε, k–ε–S_k, and k–ε–f_P model predictions.

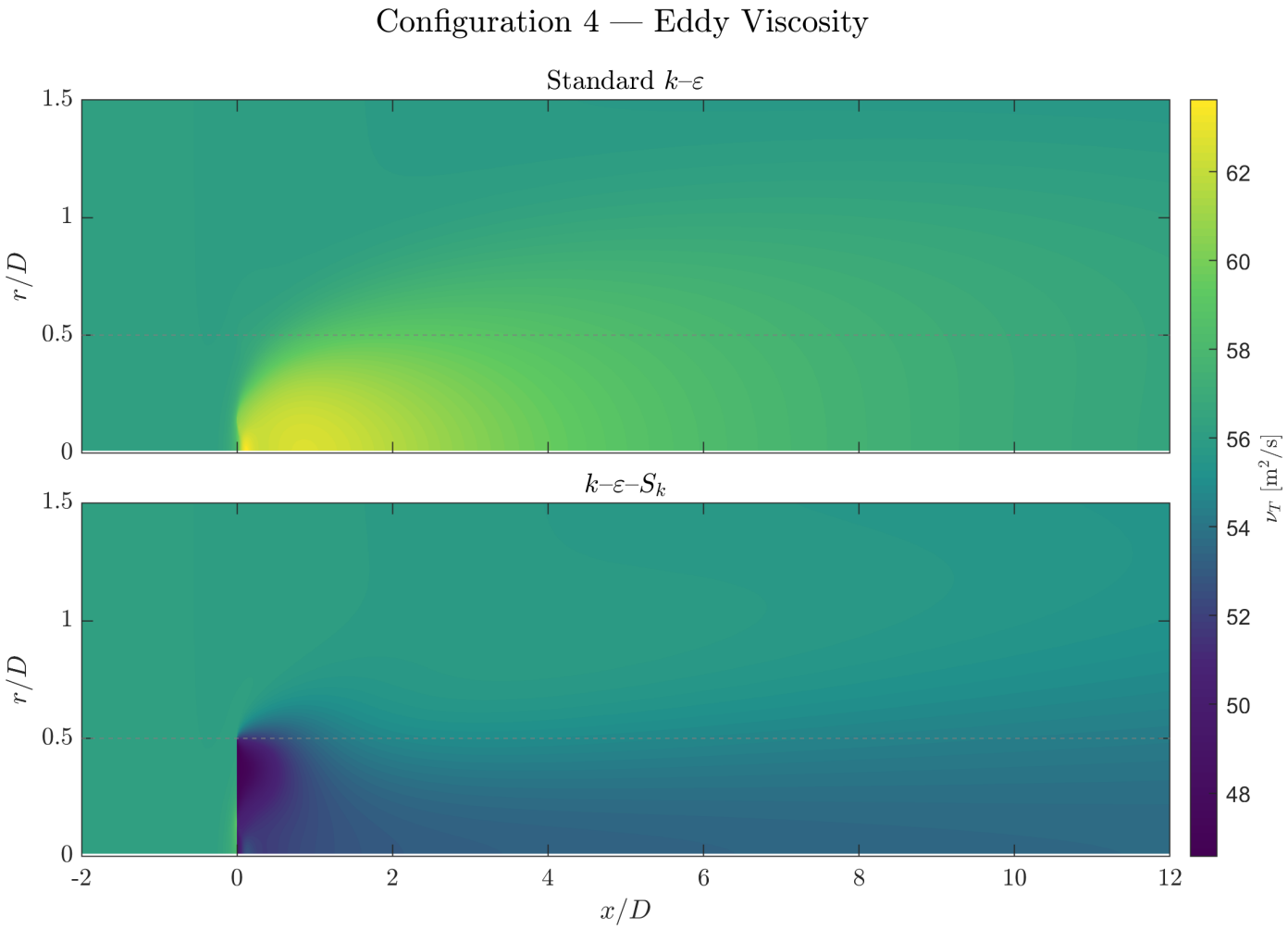

Figure B.6: Eddy viscosity ν_T contours for Configuration 4. Shown are the Standard k–ε and k–ε–S_k model predictions.

B.4 Dissipation Rate

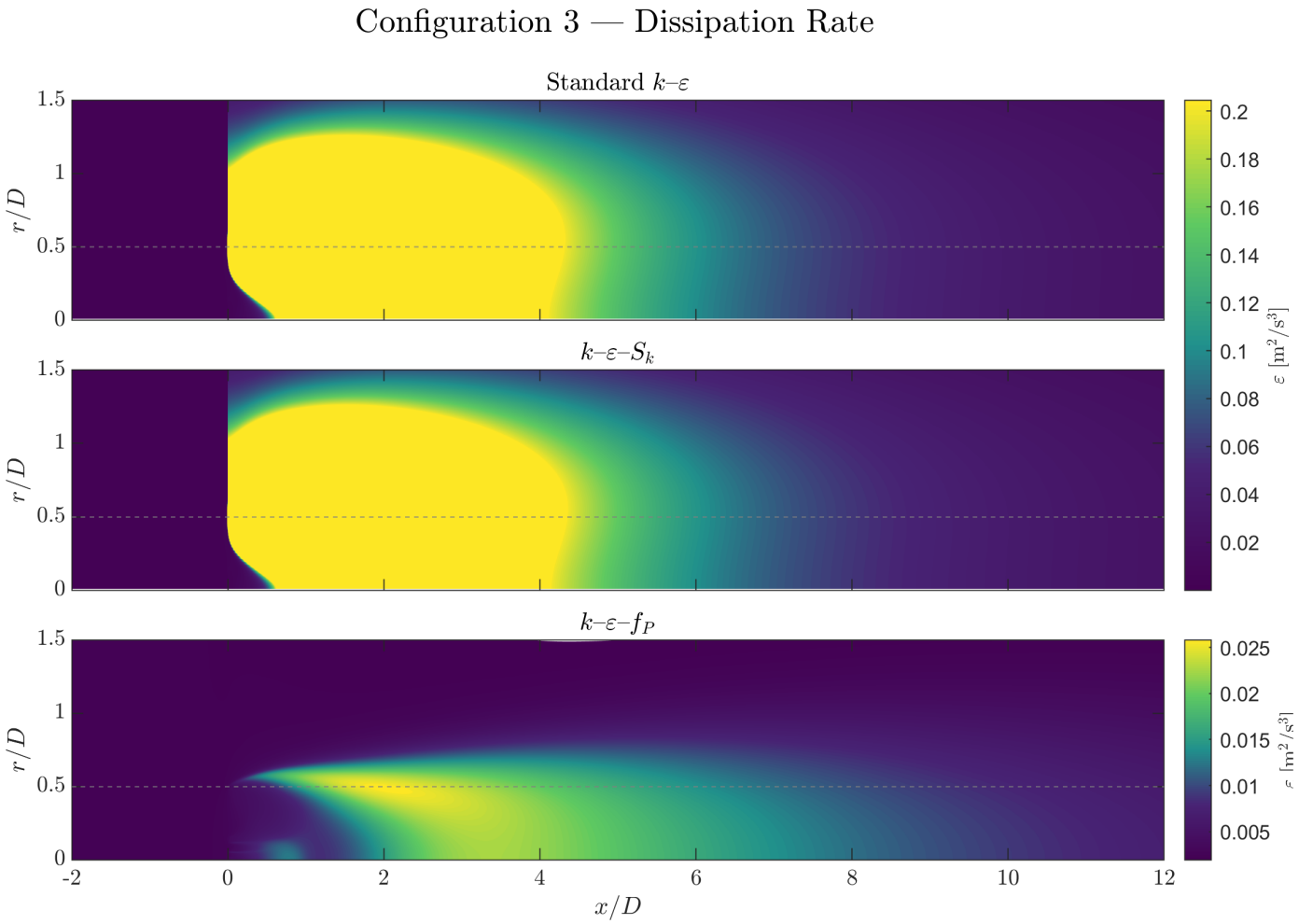

Figure B.7: Dissipation rate ε contours for Configuration 3. Shown are the Standard k–ε, k–ε–S_k, and k–ε–f_P model predictions.

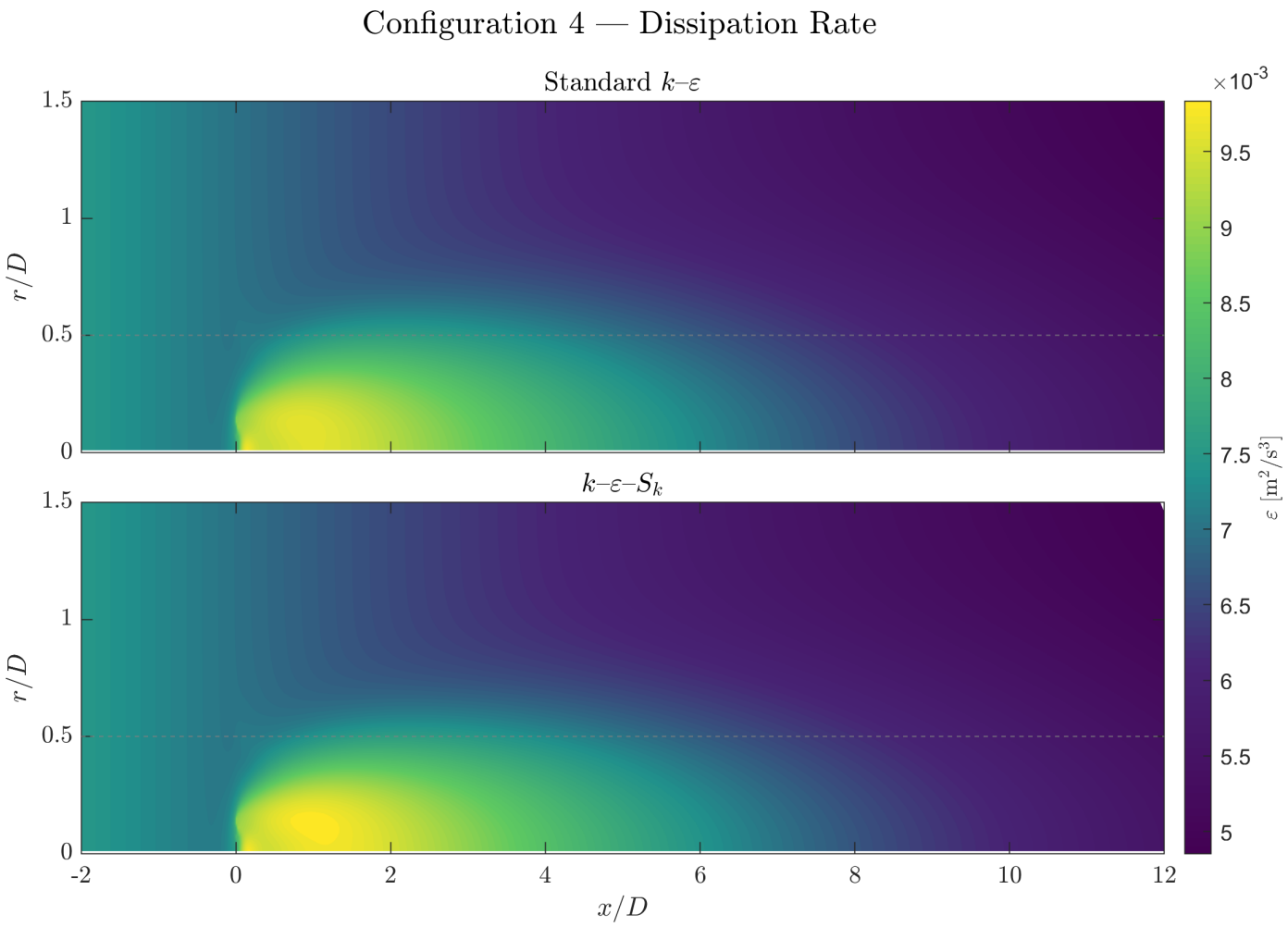

Figure B.8: Dissipation rate ε contours for Configuration 4. Shown are the Standard k–ε and k–ε–S_k model predictions.

C Error Metrics — $\partial V/\partial x$ Neglected

This appendix the error metrics between the FAWM predictions, with $\partial V/\partial x$ neglected in the production term, and the LES data.

C.1 Axial Velocity

Table C.1: Error metrics for the axial velocity U in the near wake ($-2D \leq x < 3D$), $\partial V/\partial x$ neglected.

	MAPE [%]				RRMSE [%]			
Model	C 1	C 2	C 3	C 4	C 1	C 2	C 3	C 4
Standard k–ε	11.03	9.61	9.20	1.55	16.57	14.87	14.36	2.48
k–ε–S_k	7.51	6.18	5.70	1.44	11.15	9.28	8.59	2.26
k–ε–f_P	–	3.64	3.66	1.11	–	5.36	5.41	1.55

Table C.2: Error metrics for the axial velocity U in the far wake ($3D \leq x < 10D$), $\partial V/\partial x$ neglected.

	MAPE [%]				RRMSE [%]			
Model	C 1	C 2	C 3	C 4	C 1	C 2	C 3	C 4
Standard k–ε	11.67	9.48	9.12	2.21	14.66	12.82	12.01	3.11
k–ε–S_k	7.20	4.43	4.21	2.08	8.92	6.56	5.85	2.92
k–ε–f_P	–	4.85	5.22	1.99	–	6.52	6.78	2.77

Table C.3: Error metrics for the axial velocity U over the full wake ($-2D \leq x < 10D$), $\partial V/\partial x$ neglected.

	MAPE [%]				RRMSE [%]			
Model	C 1	C 2	C 3	C 4	C 1	C 2	C 3	C 4
Standard k–ε	11.40	9.53	9.16	1.93	15.50	13.73	13.06	2.86
k–ε–S_k	7.33	5.17	4.84	1.81	9.94	7.83	7.14	2.66
k–ε–f_P	–	4.34	4.56	1.62	–	6.06	6.24	2.33

C.2 Turbulent Kinetic Energy

Table C.4: Error metrics for the turbulent kinetic energy k in the near wake ($-2D \leq x < 3D$), $\partial V/\partial x$ neglected.

	MAPE [%]				RRMSE [%]			
Model	C 1	C 2	C 3	C 4	C 1	C 2	C 3	C 4
Standard k–ε	98.14	113.29	89.78	22.92	132.65	163.86	127.21	25.75
k–ε–S_k	53.01	64.50	48.61	21.03	67.89	93.99	67.36	24.00
k–ε–f_P	–	70.91	62.90	21.72	–	106.12	89.38	24.89

Table C.5: Error metrics for the turbulent kinetic energy k in the far wake ($3D \leq x < 10D$), $\partial V/\partial x$ neglected.

	MAPE [%]				RRMSE [%]			
Model	C 1	C 2	C 3	C 4	C 1	C 2	C 3	C 4
Standard k–ε	156.69	73.54	70.46	101.52	158.54	75.74	73.15	103.20
k–ε–S_k	119.43	54.22	49.82	96.09	120.11	56.44	52.22	97.97
k–ε–f_P	–	104.51	95.98	102.49	–	111.38	101.70	104.30

Table C.6: Error metrics for the turbulent kinetic energy k over the full wake ($-2D \leq x < 10D$), $\partial V/\partial x$ neglected.

	MAPE [%]				RRMSE [%]			
Model	C 1	C 2	C 3	C 4	C 1	C 2	C 3	C 4
Standard k–ε	126.41	87.63	78.11	53.29	146.00	110.29	97.02	57.74
k–ε–S_k	85.07	57.86	49.34	50.04	93.44	70.24	58.39	54.64
k–ε–f_P	–	92.60	82.88	52.93	–	110.80	97.39	57.91

D Validation Figures — $\partial V/\partial x$ Neglected

This appendix shows the contour plots of the FAWM predictions by the modified model, where $\frac{\partial V}{\partial x}$ is neglected in the production term.

D.1 Axial Velocity

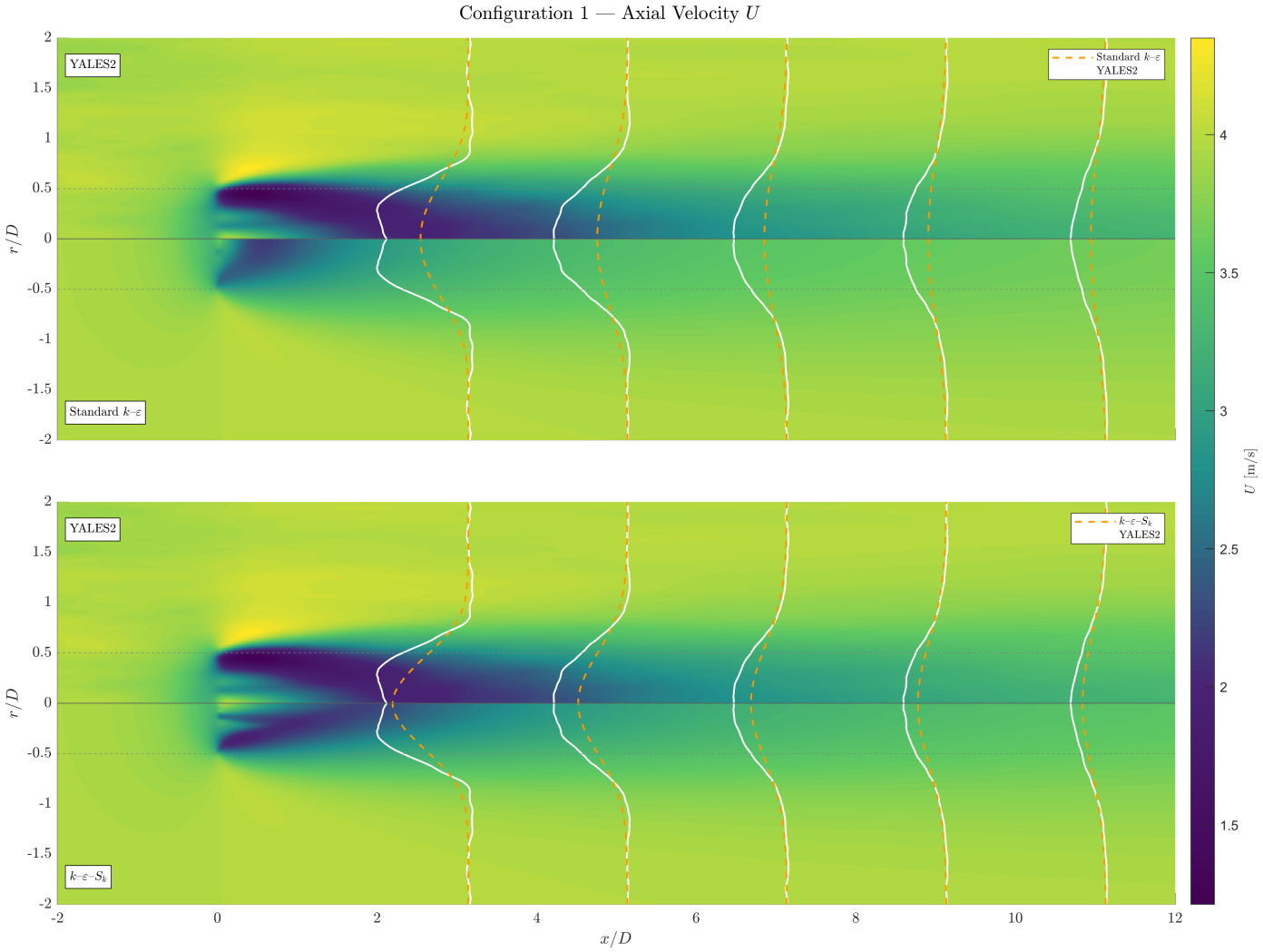

Figure D.1: Axial velocity U for Configuration 1. Upper half: YALES2; lower half: FAWM. Rows correspond to the Standard k–ε and k–ε–S_k models. The k–ε–f_P model did not converge for this configuration.

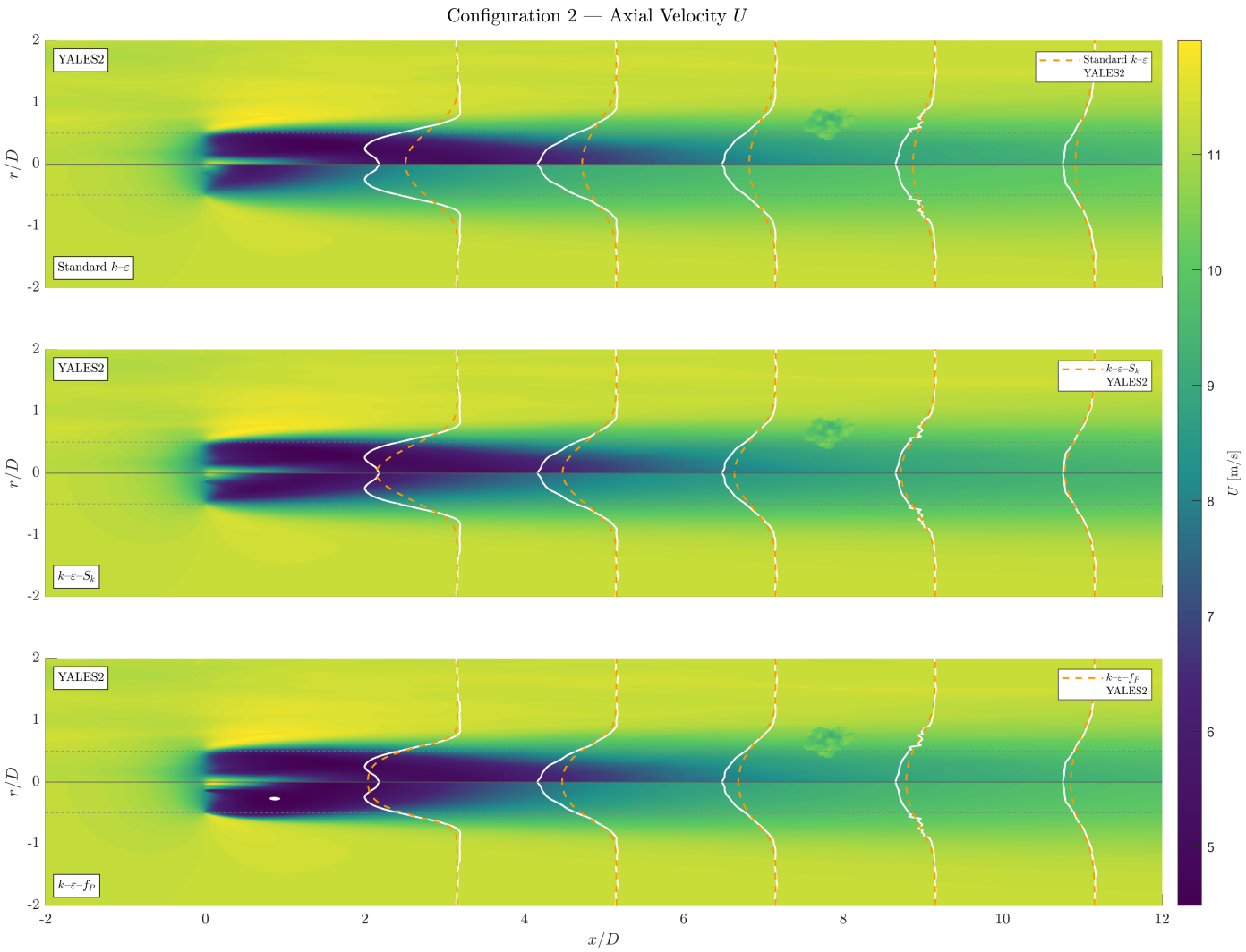

Figure D.2: Axial velocity U for Configuration 2. Upper half: YALES2; lower half: FAWM. Rows correspond to the Standard k–ε, k–ε–S_k, and k–ε–f_P models.

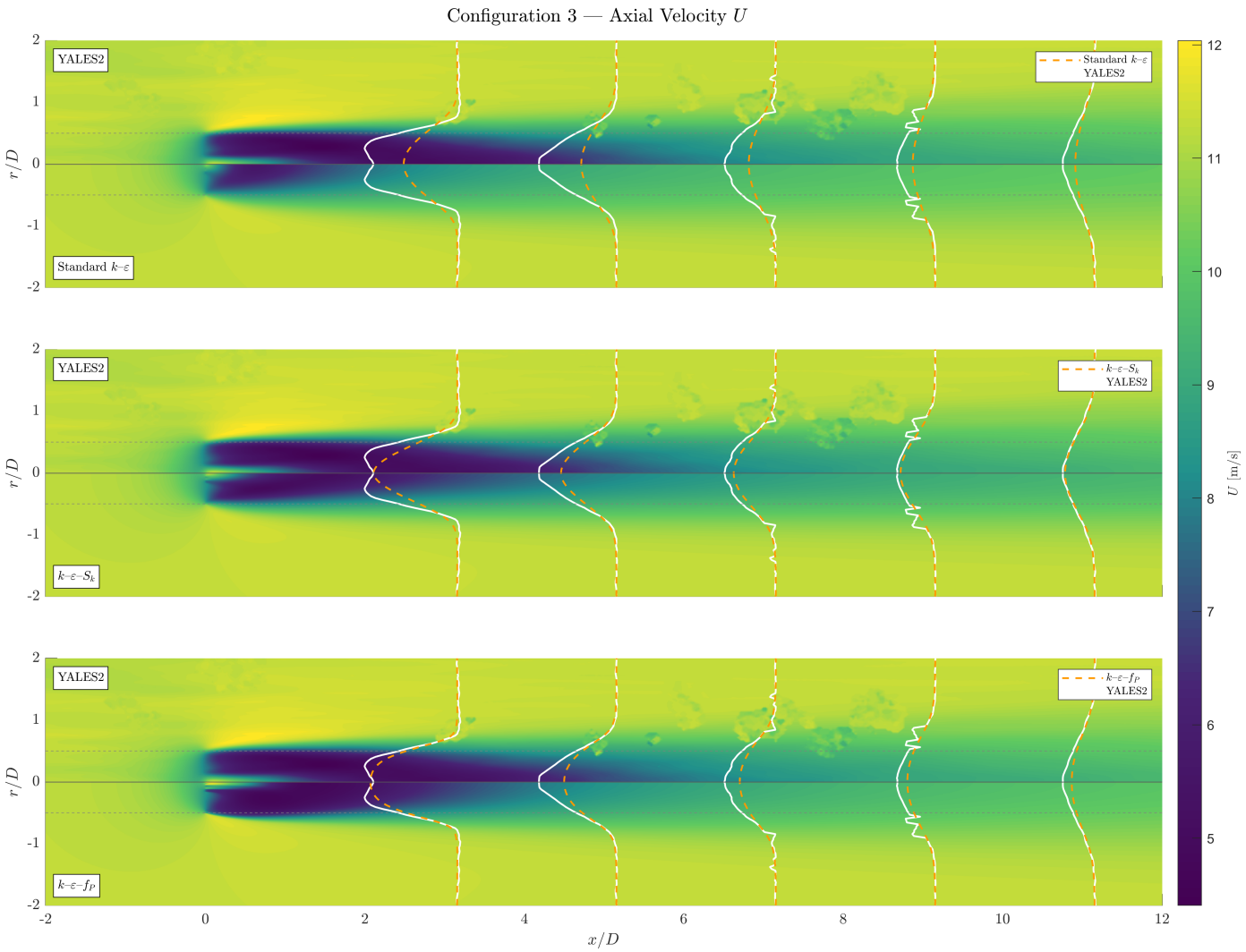

Figure D.3: Axial velocity U for Configuration 3. Upper half: YALES2; lower half: FAWM. Rows correspond to the Standard k–ε, k–ε–S_k, and k–ε–f_P models.

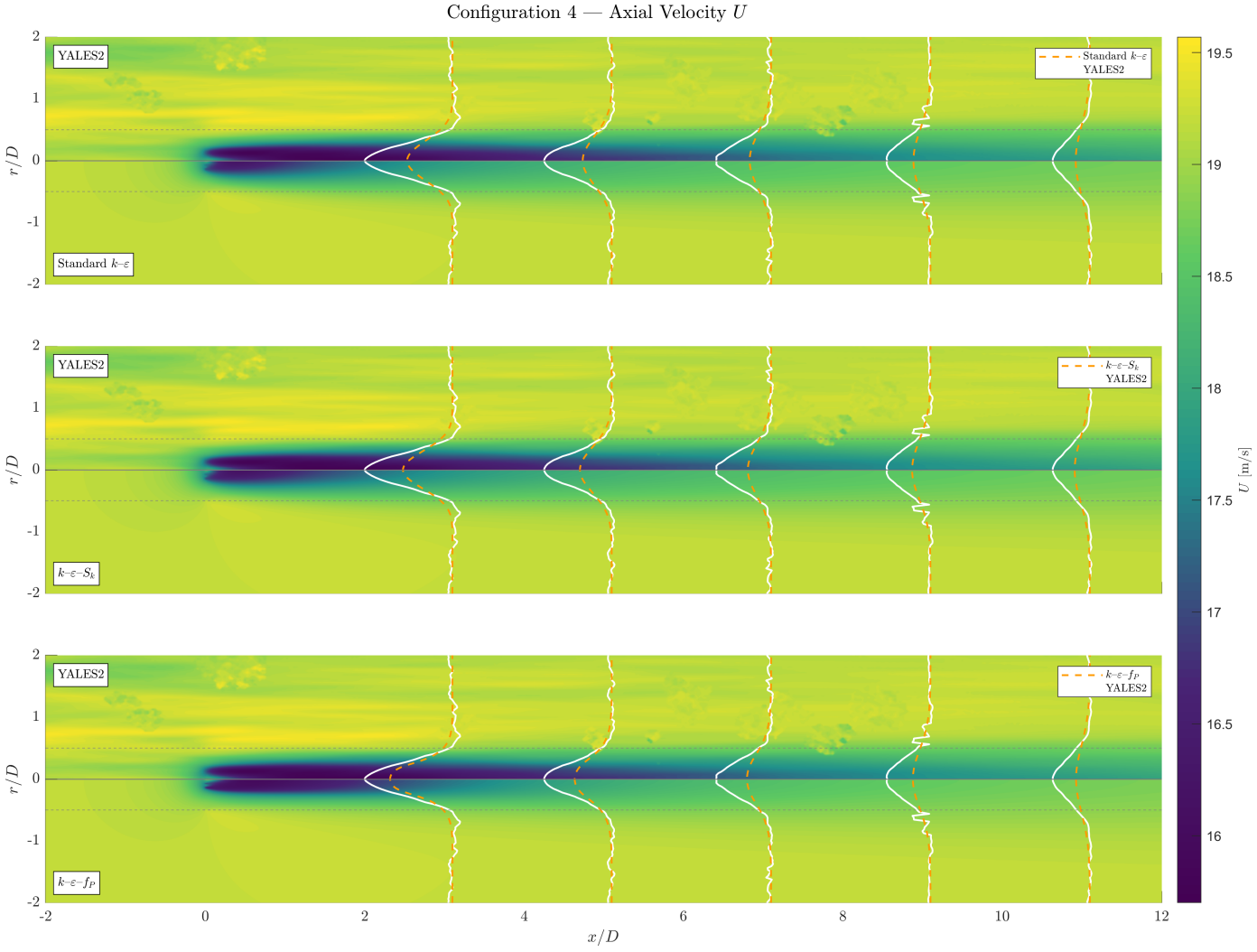

Figure D.4: Axial velocity U for Configuration 4. Upper half: YALES2; lower half: FAWM. Rows correspond to the Standard k–ε, k–ε–S_k, and k–ε–f_P models.

D.2 Turbulent Kinetic Energy

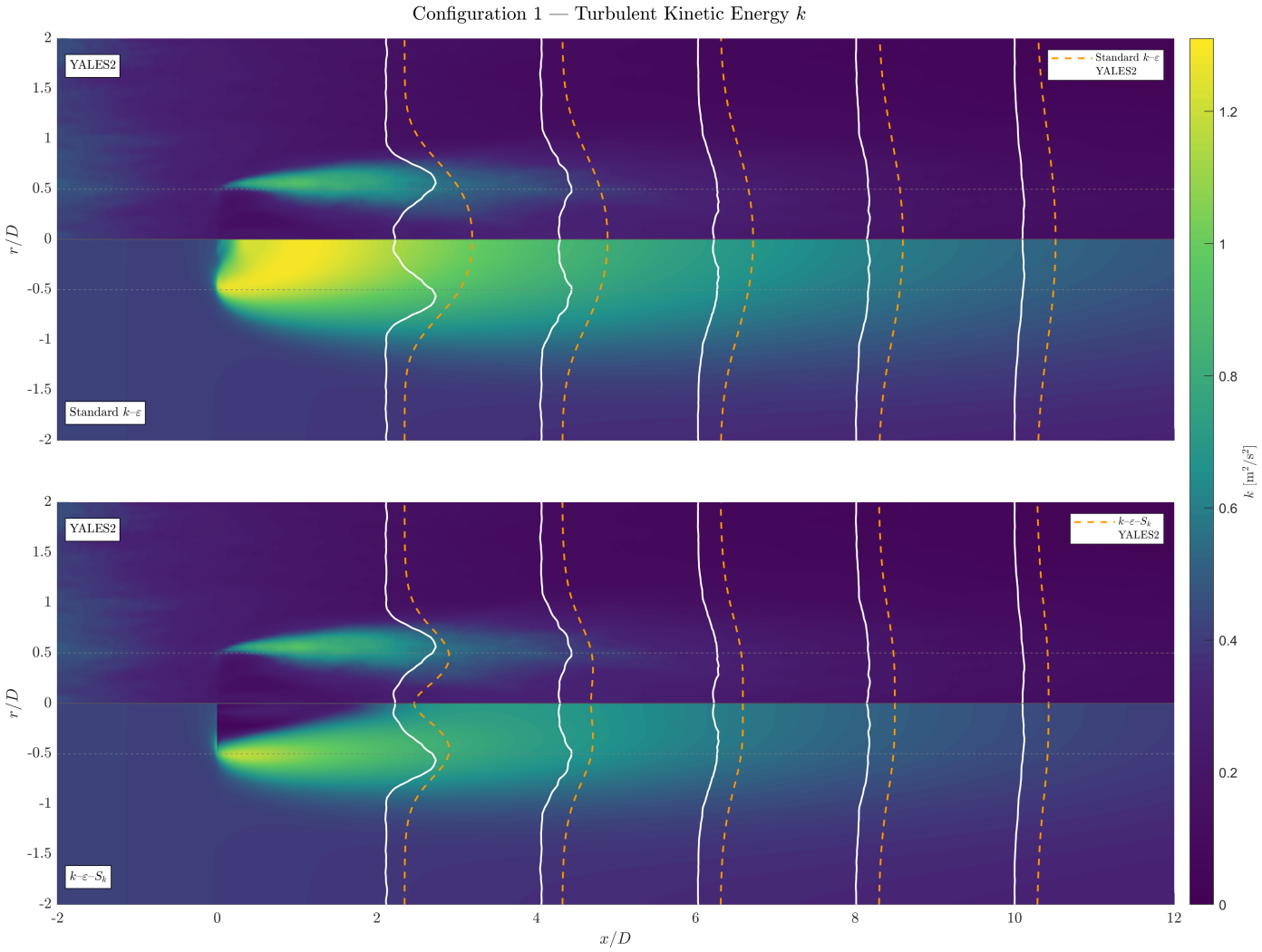

Figure D.5: Turbulent kinetic energy k for Configuration 1. Upper half: YALES2; lower half: FAWM. Rows correspond to the Standard k–ε and k–ε–S_k models. The k–ε–f_P model did not converge for this configuration.

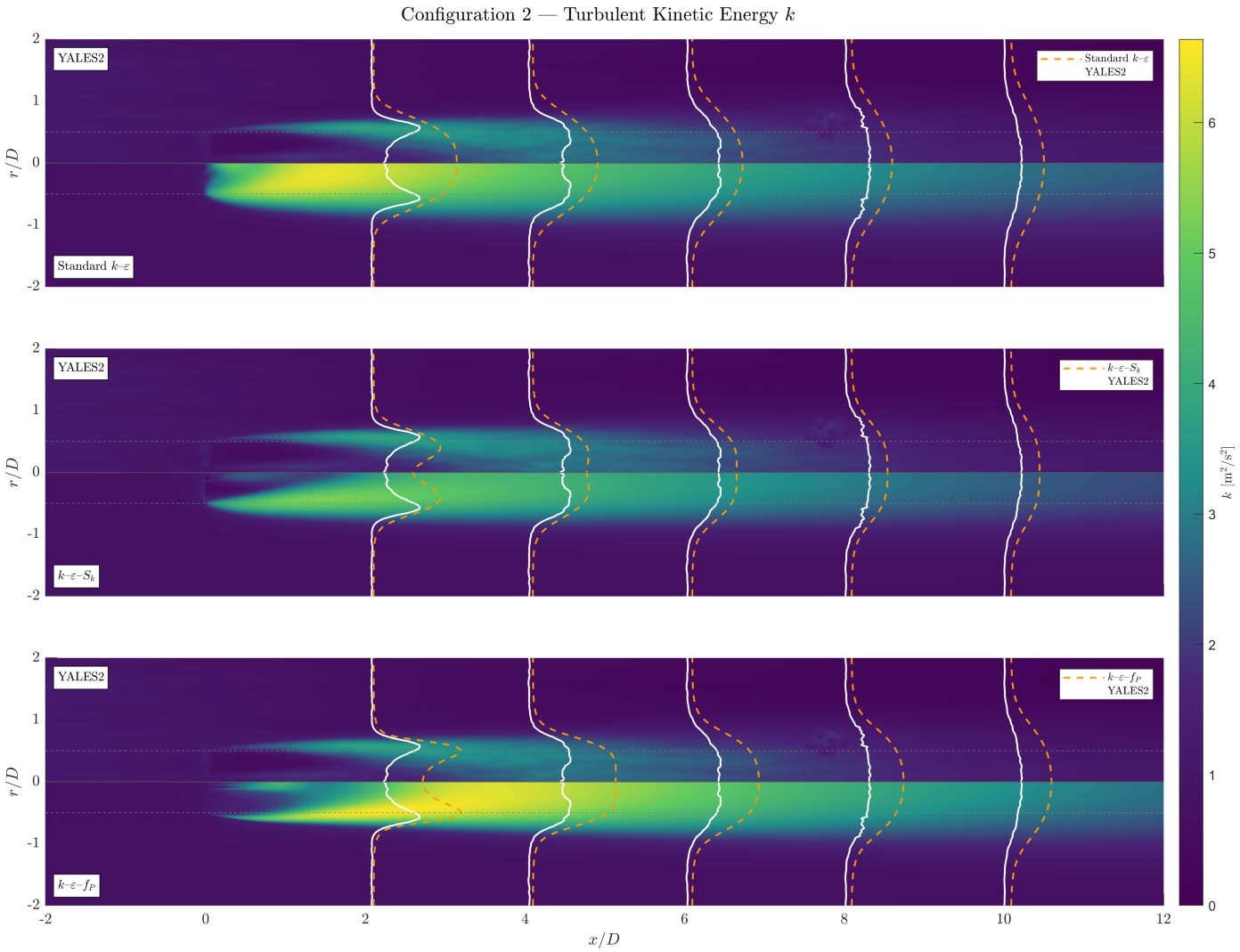

Figure D.6: Turbulent kinetic energy k for Configuration 2. Upper half: YALES2; lower half: FAWM. Rows correspond to the Standard k–ε, k–ε–S_k, and k–ε–f_P models.

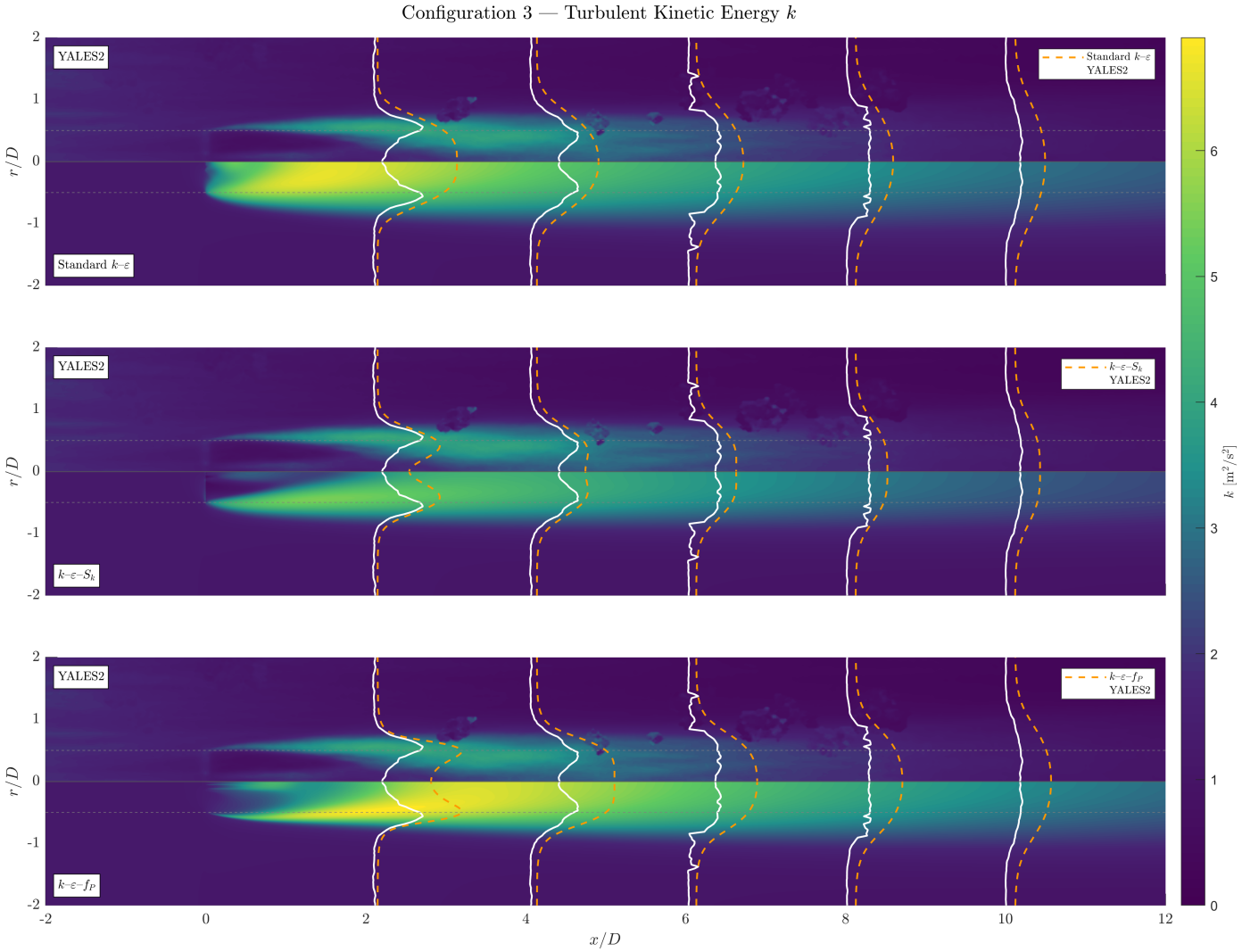

Figure D.7: Turbulent kinetic energy k for Configuration 3. Upper half: YALES2; lower half: FAWM. Rows correspond to the Standard k–ε, k–ε–S_k, and k–ε–f_P models.

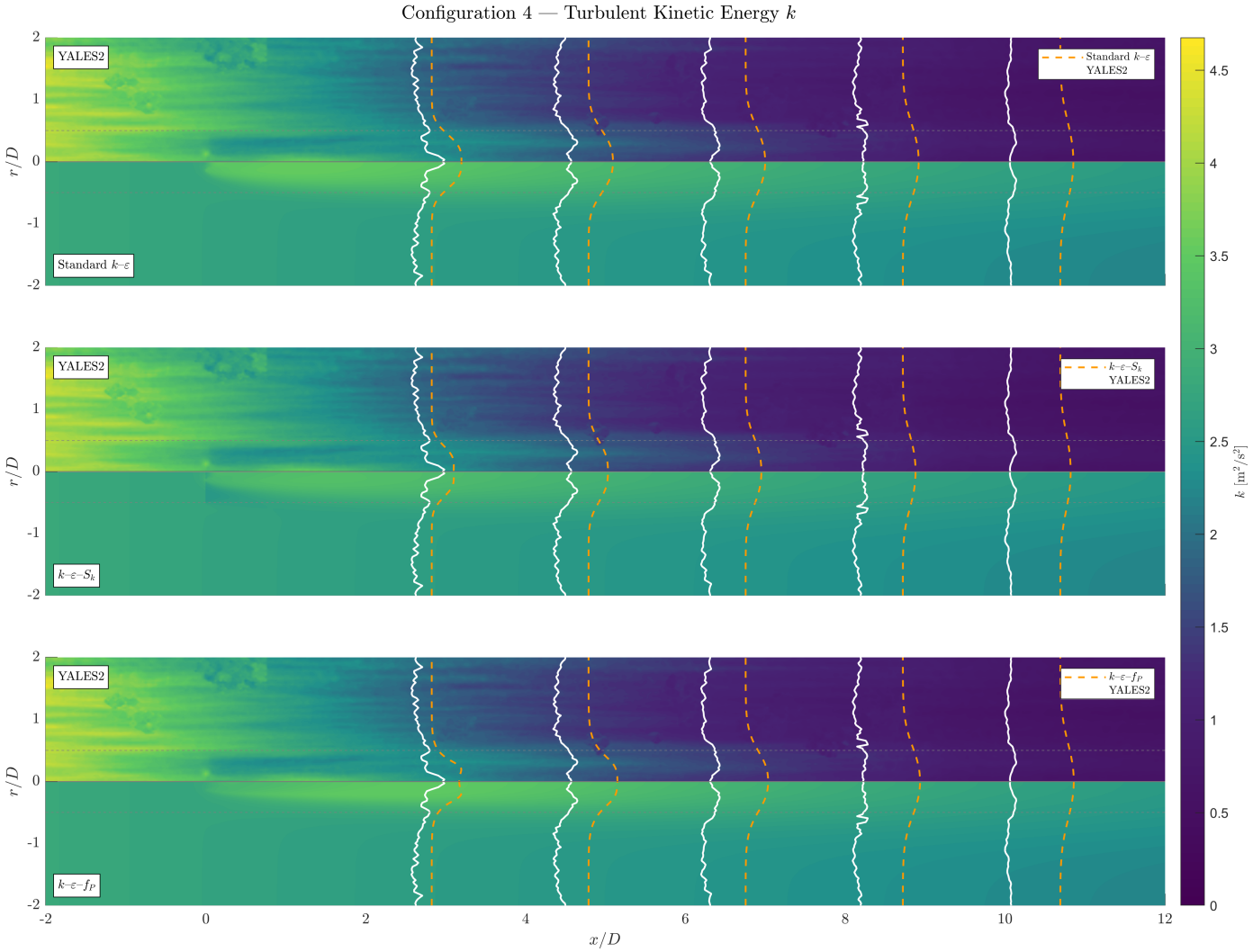

Figure D.8: Turbulent kinetic energy k for Configuration 4. Upper half: YALES2; lower half: FAWM. Rows correspond to the Standard k–ε, k–ε–S_k, and k–ε–f_P models.

D.3 Radial Velocity

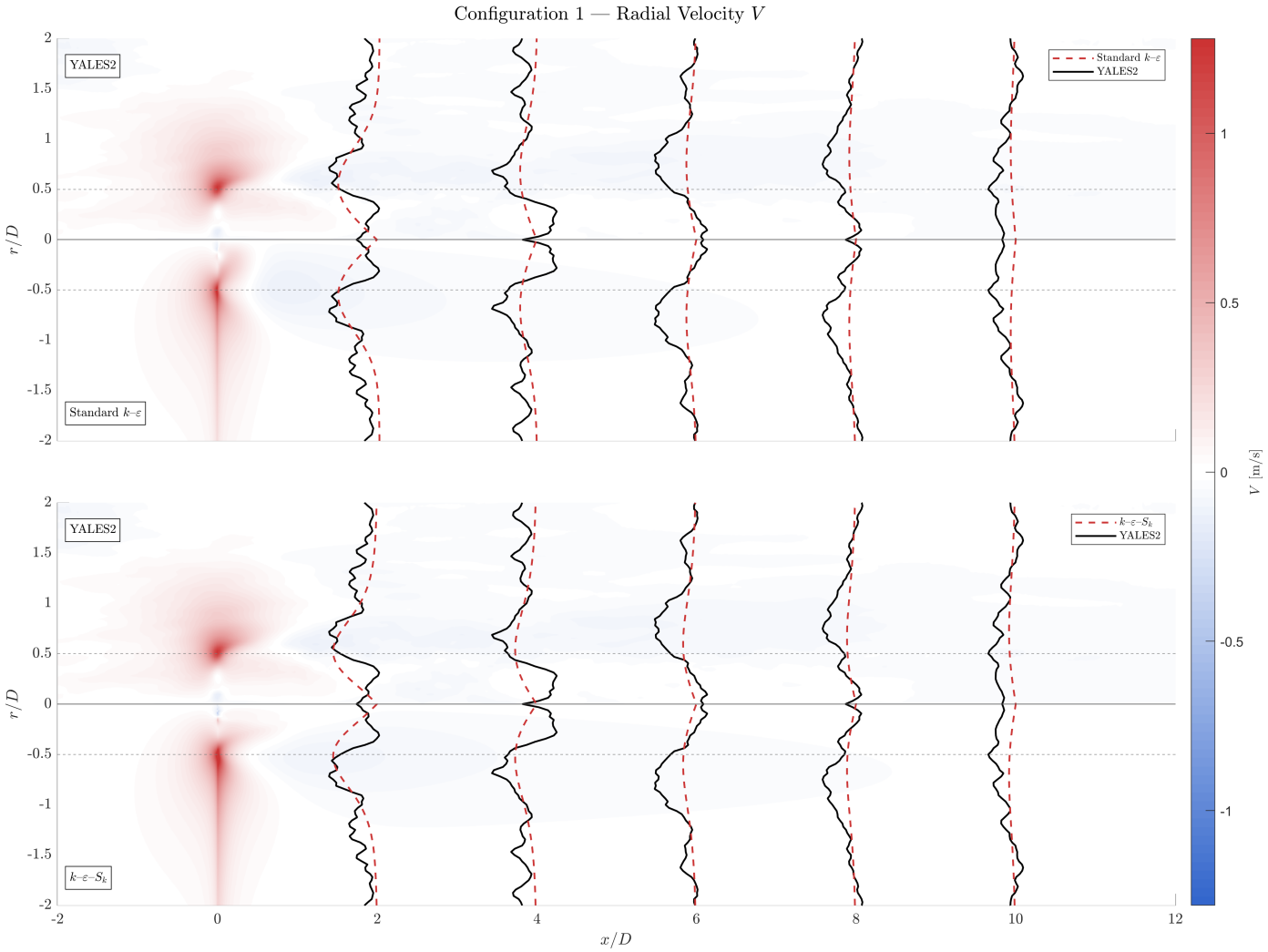

Figure D.9: Radial velocity V for Configuration 1. Upper half: YALES2; lower half: FAWM. Rows correspond to the Standard k–ε and k–ε–S_k models. The k–ε–f_P model did not converge for this configuration.

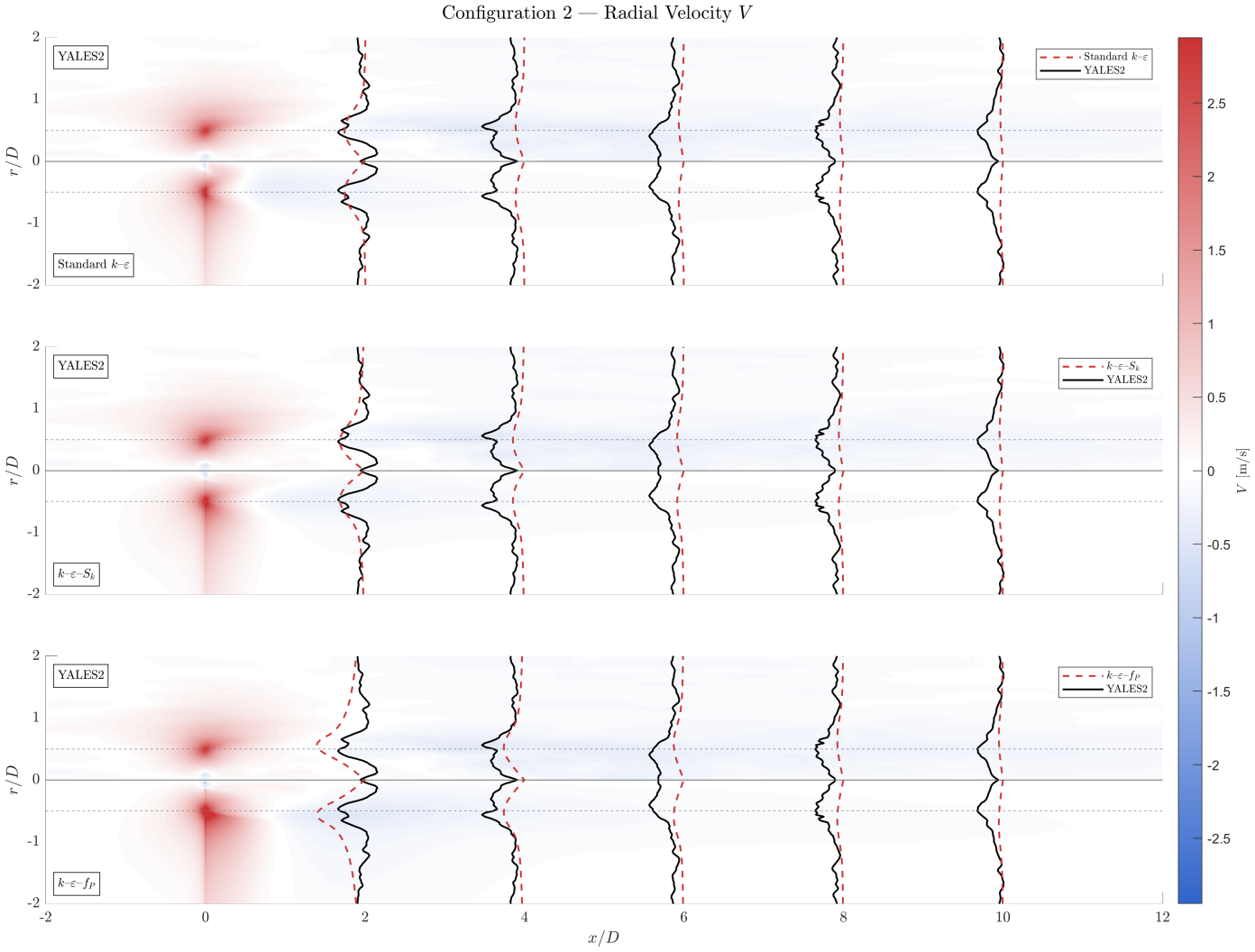

Figure D.10: Radial velocity V for Configuration 2. Upper half: YALES2; lower half: FAWM. Rows correspond to the Standard k–ε, k–ε–S_k, and k–ε–f_P models.

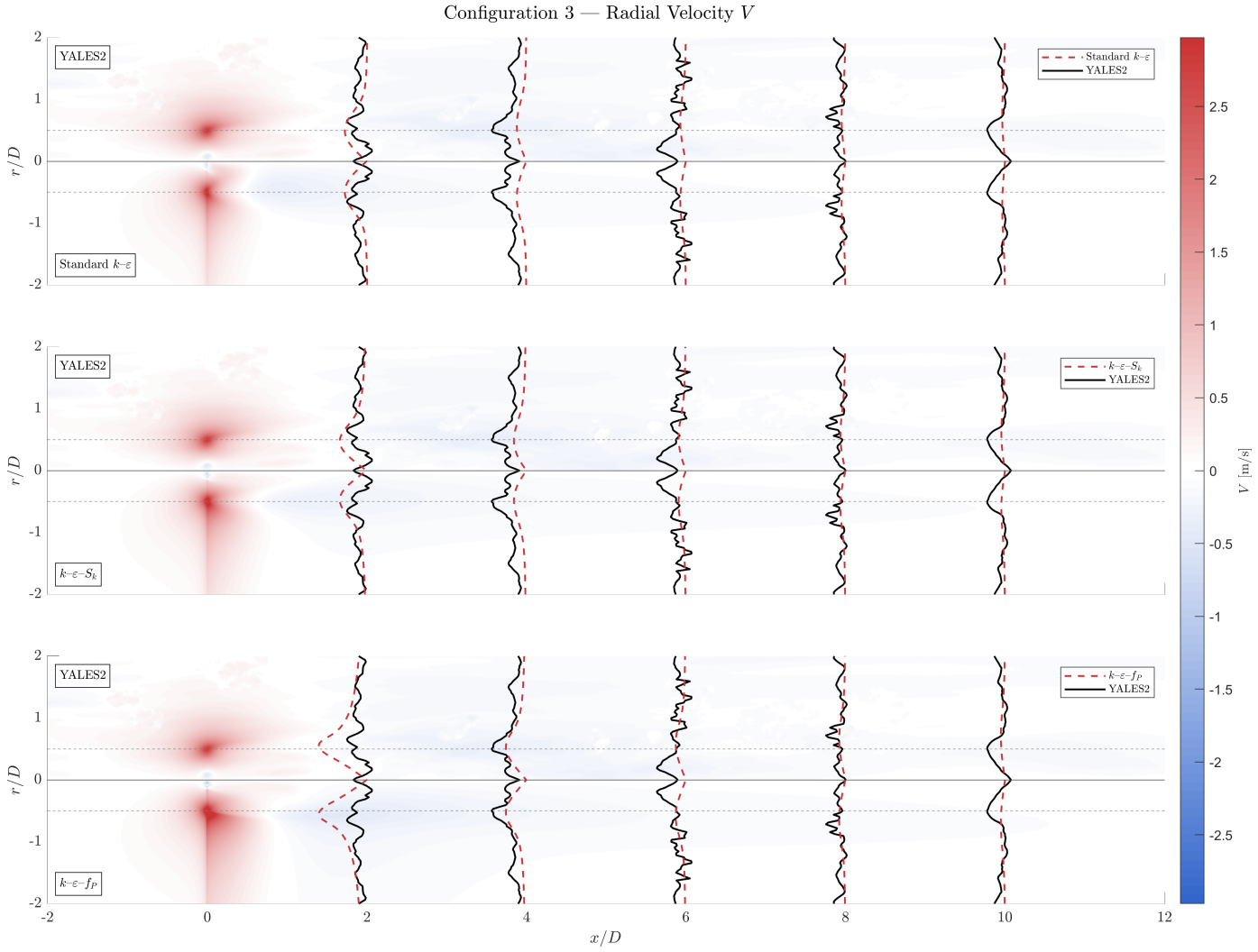

Figure D.11: Radial velocity V for Configuration 3. Upper half: YALES2; lower half: FAWM. Rows correspond to the Standard k–ε, k–ε–S_k, and k–ε–f_P models.

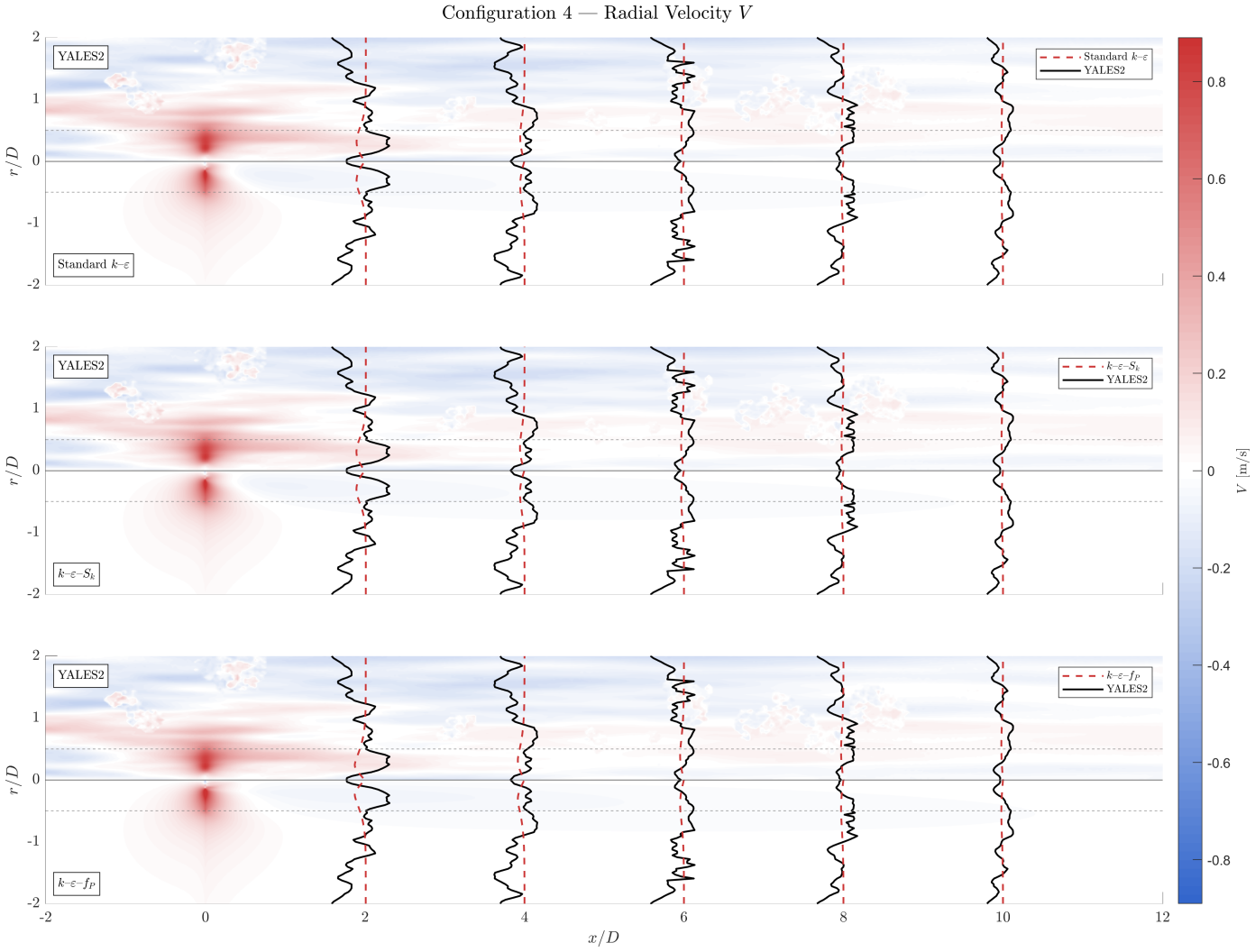

Figure D.12: Radial velocity V for Configuration 4. Upper half: YALES2; lower half: FAWM. Rows correspond to the Standard k–ε, k–ε–S_k, and k–ε–f_P models.

D.4 Eddy Viscosity

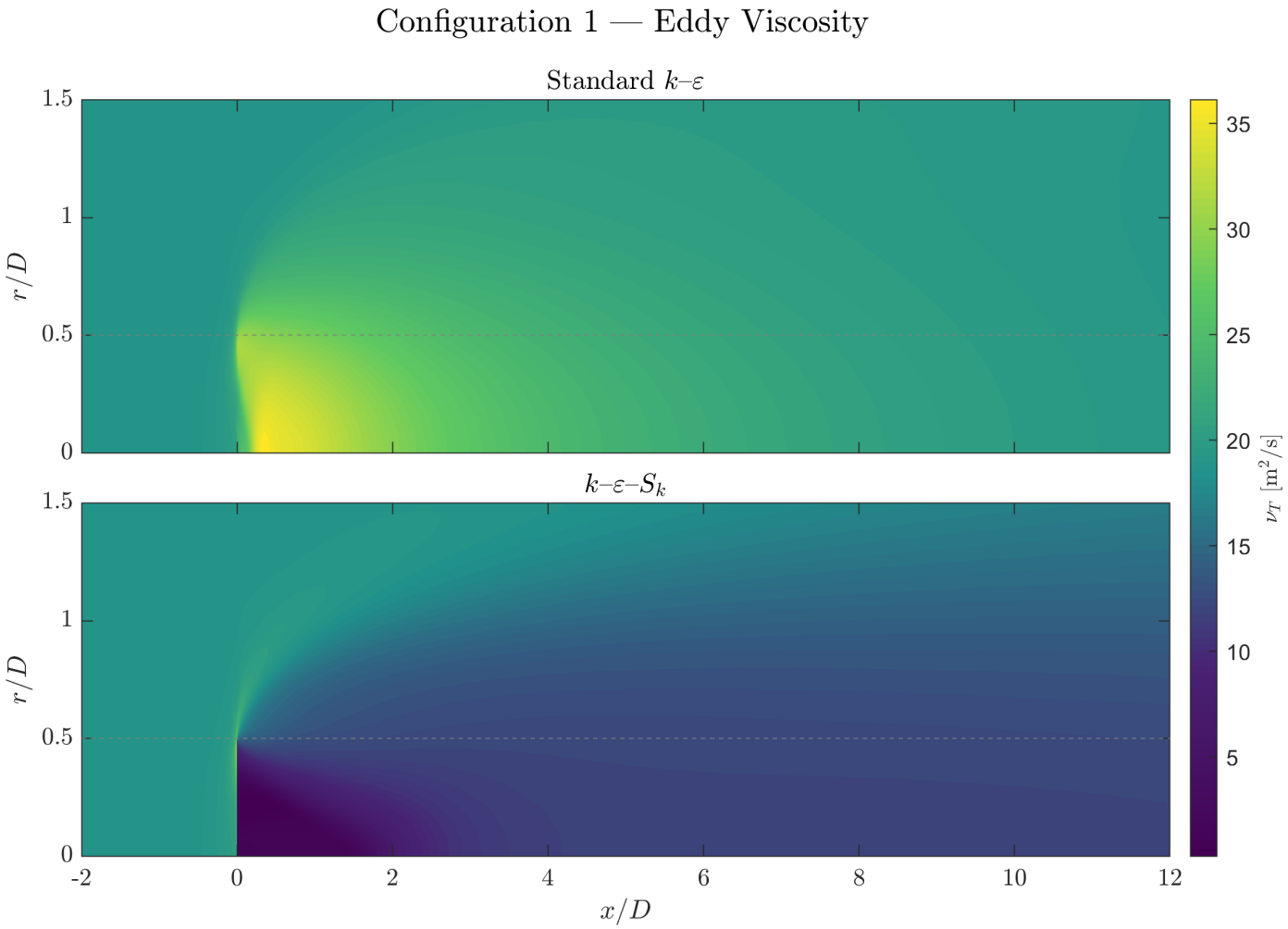

Figure D.13: Eddy viscosity ν_T contours for Configuration 1. Shown are the Standard k–ε and k–ε–S_k model predictions. No LES reference is available for this quantity. The k–ε–f_P model did not converge for this configuration.

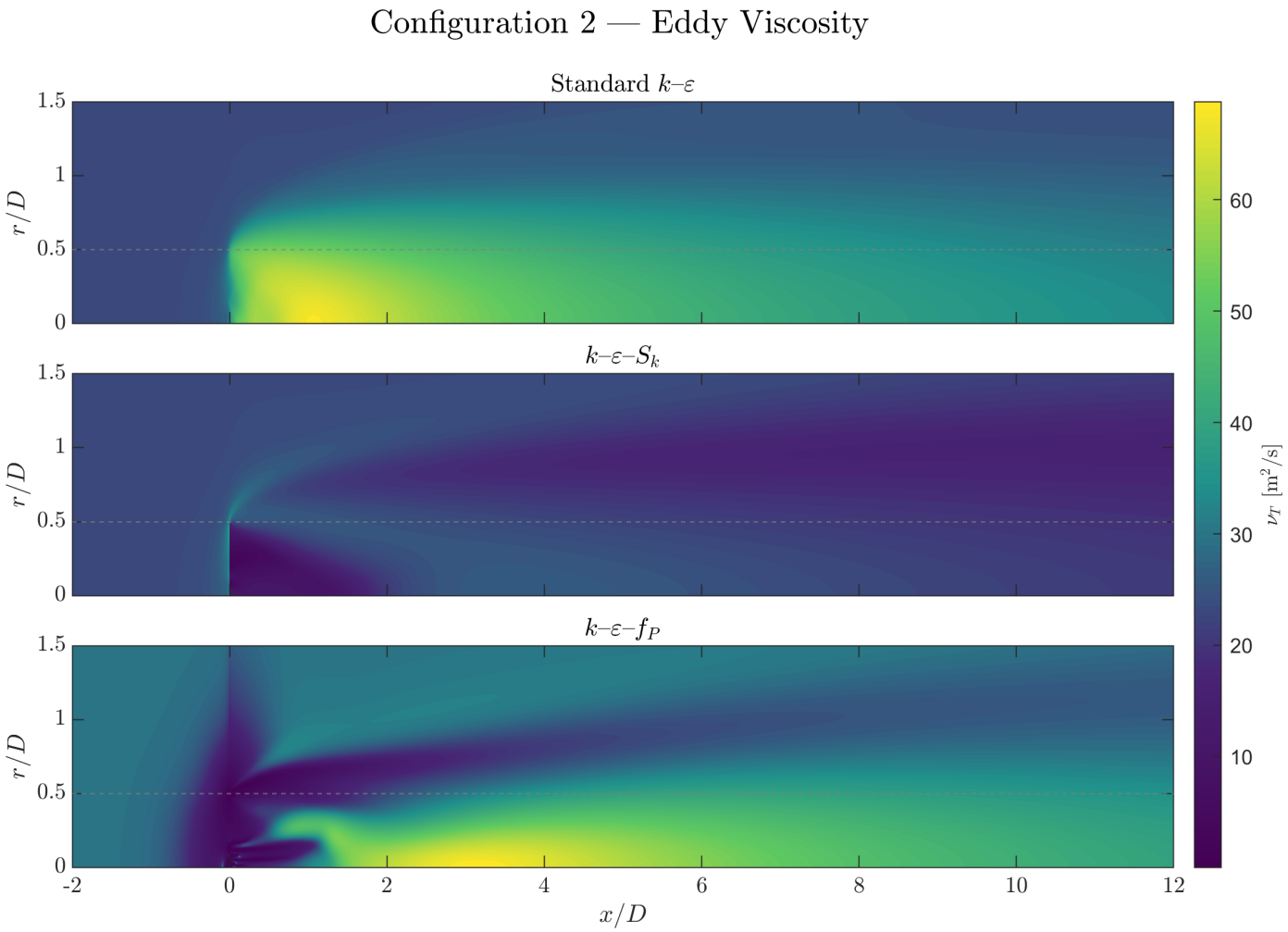

Figure D.14: Eddy viscosity ν_T contours for Configuration 2. Shown are the Standard k–ε, k–ε–S_k, and k–ε–f_P model predictions.

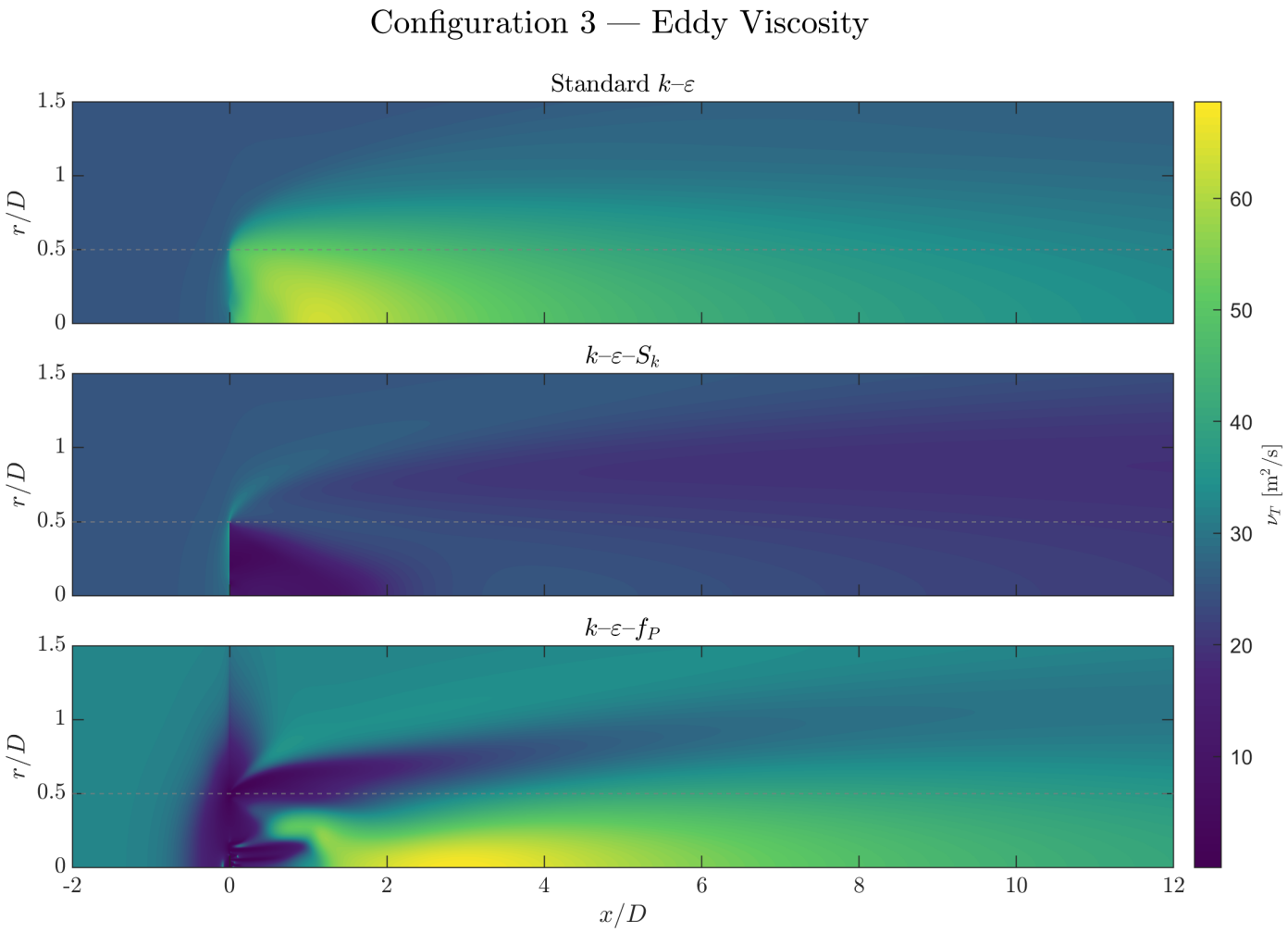

Figure D.15: Eddy viscosity ν_T contours for Configuration 3. Shown are the Standard k–ε, k–ε–S_k, and k–ε–f_P model predictions.

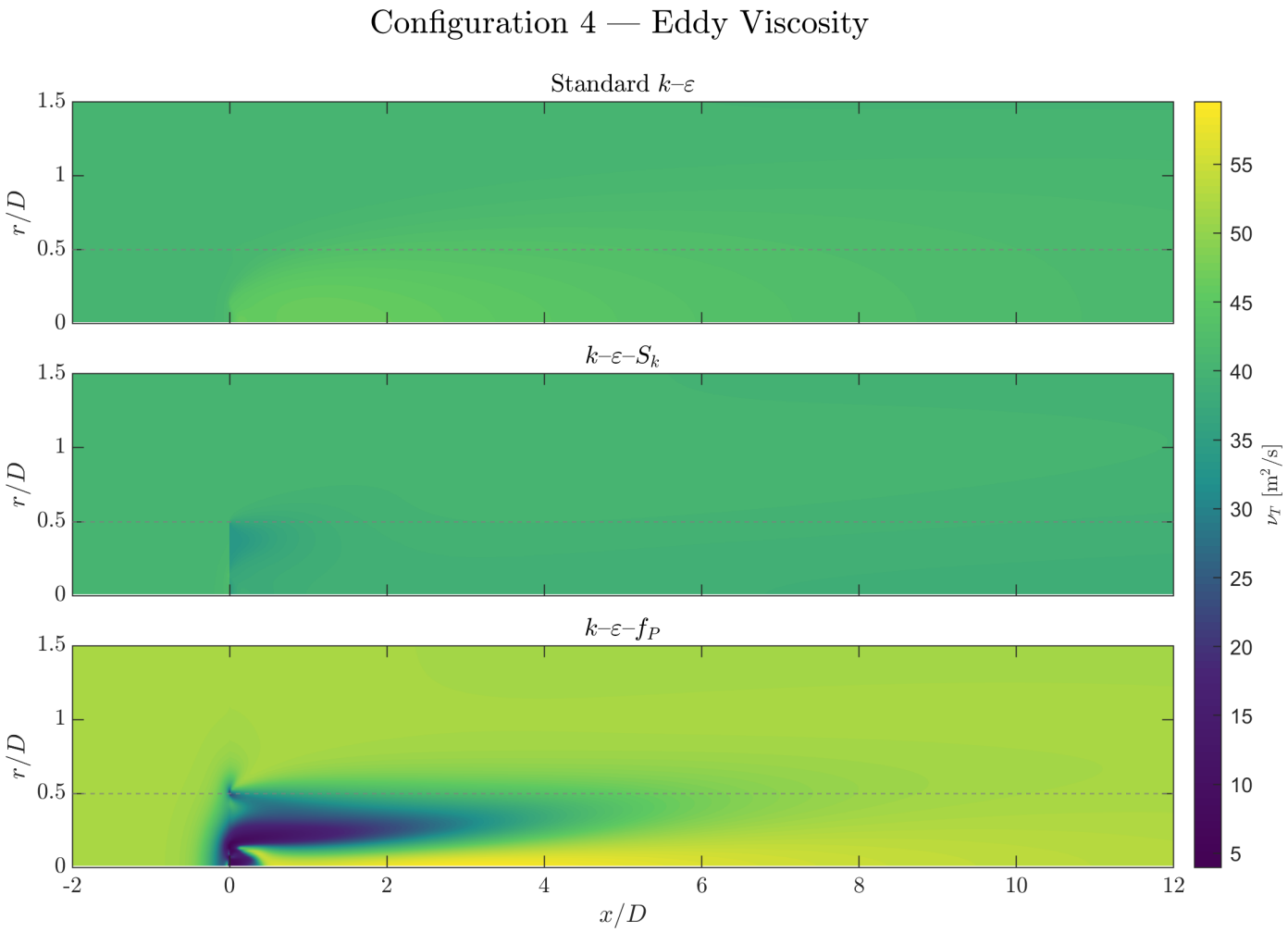

Figure D.16: Eddy viscosity ν_T contours for Configuration 4. Shown are the Standard k–ε, k–ε–S_k, and k–ε–f_P model predictions.

D.5 Dissipation Rate

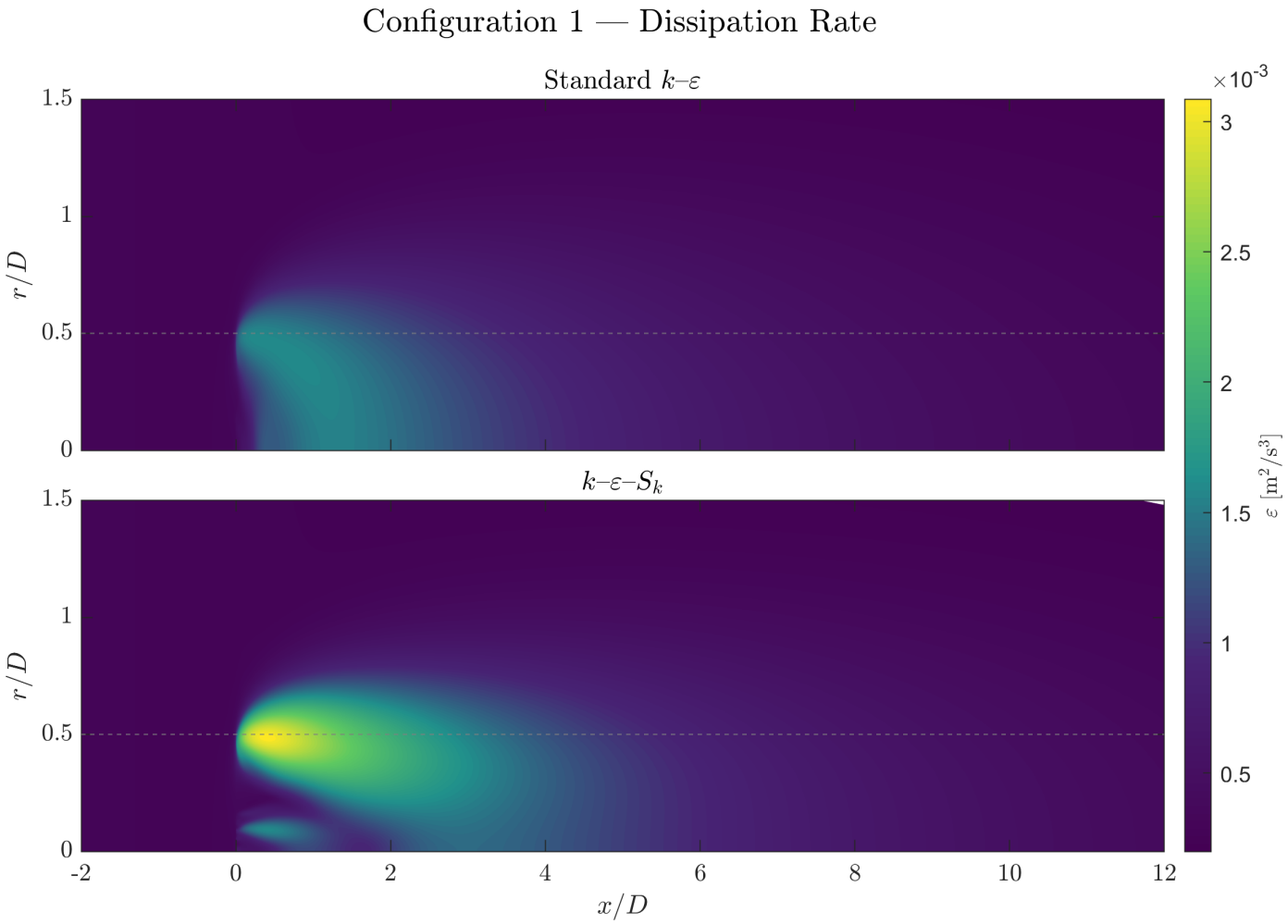

Figure D.17: Dissipation rate ε contours for Configuration 1. Shown are the Standard k–ε and k–ε–S_k model predictions. No LES reference is available for this quantity. The k–ε–f_P model did not converge for this configuration.

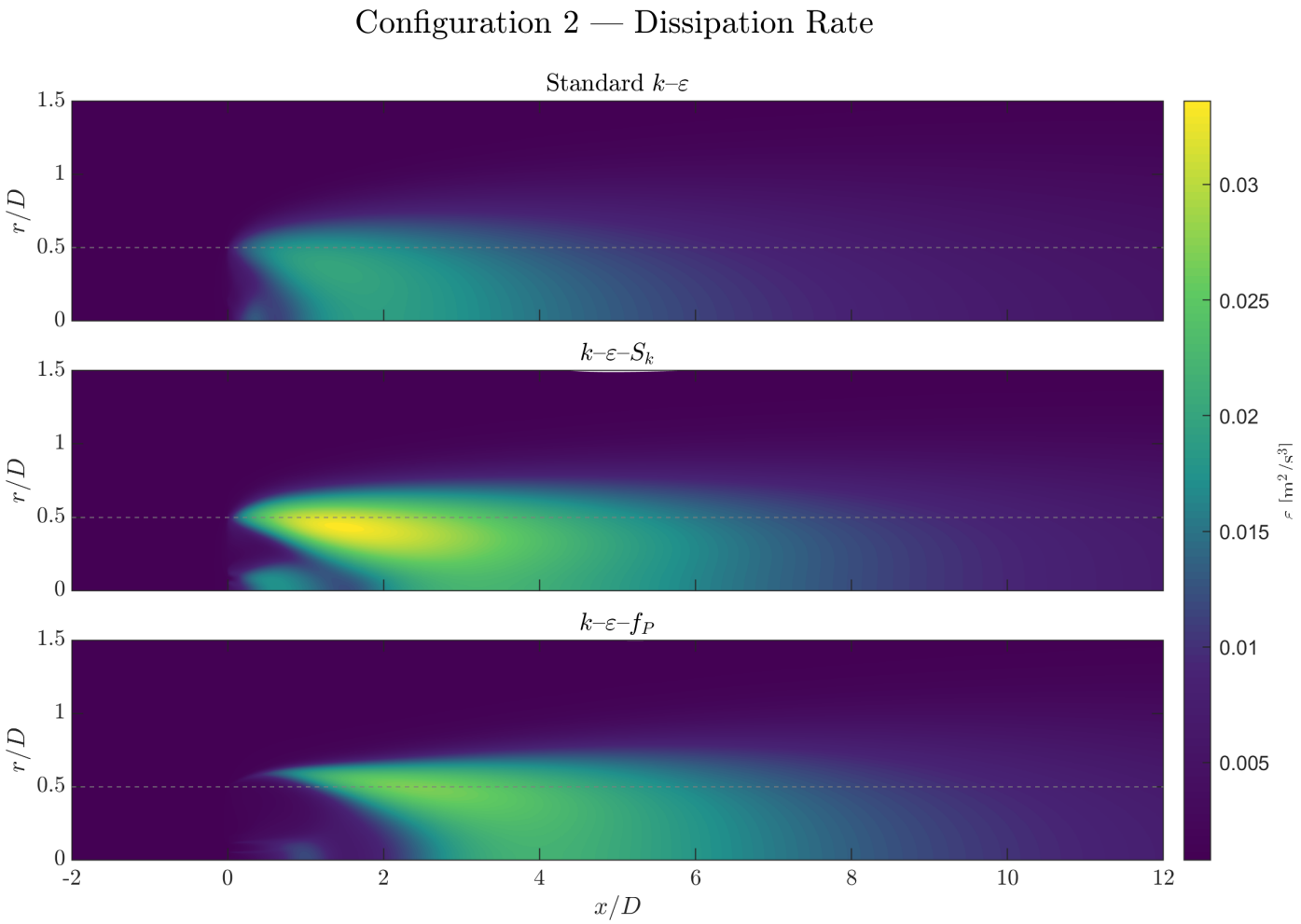

Figure D.18: Dissipation rate ε contours for Configuration 2. Shown are the Standard k–ε, k–ε–S_k, and k–ε–f_P model predictions.

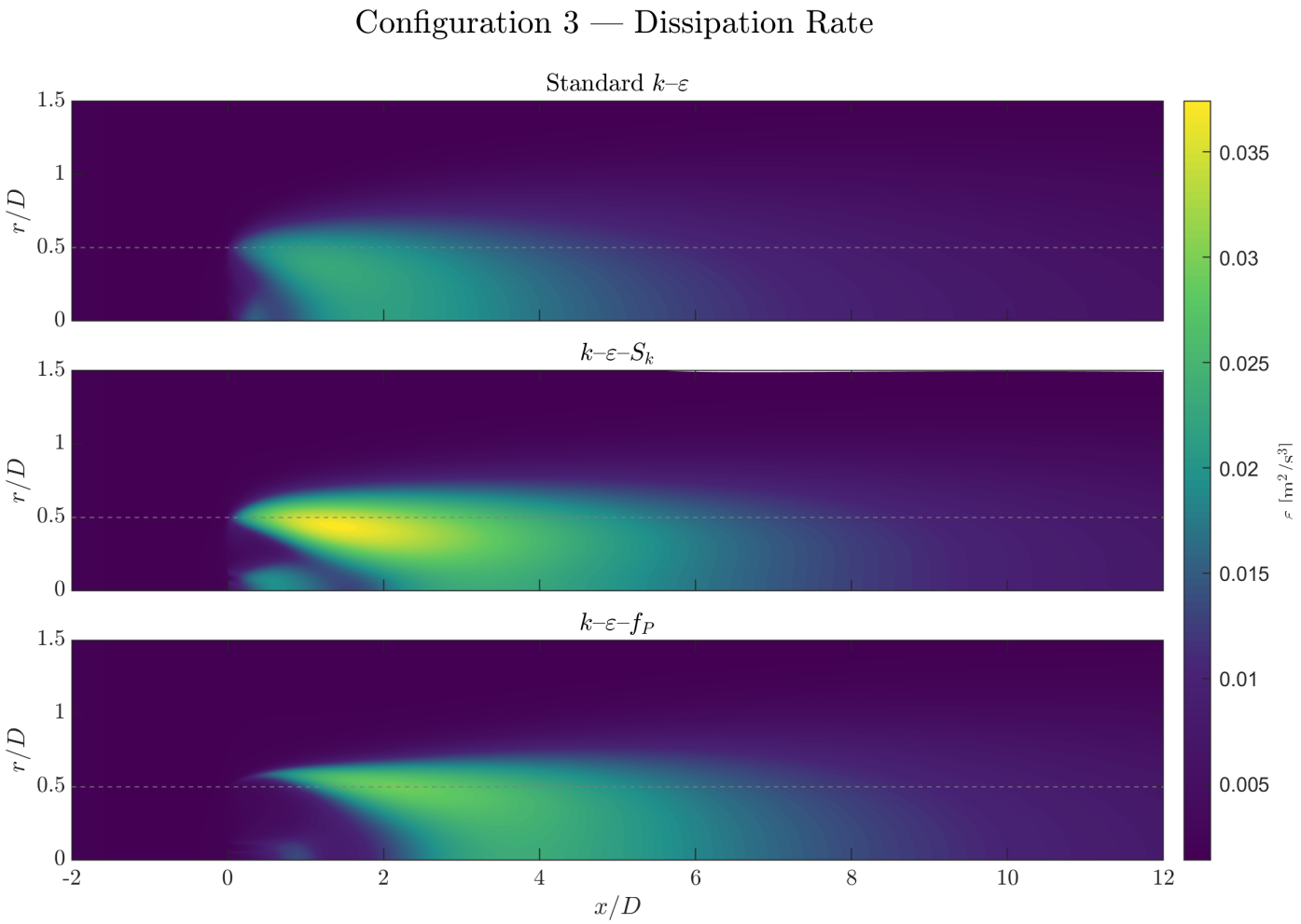

Figure D.19: Dissipation rate ε contours for Configuration 3. Shown are the Standard k–ε, k–ε–S_k, and k–ε–f_P model predictions.

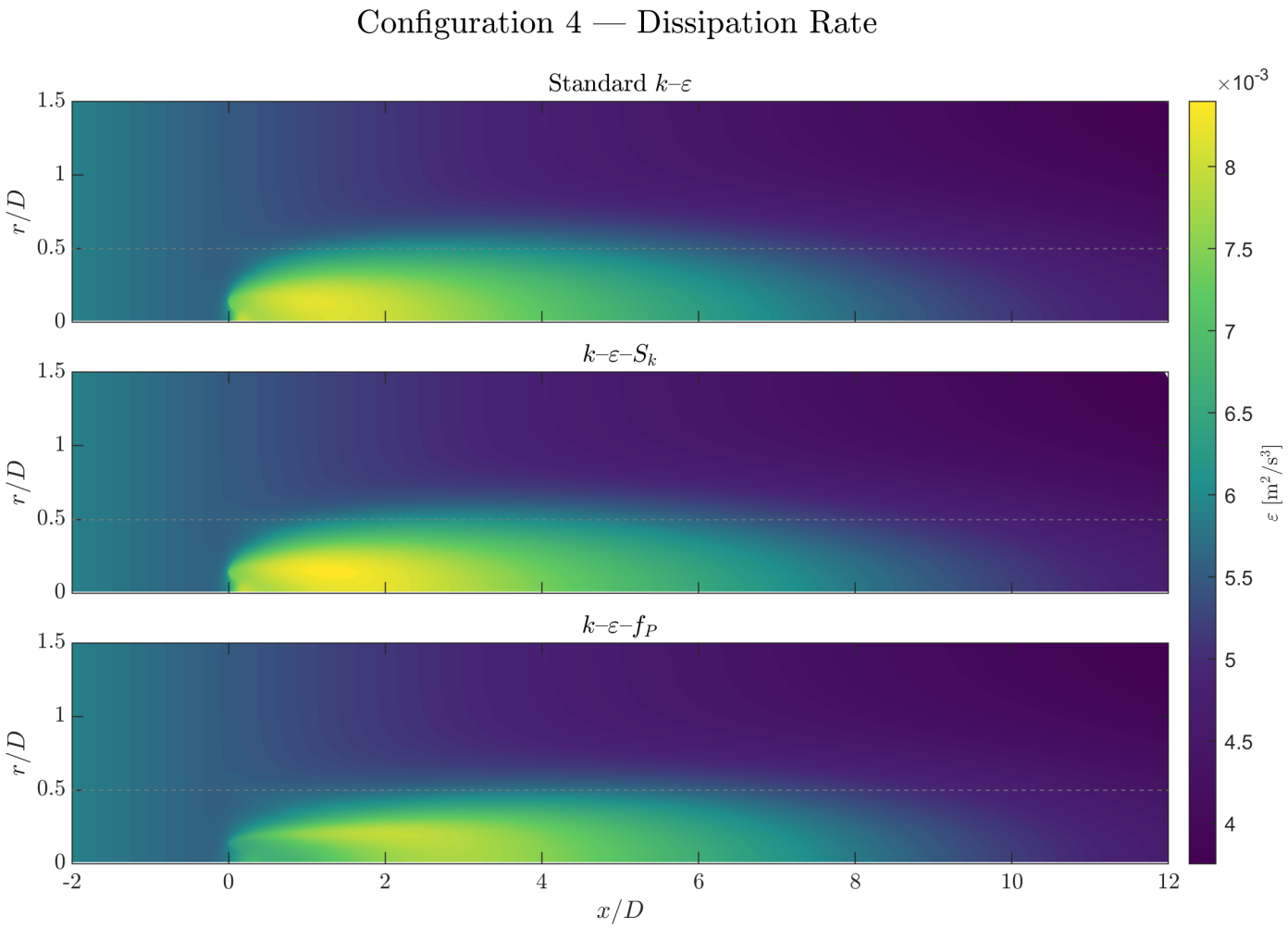

Figure D.20: Dissipation rate ε contours for Configuration 4. Shown are the Standard k–ε, k–ε–S_k, and k–ε–f_P model predictions.